Department of Physics and Astronomy and
London Centre for Nanotechnology
University College London

Polythiophene Nanofibres for Optoelectronic Applications

A thesis submitted for the degree of

Doctor of Philosophy

at University College London

Nico Seidler

London, November 2014

I, Nico Seidler, confirm that the work presented in this thesis is my own. Where information has been derived from other sources, I confirm that this has been indicated in the thesis.

Nico Seidler
London, 9th November 2014

Principal Supervisor: Prof. Franco Cacialli

Subsidiary Supervisors: Dr. Giovanni Mattia Lazzerini and Dr. Neil Curson

Part of this thesis is included in the following publication:

Nico Seidler, Giovanni Mattia Lazzerini, Giovanni Li Destri, Giovanni Marletta, and Franco Cacialli. Enhanced crystallinity and film retention of P3HT thin-films for efficient organic solar cells by use of preformed nanofibers in solution. *Journal of Materials Chemistry C*, 2013, **1**, 7748

Acknowledgements

I would like to acknowledge funding from the European Commission through the Marie Curie Initial Training Network *SUPERIOR*. Not only did this funding allow me to focus on my work for three years, it also gave me the opportunity to engage with a wider scientific community through the attendance of workshops, conferences and network meetings. It put me in touch with a large number of bright, motivated, and inspired researchers, an experience I truly enjoyed.

Many people kindly provided their help and assistance with the work on this thesis, and I would like to thank in particular:

- *Franco Cacialli*, for giving me the opportunity and freedom to work on this project, for his interest and assistance on many occasions.
- *Neil Curson* for his valuable input during the transfer exam.
- *Mattia Lazzerini* for an introduction to TFT-measurements, LabView, wine and blasphemy, and for frequent help with technical troubleshooting.
- *Giovanni Marletta* and *Giovanni Li Destri* for XRD and XPS measurements and for help with the analysis of the data.
- *Peter Christianen* and *Peter van Rhee* for performing the magnetic field measurements and helping with the interpretation of the results.
- *Jialiang Xu* for his help in organising my stay in Nijmegen and his assistance with the magnetic field measurements.
- *Stefano Prato*, *Stefano De Monte*, *Barbara Troian* and *Ivan Iskra* for help with the SNOM measurements, and for their hospitality during my visit to Trieste.

- *Egle Sirtautaite-Sidlauskiene* and *Akimitsu Narita* for supplying their precious material that would have made it into this thesis if it would just have formed fibres.

- *Oliver Fenwick* for his comprehensive introduction to many experimental setups and for teaching me the basic survival skills needed as a foreigner among Italians.

- *Francesco Di Stasio* for providing me with a clear understanding of what it means to be a spectroscopist.

- *Marten Tolk* for being my PV-buddy in the group, for most valuable scientific discussions, and for many evenings philosophising about science, morality, nutrition and robots.

- *Ruurd Heuvel* for his work towards the alignment of the nanofibres and for his persistent fight against the s-shape.

- *Giulia Tregnago, Francesco Bausi, Valentina Robbiano, Giuseppe Paternò, Charlotte Fléchon, Penglei Li, Apollo Mian, Patrick Cullen, David Buckley* and all other current, previous, and temporary residents of the physics basement for always maintaining a supportive, cooperative and friendly work environment.

Very special thanks to *Elisa Criado* for providing essential distraction, for her love and her continuous support.

Abstract

This thesis reports on the fabrication and characterisation of self-assembled nanofibres of poly(3-hexylthiophene) (P3HT), and demonstrates how these nanofibres can be used in applications like thin-film transistors and solar cells.

The first results chapter describes a preparation method of P3HT nanofibres in a solution of chlorobenzene by using di-tert butyl peroxide (DTBP) as an additive. This method allows the fabrication of films of P3HT with high molecular order and gives control over the film retention. The films are characterised using a range of experimental techniques, including optical absorption, X-ray diffraction and atomic force microscopy, which also allows to determine the dimensions of individual, separated nanofibres.

A more detailed investigation into the temperature dependence of the photoluminescence (PL) of nanofibre films in comparison to P3HT thin-films is presented in the second results chapter. The line-shape of the measured PL of the nanofibres shows significant differences to the thin-film, which is most distinctive at a temperature of around 150 K. At this temperature, the measurements show a change of the emission characteristics for the nanofibres which is absent in the thin-film. The cause for the observed transition can be related to the increased planarisation of the polymer backbone inside the nanofibres with increasing temperature. This gives rise to more dominant intrachain coupling for the fibres, in contrast to predominantly interchain coupling in P3HT thin-films.

The third results chapter demonstrates the application of the nanofibre films in thin-film transistors and solar cells. It is shown how the high molecular order of the nanofibres in combination with the formation of fibre networks can be used to control the field-effect mobility of P3HT films. Solar cells are fabricated by successive deposition of a nanofibre film and an electron acceptor layer, resulting in power conversion efficiencies comparable to bulk heterojunction solar cells.

Contents

List of Figures

1. Introduction

1.1. Organic Electronics

The field of organic electronics is a fast-evolving area of research and development that holds great promise to play a significant role in shaping our future. [1] Organic electronics make use of organic semiconductors, which are carbon-based materials that show semiconducting properties similar to their inorganic counterparts. In contrast to classic semiconducting materials like silicon, germanium or gallium arsenide, the basic optical and electrical properties of organic semiconductors do not derive from a crystal structure, but are defined by the energy levels of the individual molecules and their intermolecular interactions. This fundamental difference brings a range of important advantages compared to inorganic systems, which creates the potential for novel and improved applications in the field of electronics. The main advantage is that due to their non-crystalline character, organic materials are flexible and more mechanically robust than inorganic crystalline systems. Furthermore, the optoelectronic properties can be tailored by molecular design, targeting particular needs in terms of electrical and optical properties. Designing materials with a high absorption coefficient allows applications to be thin and light-weight. This also allows increased freedom in the design of the final products in terms of colour and form factor. Not only the photophysical properties, but also the chemical properties can be tailored, making the materials non-toxic and soluble in a range of solvents, which brings significant advantages for large scale production, since it reduces energy demand and complexity of manufacturing equipment. It also allows a variety of production methods, from large scale coating techniques like slot-die coating, spray coating, screen printing or thermal evaporation to small scale and highly customisable techniques like ink-jet printing.

The types of applications possible with organic materials cover the whole range of

electronics, from basic devices such as light-emitting diodes, transistors and photovoltaic cells to integrated circuits, displays and sensor applications. Some of these applications are already a commercial reality or on the verge of entering the consumer market. As one of the first applications, displays based on organic light-emitting diodes (OLEDs) are available in consumer electronics like smart phones and TVs. OLEDs for lighting applications are currently developed and are expected to enter the market in the coming years. [2] The development of organic thin-film transistors is lagging somewhat behind, but significant progress in improving the performance of OTFTs was made in recent years which brings this technology closer to commercialisation. [3] The first products that use organic photovoltaic cells are becoming available and the field is moving fast towards high volume production for the use in building integrated photovoltaics and large scale energy generation. [4, 5]

However, despite the impressive progress that was made in this field in recent years, there are a number of disadvantages and issues that still need to be addressed in order to make organic electronics a success. One inherent problem that results from the low crystallinity and soft nature of the materials is their low charge carrier mobility, which results in substantial resistive losses and limits the current that can be transported by organic materials. A second issue is the chemical instability of many organic materials, especially for electron-conducting compounds which are prone to oxidation, negatively impacting the performance over time. Long-term stability of the compounds becomes particularly critical in applications where high excitation densities are required, like in OLEDs for lighting, or where the device needs to withstand extreme conditions like moisture or intense light illumination as is necessary for the use in solar cells. Furthermore, although the photophysical and electrical properties of organic materials are mainly governed by the arrangement of the molecular orbitals of the individual molecules, intermolecular interactions can significantly alter these properties, which becomes particularly important once the molecules are incorporated in a solid film. Intermolecular interactions are determined by the arrangement of individual molecules with respect to each other, both for those of the same type as for different molecules. In a thin-film, this particular arrangement of molecules is known as *nanomorphology* and its impact on film properties, device performance and device stability is immense.

Due to the importance and complexity of the problem, large research effort has been

put into ways to characterise and control the nanomorphology of organic thin-films. Several classes of organic materials and material systems have been investigated, including small molecules, fullerenes, oligomers and polymers. One system that is particularly interesting is a mixture of poly(3-hexylthiophene) (P3HT) and phenyl-C61-butyric-acid-methyl (PCBM). This material combination showed unprecedented performance as active layer in photovoltaic devices and has marked a major milestone in the development of organic solar cells. [6–8]

Although with continuing research efforts in the field of organic photovoltaics, other material combinations surpassed the P3HT:PCBM system in terms of solar cell performance,[9–13] it still remains one of the most used model systems to study fundamental processes, as well as being the first material to be investigated for large-scale OPV production. [4, 14]

1.2. Motivation and Outline of this Thesis

P3HT has been investigated intensively over the last years for the use in organic thin-film transistors (OTFTs) and solar cells, and has shown remarkable performance in both applications. [15–17] Most of the work was focused around structure-performance relationships of films deposited from different solvents, as well as investigations of a variety of film treatments after deposition. It was found that the main property defining factor is the formation of semi-crystalline domains of P3HT, which requires highly regioregular P3HT and depends strongly on the molecular weight. [18] This semi-crystalline character of P3HT is responsible for relatively high charge carrier mobilities in OTFTs as well as for the formation of a film morphology which is favourable for the efficient exciton dissociation and charge transport in organic solar cells when mixed with PCBM. [19]

However, this thesis focuses on a less investigated property of regioregular P3HT, which is the ability of the polymer chains to self-assemble into highly ordered microscopic structures already in solution. [20] As will be shown in the following chapters, these structures show photophysical properties which are significantly different from P3HT films, which helps to reveal new insight in how the optical response of polymers is affected by the type of nanoscale ordering. The possibility to control the degree of crystalline order in solution also opens up new ways to control the nanomorpholoy of

a polymer thin-film prior to deposition. This is particularly interesting for the use in OTFTs and solar cells, since it allows the control of fundamental device properties during solution preparation. This has the potential to eliminate the dependence on particular deposition methods and post-deposition treatments. For this reason, new methods to make use of P3HT NFs in solution are investigated in this thesis.

The presented work demonstrates how di-tert-butyl peroxide (DTBP), which previously has been suggested as a crosslinker for P3HT, [21] can be used to control the growth of P3HT nanofibres in solution. By this method, important properties of the spin-cast film like film retention and overall crystallinity can be influenced. It is shown how pre-grown fibres in solution can be applied in a novel approach to fabricate organic solar cells, in which a better control over the the formation of the bulk heterojunction is provided by a successive deposition of donor and acceptor material. Interestingly, even though the nanomorphology of the active layer of the nanofibre solar cells shows a much higher degree of crystallinity and hence is expected to inhibit close intermixing of the donor and the acceptor phase, [22] the resulting power conversion efficiency is comparable to conventionally processed bulk-heterojunction solar cells.

Furthermore, this work investigates the temperature dependence of the photoluminescence of nanofibre films fabricated using DTBP, as well as using fibres grown by slow cooling methods reported in literature. [23–25] For the first time it can be shown that a photoluminescence behaviour which indicates the presence of J-type dipole coupling shows up not just if measured on individual fibres, but also on larger assemblies of nanofibres. This behaviour can be traced back to the different molecular arrangement in the nanofibres, mainly characterised by a higher planarity of the polymer backbone, if compared to P3HT films.

Following this section, **Chapter 2** gives a brief introduction to the fundamental processes in organic semiconductors. It is focused on topics that are relevant for this work, and references to literature for further reading are given.

The description and discussion of experimental results is structured into three individual chapters. The first result chapter (**Chapter 3**) describes the fabrication of P3HT NFs, mainly focused on the technique in which DTBP is used as an additive to a solution of P3HT in chlorobenzene. A range of experimental techniques is employed to characterise individual fibres as well as NFs deposited as films that can be used

for the application in optoelectronic devices.

The second results chapter (**Chapter 4**) looks in more detail at the photoluminescence (PL) of P3HT NFs, at varying temperatures ranging from 7 K to room temperature. The temperature dependence of the PL is a sensitive probe for structural properties inside polymer aggregates. As will be shown, the observed behaviour of the NFs deviates significantly from that of P3HT thin-films, which indicates differences in the polymer packing arrangement.

The last results chapter (**Chapter 5**) demonstrates how P3HT NFs can be used in OTFTs and solar cells. The charge transport in P3HT films and NF films is studied and it is shown how the method of forming NFs in chlorobenzene solution can be used to control the field-effect mobility of P3HT films. Furthermore, this chapter reports on a method to fabricate organic solar cells by successive deposition of donor and acceptor layer, making use of the high film retention of the NF films. Conclusions about the morphology of the active layer can be drawn from the current - voltage characteristics and external quantum efficiencies. **Chapter 6** concludes this thesis with a summary of the presented work and suggestions for further experiments.

2. Fundamentals of Organic Semiconductors

This chapter introduces some of the basic properties of organic semiconductors that are of relevance to this work. Organic semiconductors are, as part of organic materials in general, based on carbon atoms. The fundamental properties therefore derive from the specific bonds that are formed between carbon atoms itself, as well as between carbon and other elements, most importantly hydrogen, sulphur and nitrogen. Some of these compounds have the ability to conduct electrical charges on specific electronic states that are allowed, while some energy states are forbidden, similar to a band gap between conduction band and valence band in classic semiconducting materials. This is why these compounds are called organic semiconductors.

The following sections describe the fundamentals of light-matter interactions of organic semiconductors as well as charge transport. A particular focus lies hereby on the photophysics of aggregates of semiconducting polymers. The last section deals with the photogeneration of electric charges in organic semiconductors and how the understanding of the underlying principles can be used to design efficient photovoltaic devices.

The content of this chapter is based on general findings in the field of organic electronics and has been gathered from a range of sources, mainly from university lectures [26, 27] and text books. [28–32] Individual citations for most of the contents have therefore been omitted. However, if specific scientific findings that were published recently are presented or if illustrations have been adapted from text books then the relevant reference has been added.

2.1. Optical Properties of Organic Molecules

2.1.1. Conjugated π-systems

The electronic configuration of carbon in the ground state is $1s^2 2s^2 2p^2$, hence there are four valence electrons. However, this configuration cannot explain the bonds as they are present for example in ethylene ($H_2C{=}CH_2$). In this case, a mixing of the 2s orbital with two of the three p-orbitals (p_x, p_y, p_z) takes place, and three new, hybrid sp^2-orbitals are formed (Figure 2.1 (a)). These three orbitals all lie

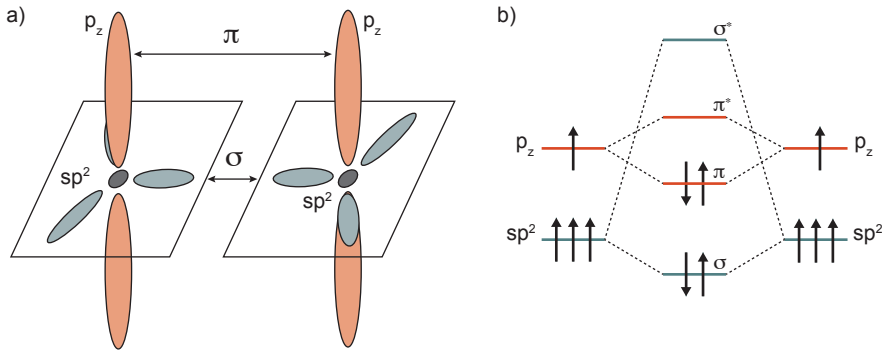

Figure 2.1.: (a) Sketch showing the orbitals of sp^2-hybridised carbon and the formation of carbon-carbon douple bonds. (b) The overlap of the sp^2- and p_z orbitals results in a splitting of the energy levels in bonding (σ-, π-) and antibonding (σ^*-, π^*-) states.

in one plane, forming angles of 120° among one another. The remaining orbital of the three perpendicular p-orbitals remains unchanged, standing perpendicular on the sp^2-orbitals. Bonds formed by sp^2-orbitals are called σ-bonds, and they are characterised by a strong overlap and a resulting large splitting into a bonding and an antibonding state. The orbitals of neighbouring p-orbitals form so-called π-bonds. The overlap of these orbitals is significantly lower, which results in a smaller splitting. As sketched in Figure 2.1 (b), the bonding π-orbital therefore forms the highest occupied molecular orbital (HOMO), and the lowest unoccupied molecular orbital (LUMO) is formed by the antibonding π-orbital. Hence, transitions from the ground state to the first excited state of molecules with a conjugated system predominantly involves π-electrons. In the case of larger molecules with many π-bonds in a row, like

poly-ethylene or molecules with thiophene rings, the individual π-orbitals will overlap and form a system of partially delocalised electrons above the plane of carbon atoms, the so-called π-system.

2.1.2. Molecular Transitions and Optical Spectra

A molecular state can be quantum mechanically described using the wave function

$$\psi_{n,m} = \phi_n \cdot \chi_{n,m} \ , \tag{2.1}$$

where ϕ_n is the wave function of the electrons in the n-th electronic state, and $\chi_{n,m}$ is the nuclear wave function of the m-th vibrational level of the n-th electronic state. The electronic part itself can be written as a product of one part ϕ_n^e which is just dependent on the spacial coordinates of the electrons, and one spin-dependent part ϕ_n^s,

$$\phi_n = \phi_n^e \cdot \phi_n^s \ . \tag{2.2}$$

This description of a molecular state can be used to evaluate the probability R_{lu}^2 for a transition from one state ψ_l to another state ψ_u,

$$R_{lu}^2 \propto |\langle \psi_u \, | \mathcal{M} | \, \psi_l \rangle|^2 \ , \tag{2.3}$$

where $\mathcal{M}$ is the operator of the dipole moment. A sketch of some of the possible transitions in a molecule is shown in Figure 2.2. Using (2.1) in (2.3) results in

$$R_{lu}^2 \propto |\langle \phi_u^e \, | \mathcal{M} | \, \phi_l^e \rangle|^2 \, |\langle \chi_{u,q} | \chi_{l,p} \rangle|^2 \, |\langle \phi_u^s | \phi_l^s \rangle|^2 \ . \tag{2.4}$$

The first term is called the transition dipole moment from the initial state l to the final state u,

$$M_{l \to u} = \langle \phi_u^e \, | \mathcal{M} | \, \phi_l^e \rangle \ . \tag{2.5}$$

Cases where the value of this expression is zero (and hence $R_{lu}^2 = 0$) are called *dipole-forbidden*. Considering also the second term of (2.4), which describes the vibration of the nuclei, the amplitude for the vibronic transition can be written as

$$M_{l,p \to u,q} = M_{l \to u} \, \langle \chi_{u,q} | \chi_{l,p} \rangle \ . \tag{2.6}$$

The square of the absolute value of $\langle \chi_{u,q} | \chi_{l,p} \rangle$ is called *Franck-Condon factor* and describes the probability with which a certain vibrational state is excited during an electronic transition.

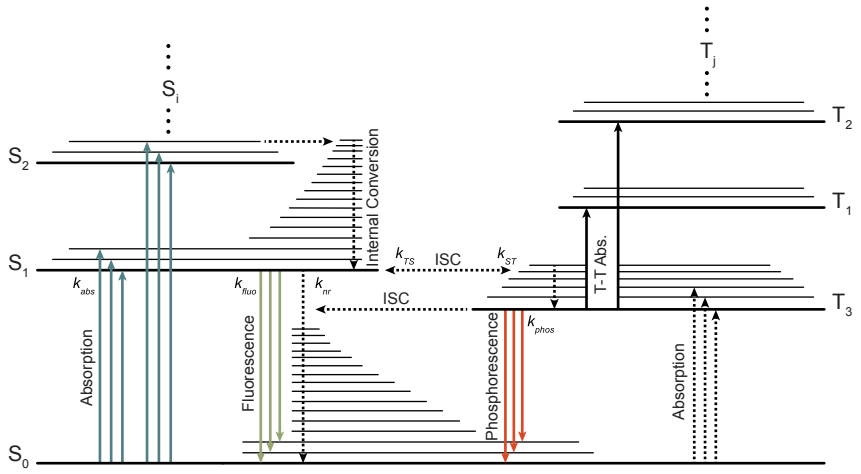

Figure 2.2.: Schematic of possible transitions in a molecule (*Jablonski* diagram). The symbols k stand for transition rates for absorption (k_{abs}), fluorescence (k_{fluo}), phosphorescence (k_{phos}) and transitions from the singlet to the triplet system (k_{ST}) and vice versa (k_{TS}).

The probability for a particular vibronic transition is often stated in form of the oscillator strength f,

$$f_{l,p\to u,q} = \frac{8\pi^2 m_e}{3he^2}\nu \left|M_{l,p\to u,q}\right|^2 \ , \tag{2.7}$$

where ν is the frequency of the transition.

The different oscillator strength of certain transitions are represented in the shape of absorption and emission spectra. Figure 2.3 shows the correlation between the molecular transitions and the optical spectra. Due to a fast internal conversion, the molecule quickly relaxes to the lowest excited state from where the emission can take place. This principle is known as *Kasha rule*, and together with the Franck-Condon principle explains the symmetrical shape of absorption and emission spectra.

The third term in (2.4) describes the spin selection rules. This term just contributes for transitions between states of same spin multiplicity, transitions between singlet and triplet states are not allowed. However, such transitions, know as *intersystem crossing* (ISC) can be observed experimentally. They become allowed because of the coupling of the electron spin with the orbital angular momentum. This *spin-orbit coupling* is most common in molecules that feature a heavy atom (e.g. iridium, platinum, iodine).

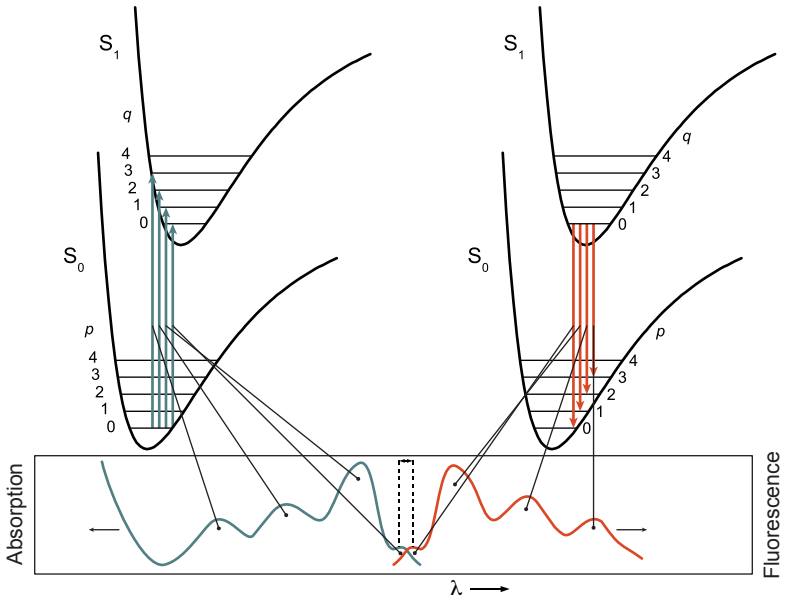

Figure 2.3.: Diagram which illustrates the origin of the symmetrical shape of absorption and emission spectra in organic molecules. The difference in energy between the transitions between the lowest vibrational states of absorption and emission (0-0 transitions) is called *Stokes shift*.

The radiative transition from the lowest excited singlet state to the ground state, $S_1 \rightarrow S_0$, is called *fluorescence*, and transitions from the lowest triplet state are known as *phosphorescence*.

Since phosphorescence in contrast to fluorescence is a dipole-forbidden transition, the typical time-constants τ are significantly bigger ($\tau_{phos}/\tau_{fluo} \approx 10^3 - 10^9$). Therefore, non-radiative processes are often dominating the deactivation of the triplet state, which is why phosphorescence is usually not detectable at room temperature. Figure 2.2 shows the rates k of several process that can take place. A rate is in general defined by its time constant by

$$k = \frac{1}{\tau} \,. \tag{2.8}$$

The probability of a certain process to take place can be expressed as

$$\eta_j = \frac{k_j}{\sum_i k_i} \,, \tag{2.9}$$

where the sum includes the rates of all processes possible from the initial state.

Since two electrons with the same spin-orientation are not allowed to occupy the

same orbital (Pauli principle), the repulsion of two such electrons is weaker than in the case of different spin. This electron-electron repulsion causes S_1 to always be energetically higher than T_1. Hence, the phosphorescence always takes place at higher wavelength than the fluorescence. This difference in energy is called *exchange energy*, or *singlet-triplet splitting*.

2.2. Energy Transfer and Charge Transport

The conjugated π-systems discussed above can extend over many repeat units in a molecule. Most common are aromatic compounds built from benzene rings or thiophene rings, where the π-electrons are delocalised over many alternating single and double carbon bonds. The extension of the π-system over many repeat units requires, however, the aromatic rings to be approximately coplanar. Larger molecules, such as oligomers and polymers will show twists in their backbone which limits the conjugation length. In general, a macromolecule can therefore be seen to consist of repeating units that define the optical properties, called chromophores. An excitation on one chromophore can be transfered *radiatively* or *non-radiatively* to another chromophore. Although originally defined for individual chromophores, in a solid organic semiconductor HOMO and LUMO can be seen as continuous bands in analogy to valence band and conduction band in inorganic semiconductors. The width of these bands is defined by the variations in energetic position of the molecular orbitals of the individual chromophores. The excitation of one chromophore will lead to an electron in the otherwise unoccupied LUMO and a missing electron, a *hole*, in the HOMO. In contrast to inorganic semiconductors, due to the weak overlap of electron density of the chromophores, charges are strongly localised. Electron and hole are strongly bound by Coulomb attraction with a typical binding energy of 0.3 eV to 1 eV. Such electron-hole pairs can be described as neutral quasi-particles called *Frenkel excitons*, in contrast to *Wannier-Mott excitons* which are characterised by much lower binding energies (typically a few meV) and that can be delocalised over tens of the lattice constant in inorganic materials. The presence of an exciton on a chromophore will lead to a disruption of the alternating single and double bond pattern of the conjugated system and give rise to new electron states within the HOMO-LUMO gap. Figure 2.4 shows a schematic of an exciton on an oligothiophene and the rep-

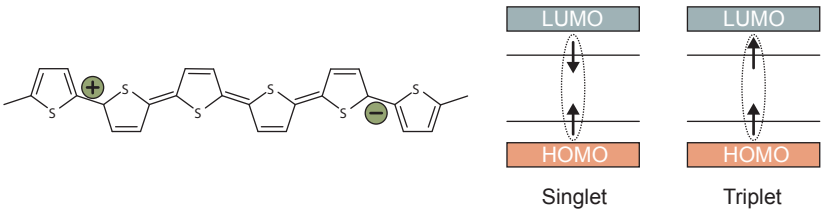

Figure 2.4.: Schematic representation of an exciton on a polythiophene chromophore. The spin-multiplicity of the exciton corresponds to the spin-orientation of electron and hole. (adapted from [29])

resentation in the energy diagram. Since excitations are characterised by their spin multiplicity, excitons can be divided into singlet and triplet excitons, corresponding to the spin-orientation of electron and hole.

As mentioned above, the energy transfer from one chromophore D to a second chromophore A can be divided into two general cases, radiative and non-radiative transfer.

A radiative transfer is simply the emission of a photon by chromophore D, with the subsequent absorption by A, hence

$$D^* \longrightarrow D + h\nu \tag{2.10}$$

$$h\nu + A \longrightarrow A^* \tag{2.11}$$

This *re-absorption* process always involves a loss of energy.

Non-radiative energy transfer is enabled by Coulomb interactions of the charge distribution of the different chromophores. The dominating process due to dipole-dipole coupling is known as *Förster resonant energy transfer* (FRET). The transfer rate k_F,

$$k_F \propto \frac{1}{R_{DA}^6} \int \frac{f_D(\nu) f_A(\nu)}{\nu^4} d\nu \ , \tag{2.12}$$

depends on the oscillator strengths and spectral overlap of the emission and absorption transitions of donor (f_D) and acceptor (f_A), respectively. [33] Despite the R^{-6}-dependence, this transfer is considered a long-range transfer with distances of up to 5-10 nm. With dipole-dipole interactions, the spin-multiplicity is conserved,

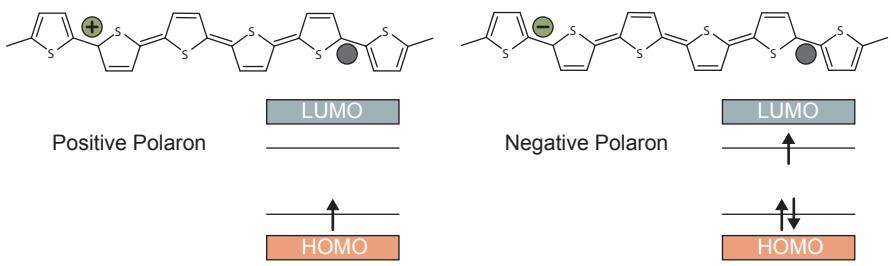

Figure 2.5.: Schematic representation and corresponding energy diagrams of a positive and a negative polaron. (adapted from [29])

which is why transfers of the form

$$ {}^1D^* + {}^1A \longrightarrow {}^1D + {}^1A^* \text{ and} \tag{2.13} $$

$$ {}^1D^* + {}^3A \longrightarrow {}^1D + {}^3A^* \tag{2.14} $$

are allowed, while triplet-triplet transfers like

$$ {}^3D^* + {}^1A \longrightarrow {}^1D + {}^3A^* \tag{2.15} $$

are forbidden.

Another possibility for a non-radiative energy transfer involves the exchange interaction. This requires an overlap of the wave functions of the chromophores, and hence is of much shorter range than the dipole-dipole interaction responsible for the Förster transfer. This transfer is called *Dexter transfer*, and its rate can be written as

$$ k_D \propto e^{-2R_{DA}/L} J \, , \tag{2.16} $$

where L is the mean Van der Waals radius of D and A and J the spectral overlap. [34] Here, in addition to the transitions (2.13) and (2.14), also a triplet-triplet transfer like (2.15) is allowed.

The charge-carrying counterparts to the neutral excitons are called *polarons*. Similar to excitons, these charged quasi-particles induce a lattice deformation which gives rise to localised states within the forbidden gap. In other words, a charge is self-trapped by the deformation it induces in the polymer chain. Figure 2.5 schematically shows a positive and a negative polaron in polythiophene and the corresponding energy diagrams. Charge transport can generally be described by a charge carrier

mobility μ, defined by

$$v_d = \mu \cdot E \ , \tag{2.17}$$

where v_d is the drift velocity of the charges and E the electrical field. Transport between localised states in organic semiconductors occurs through *hopping* of charges, which is, in contrast to inorganic semiconductors, where charge transport is limited by scattering, phonon-assisted. Accordingly, the charge mobility decreases with temperature in conventional semiconductors, while the reverse is true in most organic materials. Several models have been developed to rationalise the hopping transport. In most cases, the temperature dependence of the mobility follows a law of the form

$$\mu = \mu_0 e^{-(T_0/T)^{1/\alpha}} \ , \tag{2.18}$$

where α is an integer ranging from 1 to 4. [35]

The weak intermolecular electronic coupling, the large electron-vibration coupling (leading to distinct geometric relaxations), and disorder effects in organic semiconductors are responsible for relatively low mobilities and a strong dependence on the morphology. This results in variations over several orders of magnitude, typically ranging from 10^{-6}-10^{-2} $\mathrm{cm^2V^{-1}s^{-1}}$ for disordered films, and up to > 1 $\mathrm{cm^2V^{-1}s^{-1}}$ for highly ordered materials. [35, 36]

2.3. Optical Properties of Polymer Aggregates

For the description of the optical response of polymer films and saturated solutions, it is in general not sufficient to look at the behaviour of single chromophores of the material, but instead it is necessary to take interactions of individual chromophores into account. These interactions result from packing arrangements of the polymer chains that can take place in solution as well as in a film, and that are strongly influenced by interactions with the solvent and the film substrate. The optical properties are then determined by the coupling of the optical transition dipoles, which takes place if the packing reduces the distances between the chromophores sufficiently so that the electrons can interact via coulomb forces. To understand the altered optical properties due to transition dipole coupling in polymers, it is worth looking at the possible dipole interactions of two small molecules from a purely electronic perspective (i.e. without phonon interactions). This description has been worked out

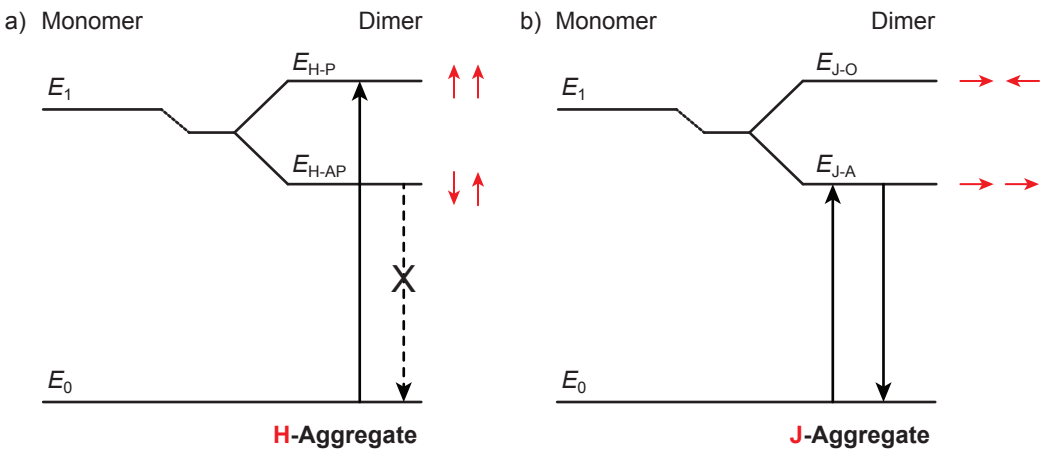

Figure 2.6.: Illustration of the splitting of energy levels in a dimer due to coupling of the transition dipoles. (adapted from [32]) Shown are the ground state, E_0, and lowest excited state, E_1, of the monomer. Depending on the orientation of the interacting dipoles, E_1 is divided in two new energy levels. (a) For a side-by-side coupling (H-aggregate), the parallel orientation will be at higher energy, E_{H-P}, while the energy of the anti-parallel orientation E_{H-AP} will be lower than the monomer level E_1. (b) In J-aggregates, the dipoles couple in one dimension, giving rise to two energy levels, either are dipoles aligned, E_{J-A}, or oriented opposite, E_{J-O}.

early on in the 1960's by Kasha [37], in which he divided small aggregates depending on the orientation of the optical dipoles in two categories, H- and J-aggregates. In H-aggregates, the dipoles align parallel, while in J-aggregates the dipoles align in a head-to-tail orientation. These two cases are illustrated in Figure 2.6.

The two different possible alignments for both cases leads to a splitting of the energy level of the monomer. In the case of H-aggregates, the parallel alignment of the dipoles (which is energetically unfavourable) results in an energy level which lies at higher energy than the one for the monomer. The anti-parallel alignment of the dipoles results in an energy level at lower energy than for the monomer, but the overall transition dipole moment will tend to vanish for this configuration, which means that this energy level is accessed with significantly lower probability through an optical transition from the ground state. The absorption of a dimer in H-aggregate

configuration will therefore be blue-shifted compared to the monomer absorption. Furthermore, the emission will have to take place from the lowest energy excited state (Kasha's rule) following a fast relaxation process with the generation of a phonon. Due to conservation of momentum, the emission from this state to the ground state (lowest vibrational state) will therefore be suppressed.

For J-aggregates, the configuration of two dipoles in a head-to-tail configuration results in an excited energy state with lower energy than the lowest excited state of the monomer, the absorption into this state is therefore red-shifted. Emission from this state is enhanced by the number of coupled chromophores, which leads to superradiant decay rates.

The above model is for purely electronic excitations and does not account for coupling of the electronic states to vibrational modes. To describe more accurately an excitation in a molecular assembly, a model called the Frenkel-Holstein model has been developed, in which the coupling of charges to vibrational degrees of freedom is considered. [38, 39] This coupling describes charged polarons; a charged particle and the deformation of the nuclear coordinates around it.

A significant amount of work to apply the model of Frenkel-Holstein polarons to real systems of polymer aggregates has been carried out by *Frank Spano* and coworkers. A detailed description of this model goes beyond the scope of this thesis, so the following paragraphs will just summarise the outcome of the studies of Spano *et al.* that is of importance for this work. [40–45] Spano developed a model considering that an excitation comprises a vibronically excited central molecule and vibrationally, but not electronically, excited neighbouring molecules. The latter are geometrically distorted, due to elongation of one or more symmetric vibrational coordinates.

To account quantitatively for exciton-vibrational coupling, the nuclear potentials corresponding to the ground (S_0) and electronically excited (S_1) molecular states are shifted harmonic wells of frequency ω_0. The shift is quantified by the *Huang-Rhys factor*, λ^2.

As a consequence of the coupling of the electronic states to vibrational modes, several vibronic states are formed, and instead of two discrete energy levels as discussed above, bands of states with distance approaching zero are created. The individual bands are separated by the energy of the main vibrational mode, which is the carbon-carbon symmetric stretch mode with an energy of $\hbar\omega_0 \approx 0.17\,\mathrm{eV}$. The width of the

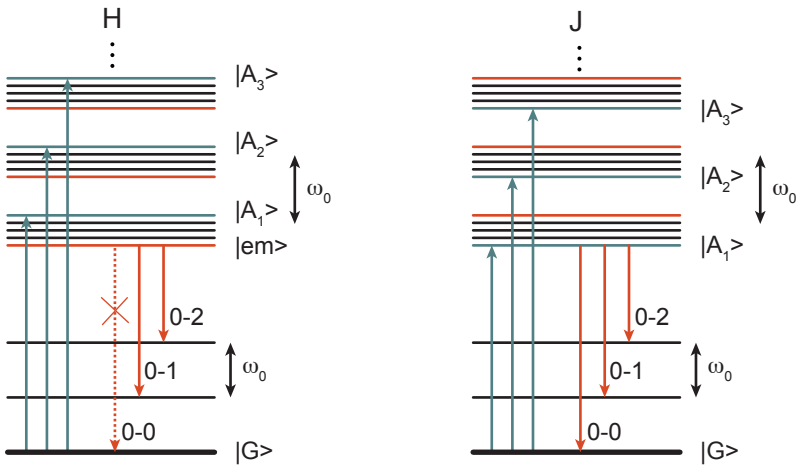

Figure 2.7.: Level diagrams of H- and J-aggregates in the weak coupling regime. (adapted from [42])

bands depends on the strength of the electronic coupling between neighbouring chromophores, expressed in the energetic shift of the $k = 0$ (phonon-less) exciton, $J_{k=0}$. The exciton bandwidth, W, then becomes $W = 2\,|J_{k=0}|$. As discussed above, for H-aggregates the $k = 0$ hereby is located at the top of the band (at higher energy then the monomer), the sign of the coupling therefore positive. For J-aggregates, the sign of the coupling is negative and the $k = 0$ exciton resides at the bottom of the band. The width of the exciton bands is therefore directly connected to the strength of the coupling. Depending on the size of W, different cases are considered: weak coupling ($W < \lambda^2\hbar\omega_0$), intermediate coupling ($W \approx \lambda^2\hbar\omega_0$), or strong coupling regime ($W \gg \lambda^2\hbar\omega_0$). The above description for the case of weak coupling is illustrated in Figure 2.7. The arrows mark excitations due to optical absorption of a photon as well as allowed optical transitions back to the ground state under photon emission.

The above approach for the description of polymer assemblies as H- or J-type aggregates has been successfully applied to the photophysical response of a range of real world systems, including poly(3-hexylthiophene). A more detailed introduction to this material and the application of the H- and J-aggregate model to describe the optical absorption follows in the next section. A more extensive investigation of the photoluminescence of P3HT can be found in the second result chapter (Chapter 4).

2.4. Poly(3-hexylthiophene)

Poly(3-hexylthiophene) (P3HT) is one of the most intensively investigated materials among soluble π-conjugated polymers. Due to its facile processability, high charge carrier mobility, and environmental stability it has become a key material for research on organic field-effect transistors and organic solar cells. [6, 7, 18, 46–51]

The P3HT polymer chain is made of a π-conjugated polythiophene backbone with hexyl side chains attached at the 3-position of the thiophene monomers to improve solubility. Three different possibilities exist to couple the monomers at their 2- and 5-positions, namely head-tail, head-head, or tail-tail. The regioregularity of the polymer chain strongly affects the crystallinity of the film. [50] This is because the chemical incompatibility of the side chains with the polymer backbone results in the tendency to form a self-assembled structure, in which stacks of polymer backbones alternate with layers of more or less ordered side chains. [52–54] The self-arrangement of aromatic molecules in a *face-to-face* orientation is due to non-covalent, attractive interactions of their π-systems, and therefore referred to as *π-stacking*. [55] The exact nature of these attractive interactions of the negatively charged electron clouds is still not completely understood, but results mainly from electrostatic interaction and dispersion forces arising from induced multipoles in the molecules. [56, 57]

Figure 2.8 illustrates the structure of the π-stacks for P3HT. The distance a between the π-stacks, often called *lamella stacking distance*, is mainly defined by the length of the side chains, but depends also on the weight-average molecular weight of the P3HT, and is typically in the range of 1.55 - 1.7 nm. [58] Furthermore, it has been found that P3HT can exist in two different crystal structures, called *Type I* and *Type II*, which differ mainly by the side chain conformation. [54] While in Type II the side chains are interdigitated, no interdigitating is taking place in Type I P3HT, resulting in a larger lamella stacking distance a. Type I is the thermally stable structure that is usually obtained when P3HT is cast or spin-coated from chlorinated solvents. Type II is less common and has just been reported for specific solvent drying conditions, very low molecular weight P3HT, and involving the application of pressure. [59–61] Also the π-stacking distance (distance b) varies for both structures, with 0.38 nm for Type I and a 0.43 nm separation for Type II. [62]

Besides the aforementioned importance of macromolecular properties, the morphol-

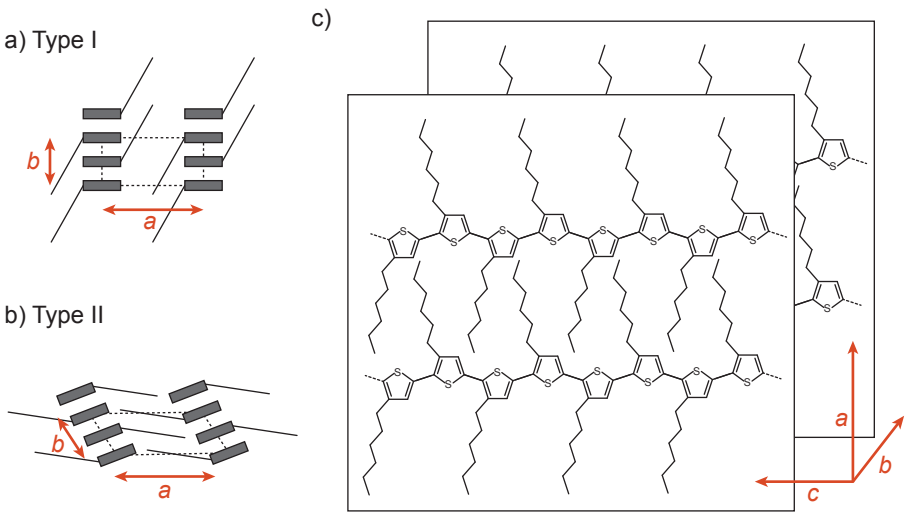

Figure 2.8.: Illustration of the self-assembly of P3HT polymer chains by π-stacking. (a) and (b) show two known structures, Type I and Type II, characterised by different stacking distances and the difference in interdigitation of the alkyl side chains (adapted from [30])). Distance a is the lammellar spacing, b the π-stacking distance, and c points in the direction of the long axis of the polymer chain. (c) shows how the polymer chains assemble in the case of interdigitating side chains.

ogy of thin-films also crucially depends on processing conditions like solution preparation method (e.g. solvent used and processing temperature), deposition method (drop-casting, spin-coating, film drying conditions), and the nature of the used substrate. [15, 63–67] Thermal annealing after deposition further changes the nanomorphology of the film. However, it has been observed that spin-coated films of P3HT in general are made of a network of crystalline domains embedded in a matrix of amorphous material. [7]

The short distance between polymer backbones forming the π-stacks results in a strong overlap of the molecular orbitals in this direction, while the overlap along the lamellar direction is significantly smaller. This leads to a large anisotropy of charge transport and strong polarisation effects of optical absorption and emission within the crystalline domains. Furthermore, these nanocrystallites preferentially orient with one molecular surface in contact with the substrate, being isotropic in two rather than

three dimensions of the film. Slow deposition orients molecules *edge-on*, with the π-stacking parallel to the substrate plane. Depositing material faster, e.g. by the use of low boiling-point solvents and high spin-coater speeds or by friction transfer results in a *face-on* orientation of the molecules. [46, 68]

Optical Absorption of P3HT Films Spano *et al.* developed a theoretical model that has been shown to be well suited to explain the optical absorption spectra of P3HT films. [40] He could derive a mathematical expression that relates the strength of the excitonic coupling, $J_{k=0}$, to the relative intensity of the lowest energy absorption peaks, $R_{abs} = I_{abs}^{0-0}/I_{abs}^{0-1}$,

$$R_{abs} = \frac{\left(1 - 0.48 J_{k=0}/\left(\hbar\omega_0\right)\right)^2}{\left(1 + 0.146 J_{k=0}/\left(\hbar\omega_0\right)\right)^2} \ . \tag{2.19}$$

This equation is strictly valid in the weak coupling regime, assuming a Huang-Rhys factor of 1. It predicts an increase of R_{abs} with decreased coupling strength for H-aggregates ($J_{k=0} > 0$), and a decrease of R_{abs} with increasing $J_{k=0}$ for J-aggregates. This change in relative absorption strength can be explained by an increased inter-band mixing with increasing $J_{k=0}$ and a resulting redistribution of oscillator strength to higher energy for H-, and lower energy for J-aggregates. The shift of line intensity of the 0-0 and 0-1 absorption peaks from the isolated molecule to the aggregate therefore provides a good test for the type of aggregation, whether H-type of J-type.

It has been found that the excitonic coupling strength and hence W is influenced by the exciton coherence length. More precisely, an increased exciton coherence length leads to a decrease in W. This behaviour is not intuitive but has been shown experimentally by comparing the absorption spectra of P3HT films cast from different boiling point solvents. [45]

Like the optical absorption, also the photoluminescence spectra of P3HT films spin-cast from low boiling point solvents can be explained well with the model of weakly coupled H-aggregates. Deviations have been reported recently for high molecular weight P3HT and for individual, self-assembled P3HT nanofibres. Since the photoluminescence of P3HT films and P3HT nanofibres constitutes the main topic of one of the Chapters later on in this work (Chapter 4), a more detailed introduction covering the PL characteristics of H- and J-aggregates will be given within the scope of that Chapter (see Section 4.1).

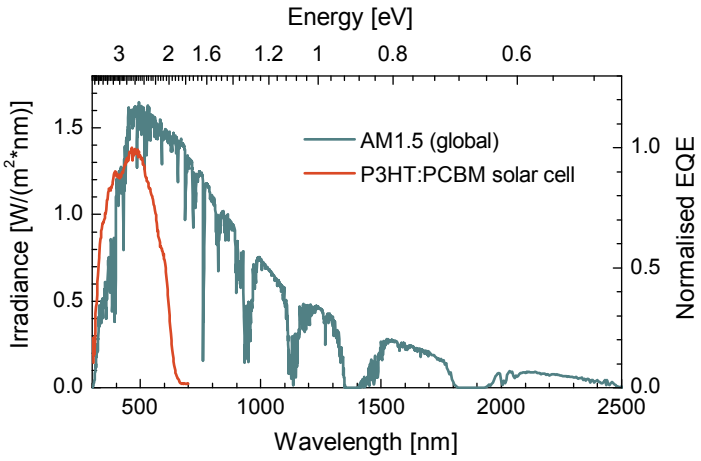

Figure 2.9.: Comparison of a standard AM1.5 solar spectrum and the EQE of a typical polymer solar cell, using a P3HT:PCBM bulk heterojunction.

2.5. Organic Photovoltaics

2.5.1. Exciton Dissociation

The possibility to control the optical and electrical properties by chemical synthesis makes organic semiconductors interesting for the use in optoelectronic devices like solar cells. The high extinction coefficient over a large wavelength range allows the absorption of a considerable part of the solar spectrum with the use of films with a thickness of just 100 nm - 200 nm. Figure 2.9 shows the solar spectrum after travelling through the Earth's atmosphere, representative for temperate latitudes (*air mass coefficient* of 1.5, i.e. AM1.5). The graph also shows the response of a typical organic solar cell. As described above, since the excitation of a molecule leads to a quick relaxation into the lowest excited state, excessive energy will be converted into heat, and can therefore not be harvested in electrical energy. Reducing the optical gap to broaden the wavelength range in which the molecule will absorb will therefore result in the loss of the energy of high-energy photons. This thermalisation process constitutes a major limitation of the efficiency of photovoltaic devices. Improvements can be achieved with tandem architectures, where multiple absorber layers with different energy gaps are stacked on top of each other.

To generate an electrical current from an optical excitation, the excitons formed on the absorber material of a solar cell need to be split into free positive and neg-

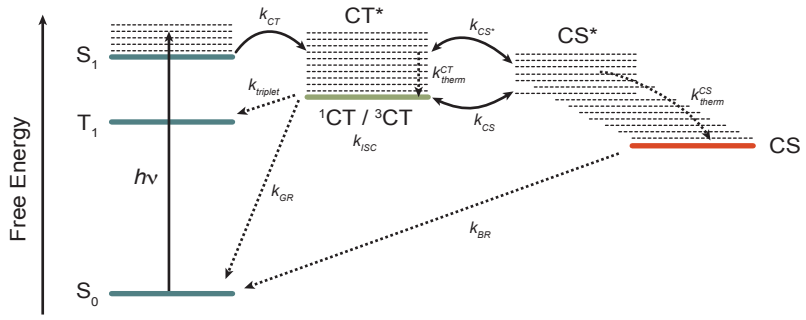

Figure 2.10.: Energy level diagram summarising the main processes involved in charge photogeneration. (adapted from [69, 70])

ative charge carriers. The fundamental processes involved in this are illustrated in Figure 2.10.

Light being absorbed from the singlet ground state creates a higher energy excited state, which quickly relaxes into the lowest excited singlet state (S_1). In most hydrocarbons featuring no heavy atoms and a coplanar structure, intersystem crossing to the triplet manifold is relatively small. [71] The generated exciton can then diffuse through the organic layer. To be split into charge carriers, it needs to find a site with an energetically lower lying charge-transfer state (CT-state). [70] This state forms at the interface of an electron donor and an electron acceptor material (D/A interface). The molecular nature of the CT-state is not completely understood yet. It is characterised by a broader localisation of the exciton and is often pictured as the hole being located on the donor and the electron located on the acceptor, while both charges are still strongly Coulombically bound. [72] To completely dissociate into the charge separated state (CS), this energy barrier has to be overcome. There is experimental evidence that the dominating dissociation process is extremely fast (in the range of femtoseconds) and the CT-CS transition takes place before the excitons thermally relax to the CT ground state, so that the excessive energy of the 'hot excitons' helps to overcome the Coulombic barrier (k_{CS^*}). [73–75] However, the important role of hot excitons for efficient charge dissociation is not completely understood and there is also evidence that shows that excitons with excess energy do not lead to improved charge separation. [76]

Once the charges have been separated, they move toward their respective elec-

trodes. The efficiency of this process is mainly dependent on the mobility of the hole conducting and electron conducting material as well as on charge recombination processes. [77] Both factors are strongly connected to the morphology of the layers and can vary significantly.

2.5.2. Design of Photovoltaic Devices

A basic device structure of an organic solar cell features an active layer sandwiched between a transparent and a reflective electrode. Most commonly, the transparent electrode is a layer of *indium tin oxide* (ITO) sputtered on a glass substrate. As top electrode, low work function materials like calcium or aluminium are used. [78]

In the simplest case, the active layer consists of a single polymer layer. This device corresponds to a *metal-insulator-metal* (MIM) diode. In forward bias, electrons are injected from the low work function and holes from the high work function electrode. Due to the asymmetrical work functions of the electrodes, the current under reverse bias will be orders of magnitudes smaller. This rectifying character can be accompanied by a radiative recombination of the injected charge carriers, resulting in a light-emitting diode. If photoinduced free charge carrier generation is allowed, the device exhibits a significant photocurrent under reverse bias. Using the device for photodetection under reverse bias, the potential difference between the electrodes has to be high enough to overcome the Coulomb attraction of the generated excitons. Otherwise, the photogenerated excitons will decay geminately, either radiatively (i.e. photoluminescence) or non-radiatively. [70] When operated as a photovoltaic device, where no external voltage is applied and open-circuit conditions exist, the potential difference available in the MIM device is caused by the difference in the work function of the metal electrodes. In most cases (e.g. ITO and Al), the potential difference due to this work function difference is not high enough to give efficient photoinduced charge generation, limiting the operation of the photovoltaic cells.

To overcome this limitation, a dual molecule approach, using a donor and an acceptor material, has been developed. [79] Figure 2.11 shows the energy level diagram of such a donor-acceptor bulk heterojunction device, illustrating the operation principle. All processes involved occur with a certain efficiency η, determining the overall external quantum efficiency (EQE) of the device. Photons enter the device through the

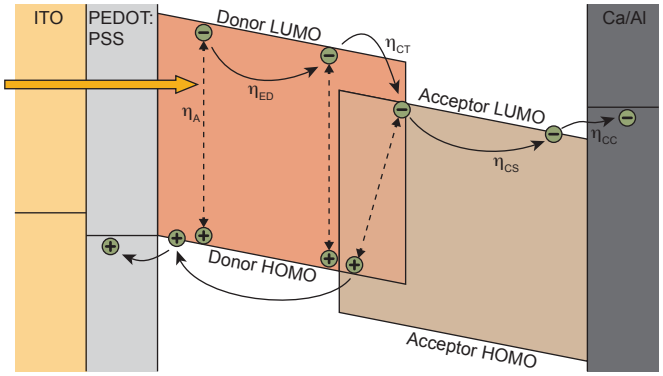

Figure 2.11.: Operating principle of a bulk heterojunction solar cell (adapted from [80]).

transparent ITO electrode and hole extraction layer (consisting of poly(3,4-ethylenedioxythiophene) poly(styrenesulfonate), PEDOT:PSS) where they get absorbed, predominantly in the donor layer, leading to the formation of an exciton (absorption efficiency η_A). For efficient dissociation, the exciton then has to diffuse to the donor-acceptor interface within its lifetime, where the transition to the CT state can take place (exciton diffusion efficiency η_{ED}, compare also Figure 2.10). From this state, the exciton can dissociate into free charges (charge separation efficiency η_{CS}), which will travel to the respective electrodes (charge collection efficiency η_{CC}). [80] This results in an overall efficiency of

$$EQE(\lambda) = \eta_A(\lambda) \times \eta_{ED}(\lambda) \times \eta_{CS}(\lambda) \times \eta_{CC}(\lambda) \; . \tag{2.20}$$

The EQE is often called *Incident Photon to Current Efficiency* (IPCE), since it can be seen as the ratio of the number of incoming photons of a certain wavelength to the number of extracted electrons. Most commonly, the performance of a photovoltaic device is stated as the power conversion efficiency $\eta = P_{max}/P_{in}$, the ratio of the maximum output power to the power of the incoming irradiation. It can also be expressed as

$$\eta = \frac{V_{OC} \cdot I_{SC} \cdot FF}{P_{in}} \; , \tag{2.21}$$

where V_{OC} is the open-circuit voltage, I_{SC} the short-circuit current, and FF the fill-factor of the device.

V_{OC} is directly linked to the energy difference between the HOMO level of the

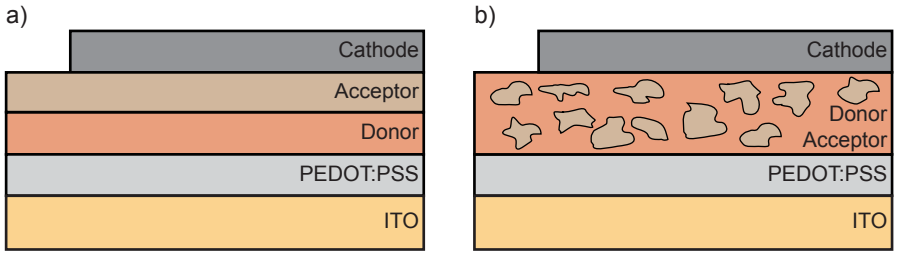

Figure 2.12.: Comparison of two fundamental device architectures, (a) a bilayer structure, and (b) a bulk heterojunction.

donor and the LUMO level of the acceptor. *Scharber et al.* have found that it can be expressed by the empirical equation

$$V_{OC} = \frac{1}{e}\left(\left|E_{HOMO}^{donor}\right| - \left|E_{LUMO}^{acceptor}\right| - 0.3\,\mathrm{eV}\right) , \tag{2.22}$$

where e is the elementary charge and E is the energy level. [81] Since a higher V_{OC} will directly increase the efficiency of the solar cell (Equ. 2.21), the position of the energy levels is of great importance and needs to be considered when materials are developed.

I_{SC} is mainly dependent on the integral of the product between cell responsivity and incident solar spectral irradiance (i.e. the overlap between EQE and solar spectrum, compare Fig. 2.9). Therefore, the most powerful strategy to achieve high I_{SC} is to narrow the band gap to cover a wider range of the solar spectrum. Other parameters, such as carrier mobility, intermolecular interactions, and molecular chain packing also affect I_{SC}.

The third parameter in Equation 2.21 that has to be maximised to achieve high power efficiency is the fill-factor (FF). The FF is affected by many factors, such as charge carrier mobility and balance, interface recombination, series and shunt resistances and film morphology. [82, 83] It acts as a sensitive indicator for these influencing factors, however, the exact effect on the FF for many parameters is still not understood.

The quest for high efficiencies has led to two basic solar cell designs. As illustrated in Figure 2.12 (a), the donor and acceptor layer can be deposited successively, resulting in a bilayer structure. The advantage of this structure is that the processing conditions for both materials can be controlled and optimised individually, to achieve

a high mobility for the respective charge carrier type, so the charge collection efficiency η_{CC} can be high. Nevertheless, a bilayer structure offers just a small interface area between donor and acceptor, where the dissociation of excitons can efficiently take place. The limited amount of charges generated is the main reason for the comparatively low efficiency of this device structure. The problem of a small interface area can be overcome if donor and acceptor are blended in one layer, forming a bulk heterojunction (Figure 2.12 (b)). This structure can offer a large interface area if the processing is optimised to result in the right domain size, which ideally has to be within the exciton diffusion range (typically $\approx 10\,\mathrm{nm}$). In addition to the importance of phase separation, charge transport out of domains of one component which is surrounded by the other can be a problem. In highly efficient systems, the two materials are often not completely segregated, but mixed phases where both holes and electrons can be transported exist.

The bulk heterojunction concept has led to remarkable results, with power conversion efficiencies approaching 10 %. [13] Most commonly, the materials are deposited from solution, but also the deposition of small molecules by thermal evaporation in vacuum has led to equally good results. [84] As an acceptor material, fullerenes became a standard, while a wide range of donor materials have been investigated. A major breakthrough was the discovery of soluble thiophenes, most importantly P3HT. [6] With this system, efficiencies of 4-5 % could be achieved after careful optimisation of the morphology. [8] Although other materials could exceed this performance, P3HT:PCBM became a popular system both for fundamental research as well as for first large-scale applications. [85, 86]

Since this work is focused on P3HT, a more detailed summary of the optical and electrical properties of this material is presented in the following chapter.

3. Fabrication and Properties of Polythiophene Nanofibres

3.1. Introduction: Nanofibre Formation of P3HT

The self-assembly of polythiophene chains on a nanoscale and the orientation behaviour of the crystallites in the film have sparked interest to increase the order of polythiophenes on a larger length scale. In 1993, *Ihn* and coworkers first described that polythiophenes can form macroscopic structures in the shape of long whiskers of the length of several micrometres. [20] They discovered that these structures form when a warm solution of the polymer in a poor solvent is slowly cooled to room temperature, and that the observed colour change of the solution from light orange to dark red, which was previously referred to as thermochromism, [87] was related to an increased crystallinity.

Their method of slowly cooling a solution of P3HT in a poor solvent was further investigated by other groups, [23–25] and alternative techniques to grow nanofibres from solution were developed, which often involve the addition of a suitable non-solvent to a solution of P3HT such as hexane, [88, 89] acetonitrile, [90, 91] and nitrobenzene. [92]

This chapter reports on a nanofibre (NF) formation process in which di-tert butyl peroxide (DTBP) is used as an additive to a solution of P3HT in chlorobenzene. It will be described how this technique can be used to control the crystallinity of P3HT films as well as to gain control over the degree of insolubility of the films. The possibility to fabricate insoluble films is of advantage for the fabrication of solar cells, since it allows the successive deposition of a second layer from a similar solvent, which can be used to obtain better control over the formation of the bulk heterojunction of the solar cell. This application will be discussed in more detail in Chapter 5.

Although the focus of this chapter lies on the NF formation using DTBP, some results reported concern the formation process using a method of slow cooling in toluene. During slow-cooling, the material is dissolved in a poor solvent at elevated temperature, and the solution then cooled to room temperature, falling below the solubility limit and thereby forcing the material to aggregate. Given suitable conditions with regard to solvent choice, polymer concentration and temperature, it has been shown that this method can lead to the formation of P3HT NFs of different quality. [93] According to *Roehling et al.*, the use of toluene as a solvent results in NFs with fewest stacking faults and high planarity of the polymer backbone inside the fibres. [93] For some measurements in this chapter, the method of slow cooling in toluene is used as a comparative technique to the fibre growth using DTBP as additive. Since this method is of importance for the photoluminescence studies reported in Chapter 4, some results about the formation process and characterisation of the NFs are included in the following sections.

3.2. Experimental

3.2.1. Materials

All materials used in the following experiments, including the solvents chlorobenzene and toluene, were purchased from *Sigma Aldrich* and used without further purification. The P3HT powder (Prod. Nr.: 698997, M_n=54,000-75,000 g/mol, > 98 % head-to-tail regioregular) was stored in inert gas atmosphere, while solution preparation took place in ambient conditions. DTBP (Prod. Nr.: 168521) was stored in ambient conditions at low temperature ($\approx 5\,^{\circ}$C).

Di-tert-butyl peroxide (DTBP)

DTBP is one of the most stable organic peroxides and a light yellow transparent liquid at room temperature. At elevated temperatures above 100 °C it undergoes homolysis, meaning the breakdown of the relatively weak oxygen-oxygen bond, generating two radicals. This process is shown in Figure 3.1. Because of this behaviour, peroxides are commonly used in rubber industry as a radical initiator to crosslink polyethylene. [94, 95]

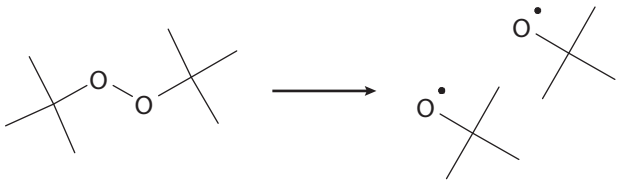

Figure 3.1.: Chemical structure of DTBP and its decomposition reaction at elevated temperatures.

In 2009, *Gearba* and coworkers reported on the use of DTBP to thermally crosslink P3HT. [21] They explain that upon annealing at 150°C the DTBP-radicals attack mainly the alkyl sidechains of P3HT, where they remove hydrogen atoms. This leads to bonds between different polymer chains, while the conjugated system of the polymer backbone remains unaffected. This process would form an interconnected network of polymer chains, resulting in insoluble films. By adding DTBP directly to a solution of P3HT in chlorobenzene, and by annealing the films spin-cast from this solution, Gearba et al. indeed observed the films to become insoluble with increasing peroxide concentration. They also proved a higher crystallinity of the film and a higher conductivity as well as a slight blue-shift of the absorption spectrum, and they concluded that the crosslinking process indeed takes place as expected.

However, as the following sections will show, the phenomena observed by Gearba et al. can be well explained by a process involving the formation of nanofibres upon addition of DTBP to a solution of P3HT, and it is unlikely that an actual crosslinking process of the alkyl side chains takes place.

3.2.2. Sample Preparation and Characterisation

Solutions of P3HT were prepared in ambient conditions by weighing the needed amount of polymer in a small vial and adding the required amount of solvent.

Nanofibre growth by addition of DTBP

A solution of 10 mg/ml P3HT in chlorobenzene was prepared by dissolving the material on a stirrer / hot plate at a temperature of 70 °C. The solution was then cooled to room temperature while stirring at low speed ($\approx 100 - 200$ rpm). DTBP was then added dropwise and the vial shaken in between to avoid local precipitation. After ad-

dition of DTBP, the vial was left on the stirrer for at least 2 h to allow the formation of NFs.

Nanofibre growth by slow cooling in toluene

A solution of P3HT ($\approx 0.5\,\mathrm{mg \cdot ml^{-1}}$) in toluene was prepared by dissolving the material in a vial that was kept in a heated water bath at 100 °C, until the material was dissolved and the solution showed a light orange colour. The heater was then gradually turned down over a period of ≈ 2 h, and the water bath slowly cooled down to room temperature. The solution was then left at room temperature for at least 12 h before it was centrifuged twice to remove non-aggregated material.

Absorption Spectroscopy

UV-vis absorption measurements in solution ($\approx 10^{-3}\,\mathrm{mg \cdot ml^{-1}}$) were performed in a cuvette with an optical path length of 4 mm. Film samples were prepared on fused silica substrates that were cleaned in a bath of acetone and subsequently in isopropanol with ultrasonication for about 10 min each and dried in a stream of nitrogen. The material was deposited by spin-casting at 2000 rpm in ambient conditions.

Absorption measurements were performed using a photo-spectrometer *Agilent 8453*. The system features a combination of a tungsten lamp and a deuterium lamp and covers a wavelength range from 190 nm - 1100 nm. For detection, the light is dispersed by a grating onto a photodiode array.

Surface Topography by AFM and Profilometry

An atomic force microscope (AFM) consists of a cantilever with a sharp tip (probe) at its end that is used to scan the sample surface. [96, 97] The cantilever is typically silicon or silicon nitride with a tip radius of curvature on the order of nanometers. When the tip is brought into proximity of a sample surface, forces between the tip and the sample lead to a deflection of the cantilever. The interaction between the tip and the sample involves a wide range of forces, such as mechanical contact force, van der Waals forces, capillary forces or electrostatic forces. The deflection of the probe is measured using a laser spot reflected from the top surface of the cantilever into an array of photodiodes.

The AFM can be operated in a number of modes, depending on the application. Possible imaging modes are divided into contact modes and a variety of dynamic (non-contact or tapping) modes where the cantilever is oscillating close to its resonant frequency. For soft samples like polymer-films, operation in tapping mode is often preferred, since this reduces the risk of causing damage to the sample. While scanning the sample surface, a feedback mechanism is employed to adjust the tip-to-sample distance to maintain a constant force between the tip and the sample. The tip is mounted on a vertical piezo scanner while the sample stage is being scanned in x- and y-direction. The resulting map of points $z_i = f(x_i, y_i)$ represents the topography of the sample and can be visualised by colour-coding the numerical values for z. A meaningful parameter to describe the surface is its root mean square roughness R_q, which can be calculated from the individual, equally spaced heights of the individual pixels, z_i, by

$$R_q = \sqrt{\frac{1}{n}\sum_{i=1}^{n} z_i^2}\,. \tag{3.1}$$

In the presented work, a *Dimension AFM* from *Veeco Instruments* was used in tapping mode, using cantilevers from *MikroMasch* (type *NSC35*). The substrates used were either fused silica slides as described above for absorption measurements, or Si / SiO_2 substrates that were cleaned in isopropanol with ultrasonication for about 5 min prior to material deposition by spin-casting or drop-casting.

Similar to the cantilever in an AFM in contact mode, a profilometer uses a diamond stylus that is moved across the sample for a specified distance and specified contact force.[1] The vertical displacement of the stylus z is measured in dependence of its horizontal position. A profilometer has a high vertical resolution of a few nanometers, but the lateral resolution is limited by the relatively big size of the stylus. Nevertheless, its scanning speed is much higher than the one of an AFM, which makes it suitable for surface characterisation on macroscopic length scales (up to several millimetres). Similar to the AFM, a root mean square surface roughness R_q can be calculated from the measured values for z using Equation 3.1.

[1] The profilometer used in this work is a *Dektak 3* from *Veeco Instruments Inc.*

GIXRD and XPS Measurements

Grazing incidence X-ray diffraction (GIXRD) measurements were performed with a *Rigaku Ultima IV type III* diffractometer (Rigaku, Tokyo, Japan) equipped with cross beam optics (CBO) by using a K_α wavelength emitted by a Cu anode. Careful alignment of source and detector with respect to the sample was reached by using a thin-film attachment with three degrees of freedom. In order to avoid beam defocusing, the measurements were carried out in parallel beam mode. Divergence of the primary beam was reduced by a 5 ° Soller slit, while divergence of the diffracted beam was reduced by a 0.5 ° horizontal Soller slit. The incident angle was kept at 0.5 ° to avoid any significant scattering from the substrates. XPS measurements were performed with a *ESCALAB IIB* spectrometer (VG Scientific Ltd., UK), using the Al K_α line at 1486.6 eV. Pass energy for wide scans was 50 eV and 20 eV for high resolution scans. All the binding energy (B.E.) values are referenced to the aromatic C 1s band at 284.6 eV. Integration of the XPS bands was carried out using the CasaXPS software.

3.3. Results

3.3.1. Fibre Formation in Solution

The method of using a suitable additive as an initiator to NF growth has the advantage that the fibres can be formed in a solvent that is normally used for the processing of P3HT, which also allows the use of a second material to dissolve in the same solution, like e. g. an acceptor material like PCBM for the use in solar cells. Furthermore, the amount of additive added to the solution presents another parameter which allows control over the formation process, which will be explored in this chapter.

The additive used in this work is di-tert butyl peroxide (DTBP). This material has been suggested as a thermal crosslinking agent for P3HT, since the use of DTBP results in insoluble films. [21] It will be shown in the following sections, that the underlying process behind the insolubilisation is a formation of NFs.

One way to directly observe the formation of nanofibres is by monitoring the UV-vis absorption of a dilute solution. Figure 3.2 shows the absorption spectra of a solution

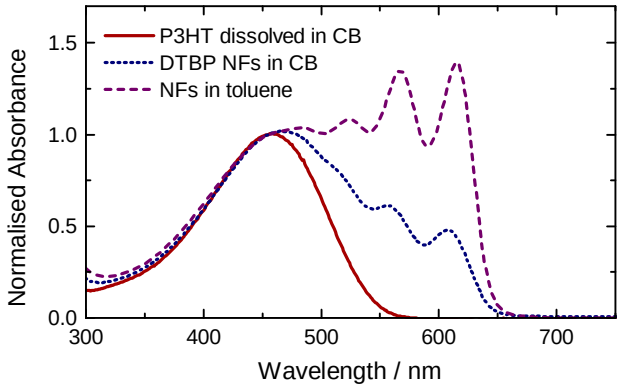

Figure 3.2.: Absorption spectra of a solution of P3HT dissolved in chlorobenzene, a dilute solution of DTBP-grown fibres in chlorobenzene, and a toluene solution with fibres grown by slow-cooling in this solvent.

of P3HT dissolved in chlorobenzene, together with two spectra of solutions in which NFs were grown. It can be seen that the spectrum of dissolved P3HT consists of one broad absorption peak around 455 nm, while the nanofibre solutions are characterised by the emergence of additional absorption peaks at higher wavelength.

These peaks, that are absent for the dissolved P3HT, indicate the formation of aggregates. The ratio of the two lowest energy absorption peaks, $A_{0-0}/A_{0-1} = R_{abs}$, is related to the strength of the excitonic coupling in the aggregate, as described by Equation 2.19. For H-type coupling ($J_{k=0} > 0$), R_{abs} goes towards 1 as $J_{k=0}$ decreases. As can be seen in Figure 3.2, for the dispersed toluene grown fibres, R_{abs} is slightly larger than 1, indicating very weak intermolecular coupling for this case.

It can also be seen in Figure 3.2 that the spectra of both fibre samples show a significant contribution of dissolved material to the absorption. This indicates that in both cases a significant fraction of non-aggregated material is still present in the solution. The amount of aggregated content is higher for the toluene sample than it is for the DTBP sample. This is mainly because chlorobenzene is a good solvent for P3HT, and with dilution of the fibres for absorption measurement in CB, a significant amount of the fibres is expected to re-dissolve. Toluene on the other hand is a poor solvent for P3HT, and hence, the fibres are more stable in this solution.

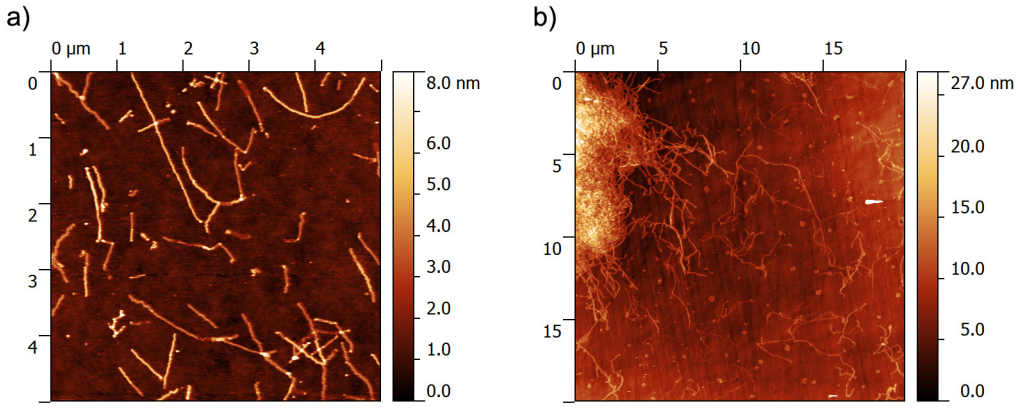

Figure 3.3.: AFM images of NFs fabricated by addition of DTBP to a solution of P3HT in CB. (a) Separated fibres, showing the variation in length. (b) If deposited from solution with higher concentration ($\gtrsim 10^{-3}$ mg/ml), the tendency of the NFs to form larger bundles becomes visible.

3.3.2. Fibre Shape and Dimensions

To find out about the actual shape of the nanofibres, solutions of dilute fibres in solutions were spin-cast on silicon substrates. Figure 3.3 shows AFM images of two samples that highlight two important properties of solution-grown nanofibres. Figure 3.3 (a) shows that the fibres can be successfully separated into individual fibres. While being nanometre-sized in height and width, the length of these fibres can exceed several micrometres. Figure 3.3 (b) shows, how individual fibres can form bigger aggregates, or fibre bundles. The bundle in the left hand side of the image has a diameter of about 10 μm. The size of the bundles varies and can be bigger than the one shown here. They are expected to form in solution already, and are more likely to occur at high concentration ($\gtrsim 10^{-3}$ mg/ml) in the solution. Nevertheless, the individual fibres surrounding the bundle as well as the fibres in Figure 3.3 (a) demonstrate that P3HT NFs can be successfully separated by lowering the concentration in the solvent.

Figure 3.4 allows a more accurate determination of the NF dimensions. Figure 3.4 (a) shows an AFM image of an area where fibres of different height are visible. The height profiles at different location is extracted and plotted in Figure 3.4 (b). The height in this graph is shown in nanometres as well as in multiples of lamella stacks, with a

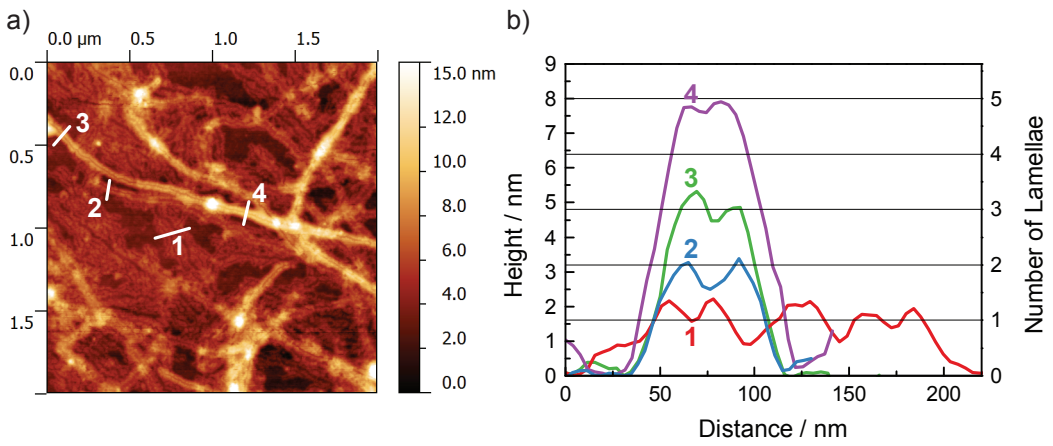

Figure 3.4.: (a) High resolution AFM image of NFs on a SiO_2 substrate, allowing the determination of their height and width. Cross-sections were taken at different positions, indicated by the white lines, and the profiles plotted in (b). To determine the number of lamella stacks, a lamella stacking distance of 1.6 nm was used.

distance of 1.6 nm typical for P3HT (compare Fig. 2.8 and Sec. 3.3.3). It shows that fibre-like structures are detectable that consist of as little as one layer of π-stacked polymer chains, up to 5 lamella-stacked layers, resulting in a height of about 8 nm. Interestingly, one single fibre can have segments of different height. Also, it appears as if a minimum of two π-stacked layers is required for the aggregate to take the shape of an extended nanofibre. The areas of single-layered stacks show up as more spread out, curled features.

Due to broadening effects of the AFM tip, it is not straight forward to accurately determine the width of the fibres. Measuring the distance at the top of the fibre, where the influence of the tip is smallest, the width can be determined to be about 30-50 nm. This assumes that the width towards the base of the fibre does not change but is a broadening effect attributed to the shape of the tip.

3.3.3. Control of P3HT Thin-Film Properties using DTBP as Additive

This section describes how DTBP can be used as an additive to a solution of P3HT in order to control the crystallinity and film retention of spin-cast films.

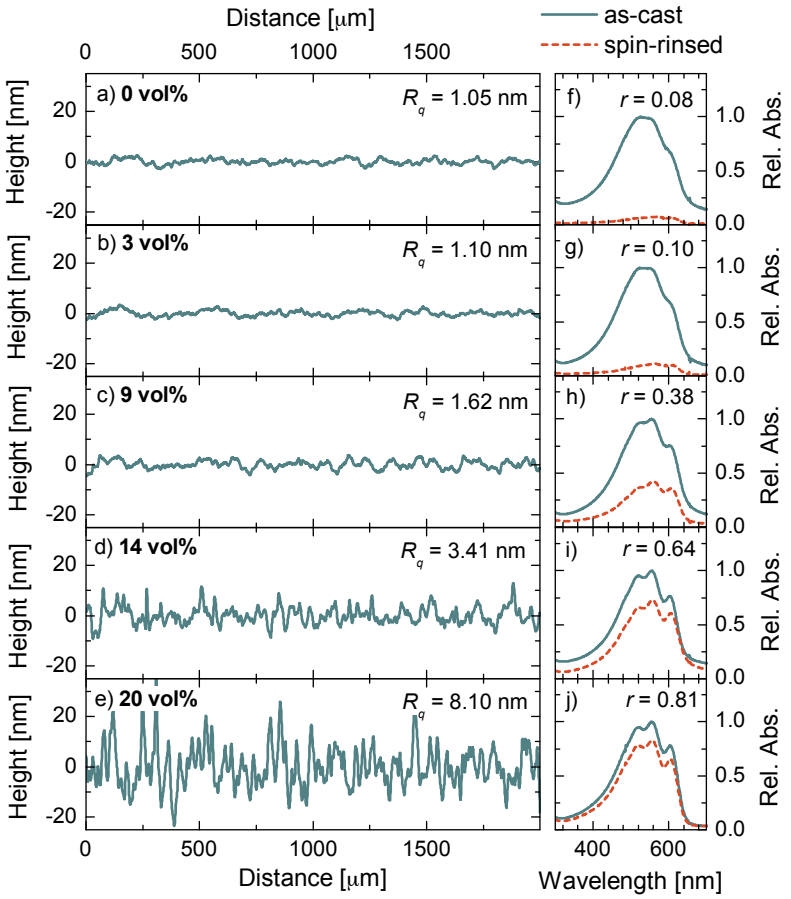

Figure 3.5.: Macroscopic surface profiles of P3HT films spin-cast from solutions with different DTBP concentration ((a)-(e)) and associated absorption spectra ((f)-(g)) of these films before (solid line) and after (dotted line) spin-rinsing with chlorobenzene. R_q is the calculated root mean square roughness of the surface. The film retention factor r is the ratio of the integrated area under the as-cast film and the spin-rinsed film.

Film Retention

To investigate the effect the addition of DTBP has on P3HT, solutions of P3HT with varying amount of peroxide were prepared, and films spin-cast on fused silica substrates. Figures 3.5 (a)-(e) show the macroscopic surface profiles of the films, scanned along a line of 2 mm, using the surface profilometer. The DTBP concentration, c_{DTBP}, was varied from 0 vol% to $c_{DTBP} = 20$ vol%. The root mean square

roughness R_q, calculated from the scans allows a qualitative comparison of the change in surface topography.

It can be seen that the profiles for $c_{DTBP} = 0$ vol% and $c_{DTBP} = 3$ vol% are virtually identical. The roughness starts to increase from a concentration of $c_{DTBP} = 9$ vol%, and at $c_{DTBP} = 20$ vol%, R_q reaches a value of 8.1 nm, with peak heights exceeding 20 nm. Using a film with such large variation in height in electronic devices bears the risk to create direct pathways between the electrodes. These direct pathways, or *shunts*, lead to a decreased fill-factor in solar cells and hence lower the efficiency of the device. [8, 98] It is in some cases possible to even out rough layers by making the following layers sufficiently thick. But increasing the layer thickness generally leads to higher series resistance, which will again lead to a reduction of the fill-factor and might additionally unfavourably influence the charge carrier balance. Since this work is motivated by potential applications in bilayer solar cells, and single layer thicknesses typically do not exceed 50 nm, a further increase in film roughness would not be feasible for these applications. Therefore, 20 vol% marks the highest concentration of DTBP used in this work.

In addition to the increased roughness, also the retention of the films increases. The graphs in Figures 3.5 (f)-(j) show the UV-vis absorption spectra of the films as-cast (solid line), and after they have been spin-rinsed with chlorobenzene (dashed line). To assess the degree of insolubility of the layer, a drop of chlorobenzene, wetting the whole surface of the substrate, was set on the film and after waiting for 1 min spin-rinsed at 2000 rpm. This procedure is similar to the deposition of a subsequent layer and hence a good test for the suitability for bilayer devices. The increase in viscosity upon addition of DTBP results in different film thicknesses for different peroxide concentrations, ranging roughly from 25 nm to 60 nm. Therefore, the absorption spectra were normalised to the absorption maximum, while the spin-rinsed spectra were divided by the same normalisation factor used for the as-cast spectra, allowing a comparison of the spectral shape and intensity. A retention factor r can be defined as the ratio of the integrated area from 310 nm to 750 nm under the as-cast (a/c) film and spin-rinsed (s/r) film, hence

$$r = \frac{\int_{310\,\mathrm{nm}}^{750\,\mathrm{nm}} A^{s/r}(\lambda)\, d\lambda}{\int_{310\,\mathrm{nm}}^{750\,\mathrm{nm}} A^{a/c}(\lambda)\, d\lambda} \,. \tag{3.2}$$

The absorption spectra in Figures 3.5 (f)-(j) show a clear dependence of the re-

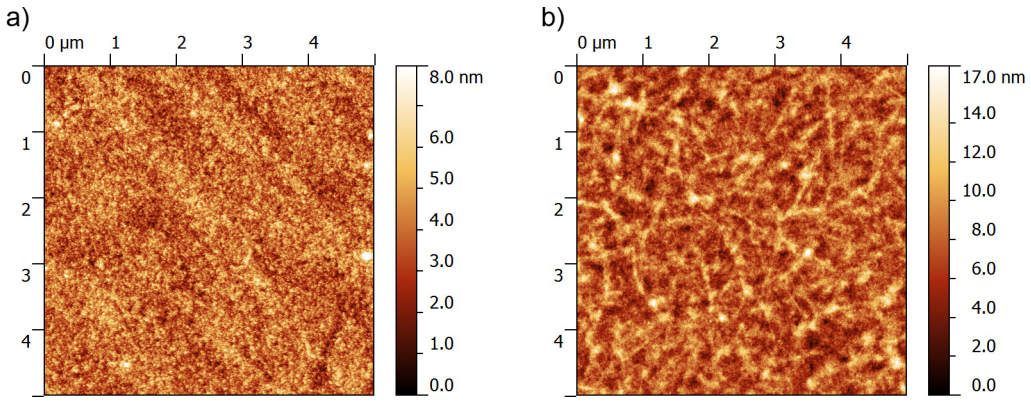

Figure 3.6.: AFM images of a film with P3HT spin-cast from a chlorobenzene solution (a), and a film spin-cast from a solution of with a 14 vol% content of DTBP (b).

tention factor on the DTBP concentration. Similar to the behaviour of the surface roughness, a concentration of $c_{DTBP} = 3$ vol% does not bring any change compared to the pure P3HT layer. In both cases, just about 10 % of the material remains on the substrate after spin-rinsing. This value increases to 38 %, 64 %, and 81 % for a c_{DTBP} of 9 vol%, 14 vol%, and 20 vol%, respectively. Furthermore, the shape of the absorption spectra changes with varying DTBP concentration, which is connected to an increase in crystallinity. This fact, as well as the correlation between surface roughness and retention, will be discussed in detail in the following section.

Figure 3.6 shows AFM images of a film of P3HT, spin-cast from chlorobenzene solution without additive (Fig. 3.6 (a)), compared to a film that has been deposited from a solution to which 14 vol% DTBP were added (Fig. 3.6 (b)). A clear difference can be seen in the surface morphology of the two films. The pristine P3HT film is almost without features and fairly flat (calculated root mean square surface roughness $R_q = 1.01$ nm). In contrast, the film from the solution with added DTBP shows an increased surface roughness ($R_q = 2.14$ nm) and it is apparent that it consists of a network of interwoven fibres.

Crystallinity

To gain further insight into the differences in microstructure of the two films, grazing incidence X-ray diffraction (GIXRD) was employed. Figure 3.7 shows the GIXRD

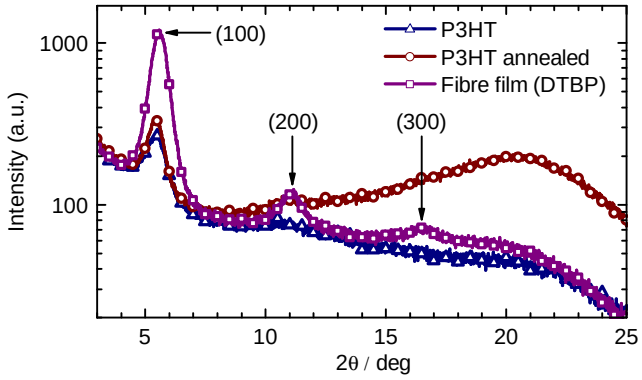

Figure 3.7.: GIXRD patterns of films of pristine P3HT, after annealing at 150 °C for 10 min, and spin-cast from a P3HT solution with 14 vol% DTBP.

patterns of films of pristine P3HT as-cast and after annealing for 10 min at 150 °C, and of a film from a P3HT solution with $c_{DTBP} = 14$ vol%. All three samples feature a clear diffraction peak at an angle 2θ =5.59 °, which can be assigned to the (100) reflection. [46] The intensity of this reflection is highest for the P3HT+DTBP sample which additionally shows the (200) and (300) reflections, which are both absent for the untreated and annealed P3HT samples. Both facts prove the significantly higher degree of crystallinity of the P3HT+DTBP sample compared to the films without DTBP. Annealing of the P3HT film leads to the emergence of a broad peak, centred at around 20 °, suggesting the formation of smaller and randomly oriented crystallites (this peak is often called the *amorphous halo*).

Using *Bragg's* law,

$$n\lambda = 2dsin\theta \ , \tag{3.3}$$

where n is an integer (the order of diffraction) and $\lambda = 1.54056$ Å the wavelength of the X-rays (Cu $K_{\alpha 1}$), it can be concluded from the location of the (100) peak at 2θ =5.59 ° that the distance d between the Bragg planes is 15.79 Å. This value is in agreement with values reported in literature, and can be assigned to the lamella stacking distance a (see Fig. 2.8). [25]. A distance of 15.79 Å indicates that the polymer chains assemble in a Type I configuration with non-interdigitating side-chains. No evidence for a Type II configuration is visible from the GIXRD spectra, since interdigitation of the side-chains would result in a shorter distance and hence in a reflection signal at larger angles. [54, 58] Furthermore, since the GIXRD setup

probes signals resulting from diffraction of a stacking direction perpendicular to the substrate plane (*out-of-plane* configuration), it can be concluded that the polymer chains are oriented in an 'edge-on' orientation. Since the diffraction signal in the direction parallel to the substrate (*in-plane*) could not be probed with the setup used, no clear conclusion can be drawn concerning the π-stacking distance (b in Fig. 2.8). Nevertheless, assuming the chains arrange in a Type I structure, this distance is known to be 3.8 Å. [25, 62]

Comparing the shape of the absorption spectra in Figures 3.5 (f)-(j) shows some clear differences which give evidence for a change in nanomorphology upon addition of DTBP. All spectra show three absorption peaks at around 520 nm, 555 nm, and 605 nm. In the case of a low peroxide concentration ($c_{DTBP} \leq 3\,\mathrm{vol\%}$), the transition peaks show a larger width, which merges the two peaks of low wavelength to one main central peak and a shoulder at 605 nm. For higher DTBP content ($c_{DTBP} \geq 9\,\mathrm{vol\%}$), the line width is decreased and the transitions become clearly visible as individual peaks.

Brown and coworkers found out that the absorption of films of regioregular P3HT cannot be explained with a simple Franck-Condon progression (compare Sec. 2.3), if it is assumed that the transition at 605 nm is the lowest energy *intra*chain excitation. [99] They conclude that this feature results from an *inter*chain aggregate excitation and its intensity is strongly correlated to the molecular order in the film. Spano and Clark could later successfully apply the H-aggregate model to explain the shape of the absorption spectra of P3HT thin films spin-cast from several solvents. [44, 45] Based on the formalism developed by Spano, they could show how the peak ratio of the lowest energy transition (the 0-0 transition) and the 0-1 transition, R_{abs}, can be used to determine a value for the exciton bandwidth W and hence for the intermolecular coupling and crystalline order of the material.

Using Equation 2.19 with $W = 2\,|J_{k=0}|$ gives

$$R_{abs} = \frac{I_{abs}^{0-0}}{I_{abs}^{0-1}} = \left(\frac{1 - 0.24\,W/(\hbar\omega_0)}{1 + 0.073\,W/(\hbar\omega_0)} \right)^2 \quad , \tag{3.4}$$

with $\hbar\omega_0$ being the 0.17 eV vibrational mode resulting from the symmetric C-C stretch (compare Sec. 2.3). For spin-cast films of P3HT, values for W typically range from 120 meV to 20 meV, depending on the boiling point of the solvent, film drying conditions, and molecular weight. [45] The DTBP-free case of Graph 3.5 (f) gives

c_{DTBP}	as-cast		spin-rinsed	
/vol %	R_{abs}	W/meV	R_{abs}	W/meV
0	0.68	99	-	-
3	0.68	99	-	-
9	0.75	75	0.84	46
14	0.77	68	0.83	49
20	0.77	68	0.79	62

Table 3.1.: Exciton bandwidth W for the as-cast and spin-rinsed films, as calculated from R_{abs} (Figs. 3.5 (f)-(j)) using Equation 3.4.

$R_{abs} = 0.68$, which corresponds to a bandwidth $W \approx 100\,\text{meV}$, which is in good agreement with the values found by Clark et al. [45] All values extracted from the absorption spectra of the as-cast and the spin-rinsed films for the various DTBP concentrations are summarised in Table 3.1. It is important to note that since the absorption spectra are a superposition of the crystalline (NF) phase and the amorphous phase, the calculated values for W are affected not just by the molecular order but also by the relative amount of crystalline to amorphous material. For the as-cast films it can be seen that W is decreased for concentrations of $c_{DTBP} \geq 9$vol% and shows the same value for both 14 vol% and 20 vol%. The value of 68 meV is still relatively large when compared to values reported for highly crystalline films of P3HT and suggests that there is still a significant fraction of the film in a non-aggregated, amorphous phase. This is also supported by the fact that after spin-rinsing, W decreases to 46 meV and 49 meV for $c_{DTBP} = 9$ vol % and 14 vol %, respectively. This shows that it is mainly the amorphous fraction of the film that gets washed away, hence the average crystallinity increases.

3.3.4. Effect of DTBP on P3HT

The DTBP molecule features two central oxygen atoms which are just weakly bound and responsible for the homolysis of the peroxide, i.e. the dissociation of the molecule into two radicals (see Fig. 3.1). Due to this process peroxides are commonly used as oxidising agents. Nevertheless, DTBP is one of the most stable peroxides, and to efficiently activate the homolysis a temperature above 100 °C is required. To see

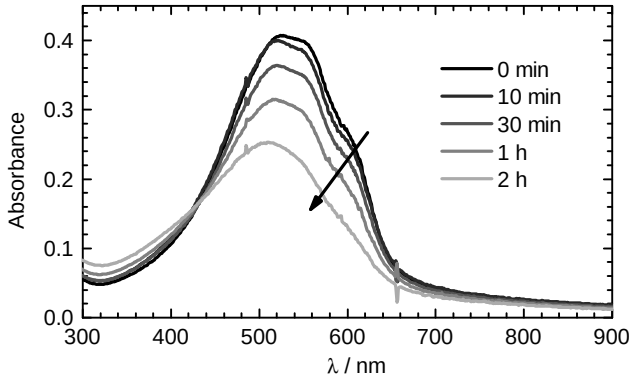

Figure 3.8.: Absorbance of a film of P3HT after annealing at 150 °C in DTBP vapour for a different amount of time.

the effect of DTBP radicals on P3HT, P3HT films were kept at a temperature of 170 °C in a vapour of DTBP for a varying amount of time. Figure 3.8 compares the absorption of the samples. Clear differences of the spectra are already apparent after a few minutes of exposure to DTBP. With increasing exposure time, the spectrum loses vibronic structure and shows a blue-shift of the absorption maximum. This indicates that the peroxide, if at a temperature above 100 °C, does effect the conjugated backbone and reduces the conjugation length of the system. It is most likely the sulfur in the thiophene rings that does get oxidised.

In contrast, if the peroxide is added to the solution and kept at room temperature, no sign of oxidation is visible from the UV-vis absorption spectra as shown in the graphs of Figure 3.5 (f)-(j). Also XPS measurements did not provide any indication for the incorporation of additional oxygen in the films upon addition of DTBP to the P3HT solution. In particular, Figure 3.9 (a) shows how the XPS spectrum of a pure P3HT film compares to a sample where DTBP was added to the solution. Both spectra are virtually identical, clearly showing signals that stem from the 2s and 2p electrons of the sulfur atoms and the carbon 1s signal. In both cases, no signal is detectable at an energy of 530 eV, where the oxygen 1s peak is expected. Furthermore, no sign of oxidation-related groups has been found both in the high resolution spectra of C 1s and S 2p regions for both the analysed films (Fig. 3.9 (b) and (c)).

Although minor oxidation effects caused by DTBP cannot be completely ruled

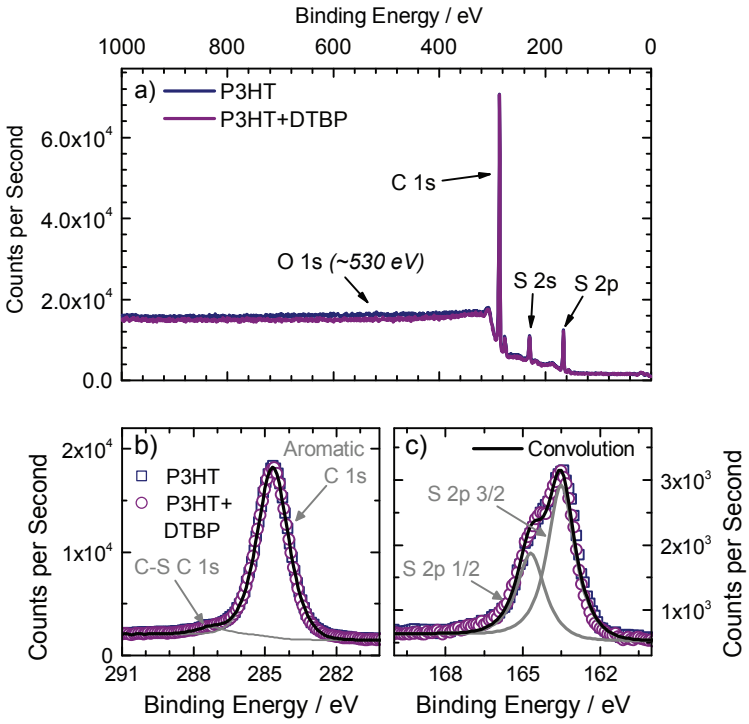

Figure 3.9.: Wide scan XPS spectra of films spin-cast from solutions with and without DTBP. High resolution scans of the C 1s and S 2p peaks are shown in (b) and (c), respectively. The gray lines show the individual components of the peaks. The overall convolution is shown as black line.

out even if the solution is kept at room temperature, the results obtained so far all indicate that the process behind the formation of insoluble layers is a self-assembly process driven by the limited solubility of P3HT in DTBP. Non-polar solvents such as chlorobenzene are well suited for P3HT, which is a non-polar molecule as well. In contrast, DTBP shows a distinct polarity due to the strong electronegativity of the two central oxygen atoms.

As will be shown in Chapter 5, no effect that can be traced back to an oxidation is apparent from the transistor characteristics and photovoltaic device performance either.

3.3.5. Additional Characterisation Techniques

This section reports on two experiments which were performed within the framework of this thesis, but which are not fully conclusive yet. However, since the measurements complement the experiments presented in this chapter and since the findings could be the basis for future experiments, the preliminary results of these measurements are included in this thesis.

Both experiments were carried out during secondments within the *Initial Training Network* (ITN) *"SUPERIOR"*. The aim of the work that is reported in the first subsection was the alignment of P3HT NFs using a strong magnetic field (up to 32 T). The measurements were carried out during a visit to the High Field Magnet Laboratory (HFML) at Radboud University Nijmegen (The Netherlands).

The second subsection describes an experiment that was focused on imaging P3HT NFs using a scanning near-field optical microscope (SNOM). The work was carried out during a visit to APE Research (Trieste, Italy), a company that is specialised in the development and application of various scanning probe microscopy techniques.

Alignment of P3HT NFs in a High Magnetic Field

The ability to fabricate films of aligned NFs enables the investigation of directional charge transport (parallel or perpendicular to the fibre long axis) as well as the polarisation dependence of optical absorption and photoluminescence. The idea is to deposit pre-formed NFs from solution while a high magnetic field is applied during the drying process to achieve the desired orientation on the substrate. Aligned films using a magnetic field during drying have been reported for liquid crystalline semiconductors and self-assembled anthracene fibres, but little work has been reported on the alignment of P3HT NFs. [100–102] Yonemura *et al.* reported a partial alignment of P3HT NFs using fields with a field strength up to $B = 10\,\mathrm{T}$. [103]

To confirm the expected alignment of P3HT NFs in solution, a dilute NF solution ($\approx 10^{-2}$ mg/ml P3HT in chlorobenzene or toluene) was placed in a 32 T magnet, and possible alignment was detected using a birefringence setup. The retardation of a 632 nm laser beam that passes through the sample in dependence of the applied magnetic field strength is shown in Figure 3.10. The blue curve shows the measurement on centrifuged NFs dispersed in toluene. It features a sharp onset of alignment at

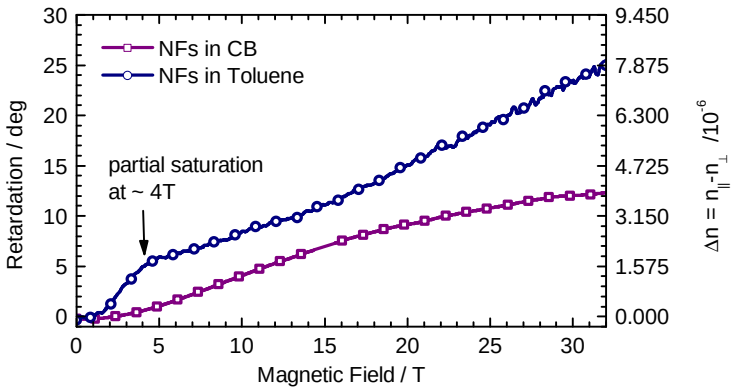

Figure 3.10.: Retardation of a 632 nm laser beam when passing through samples of NFs in solution in dependence of the applied magnetic field strength B. The retardation is caused by a difference in refractive index for the ordinary and extraordinary beam (calculated values on right y-axis), indicating field-induced alignment effects. Both curves were corrected for solvent effects by subtracting the signal of a sample of pure solvent.

a field strength of $B \approx 1.5\,\mathrm{T}$ and the beginning of a saturation regime at $B \approx 4\,\mathrm{T}$. However, the curve is still increasing significantly at $B \geq 4\,\mathrm{T}$, instead of showing a flat plateau which would be expected when the alignment of the fibres is completed. A continuous increase of alignment with increasing B can result from a large size distribution of the fibres. Large fibres will, due to the increased magnetic dipole moment align at lower field strength then fibres of smaller size. Although the solution has been centrifuged to remove non-aggregated polymer chains, a wide distribution of fibre length is still expected as suggested by the AFM images discussed above (Fig. 3.3). It is also supported by the data obtained for the same measurement on fibres dispersed in chlorobenzene (purple curve in Fig. 3.10). In this case, a clear onset of beginning alignment is missing, instead the retardation signal continues to increase with increasing field strength. Since chlorobenzene is a good solvent for P3HT, it is expected that the fibres get partially redissolved, resulting in a larger fraction of smaller aggregates and dissolved polymer chains (compare also Fig. 3.2 and discussion).

The large size distribution of the NFs in solution, which can hardly be overcome with the fibre fabrication techniques used in this work, constitutes a limitation for the

complete alignment of the fibres. Another limitation is the vertical geometry of the high field magnet at HFML. The fibres are expected to align in a plane perpendicular to the field direction. This means that material which is deposited on a horizontally flat substrate does not experience an in-plane alignment.

The maximum field strength that was available in a horizontal geometry at HFML was a 2 T magnet. According to the data in Figure 3.10, this field strength is expected to result in a partial alignment of the longer fibre fraction. Unfortunately, no alignment effect could be detected on films dried from chlorobenzene or toluene, using polarised absorption measurements and AFM. It is most likely that convection during drying of the solvent counteracts the relatively weak forces of the magnetic alignment.

Scanning Near-Field Optical Microscopy

A scanning near-field optical microscope (SNOM) is a type of scanning probe microsope that uses an optical fibre with an aperture of a few tens of nanometres. [104] Because of the small fibre opening, light that passes through the fibre is not able to exit through the aperture. However, the electromagnetic field will protrude from the fibre opening for a few tens of nanometres, allowing optical excitation of the sample with high resolution (exceeding the resolution of a conventional optical microscope). Light emitted through fluorescence of the sample as well as scattered light from the excitation is collected by a photodetector with optional filters focused on the scanned area of interest. At the same time, an image of the samples topography is recorded by scanning the probe across the sample, using shear forces to regulate the height of the probe aperture over the sample. Figure 3.11 (a) shows the topography of a sample of P3HT fibres on a fused silica substrate recorded with a SNOM. The top part of this image shows individual fibres with dimensions as expected from the AFM measurements described above (compare Fig. 3.3 (a)). The ability to image small height differences of the substrate, in this case the grooves from the fused silica substrate leading diagonally through the image, demonstrates the high resolution of this technique for horizontal displacement as well as the height resolution.

In the lower part, however, bigger structures, extending vertically (i.e. perpendicular to the scanning direction) are visible. These structures are artefacts that most likely result from material being adhered to the probe and displaced during the scan.

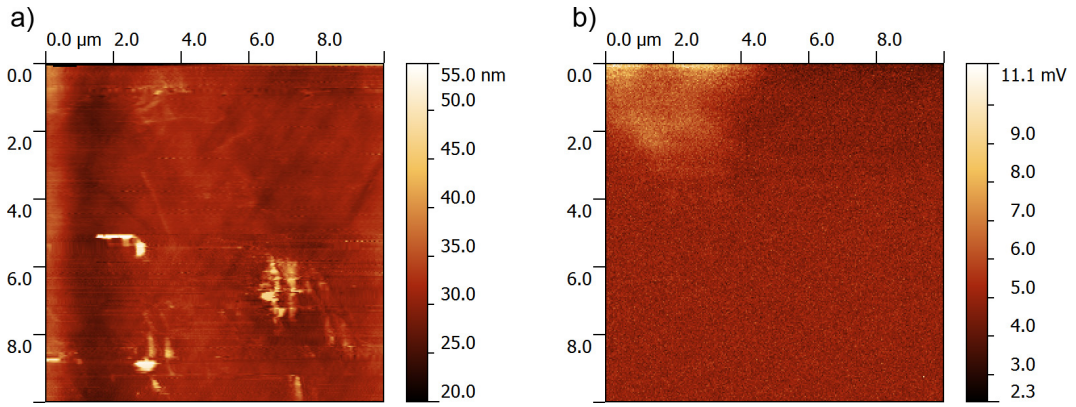

Figure 3.11.: (a) SNOM-Topography image of a sample of DTBP-grown NFs on a fused silica substrate. (b) Fluorescence image of a sample of DTBP-grown fibres on a SiO_2 substrate, using a 532 nm laser as excitation through the SNOM fibre and light detection in reflection mode.

This problem arises from the small dimensions and soft nature of the polymer fibre and the use of shear forces to detect the distance between probe and sample.

To avoid the issue of material being displaced by the scanning probe during a fluorescence scan, the instrument was operated in constant height mode ($< 1\,\mu$m above substrate surface) for collection of emitted light. A 532 nm diode laser was coupled into the optical fibre as the excitation source. This wavelength is close to the absorption maximum of the NFs ($\lambda \approx 550$ nm, compare Fig. 3.5), and therefore is expected to provide a nearly optimal PL intensity. A high pass filter (cutoff wavelength ≈ 550 nm) in front of the photodetector was used to avoid detection of scattered excitation light and to ensure the detected signal results from the fluorescence of the NFs. Figure 3.11 (b) shows an image of a sample of DTBP-grown NFs spin-cast on a silicon substrate. While the whole image is relatively featureless, a clear signal could be detected in the top left corner of the image. The dimensions, several micrometres in size, suggest that it is one of the larger fibre bundles, as described in Figure 3.3, that show up in the fluorescence image. Towards the edges of the bundle, the fluorescence signal becomes weak. Although separated fibres are expected to be present near the edges, their fluorescence cannot be detected. One of the main challenges for the detection of smaller features is the low PL efficiency of the P3HT fibres of about 2-4 %. An advanced setup for light-collection would be necessary to detect the weak

fluorescence of individual fibres.

3.4. Conclusion

This chapter described the controlled formation of P3HT nanofibres using DTBP as an additive to a solution of P3HT in chlorobenzene. Absorption spectroscopy confirms that the NFs are formed in solution, where they are present along with a fraction of dissolved polymer chains. Spin-cast from a dilute solution, the fibres can be separated and deposited on a substrate. AFM images reveal the dimensions of the NFs, which are of varying length up to several micrometres. The width of the fibres is similar for all imaged NFs, about 50 nm, while the height can vary between < 2 nm up to ≈ 8 nm, and it could be shown how the height corresponds to multiples of ≈ 1.6 nm, the lamella stacking distance between individual polymer chains. Using the model of weakly coupled H-aggregates to describe the shape of the absorption spectra of the spin-cast films, it was shown how the average crystallinity of the film can be controlled by the concentration of DTBP that is added to the solution. Alongside the crystallinity, it is also shown how surface roughness and, most importantly, the film retention increases with increased DTBP concentration. The increased crystallinity and film retention will be further investigated in Chapter 5, where these NF films will be employed in organic thin-film transistors and photovoltaic cells.

With a view to such applications it is important to note that optical absorption and XPS spectroscopy on the fibre films show that the use of DTBP does not result in measurable oxidation effects if kept at room temperature. Although minor oxidation effects and a partial cross-linking cannot be completely ruled out, the main underlying process for the fibre formation appears to be a self-assembly process driven by the change in solvent polarity with the addition of DTBP.

It could be demonstrated how NFs in solution can be aligned in a magnetic field of a strength of 2-4 T. It is challenging, however, to transfer the aligned NFs on a substrate, since solvent drying effects easily counteract the weak alignment forces.

Scanning near-field optical microscopy (SNOM) could be employed to image the topography of separated NFs, although the fact that this technique uses shear forces between the probe and the sample bears the risk that the NFs get displaced or damaged. The fluorescence of larger fibre bundles upon excitation through the SNOM

probe could be successfully detected. However, the low PL quantum efficiency of the P3HT NFs of 2-4 % in combination with its small dimensions makes it challenging to detect the emitted light from single NFs.

4. Temperature-dependent Photoluminescence of Polythiophene Nanofibres

4.1. Introduction: Photoluminescence of P3HT Aggregates

This chapter will investigate the steady state photoluminescence (PL) of a range of P3HT nanofibre (NF) samples in dependence of temperature. As will be shown in the following sections, the behaviour of the fibre samples shows clear deviations from the PL characteristics of P3HT thin-films. To understand better the differences, this section will give an overview of the current knowledge regarding the description of the PL lineshape of P3HT.

Compared to the large research effort that has been put into the understanding and optimisation of P3HT as a donor material in organic solar cells as well as charge transport properties in thin-film transistors, much less work has been done on the basic understanding of the photophysics of it. However, a good description of steady state absorption and emission behaviour could be developed, mainly driven by the theoretical work of *F. Spano*, *H. Yamagata* and coworkers, [40–42, 105–108] as well as experimental results from *C. Silva* and *J. Clark*. [44, 45, 109]

As introduced in Section 2.3, the optical response of polymer aggregates can in general be described by considering coulombic interactions of transition dipoles that can couple in either a side-by-side orientation, as is the case for H-aggregates, or aligned along one dimension, called J-aggregates (compare Fig. 2.6). For thin-films of P3HT, it has been found that both optical absorption as well as the photoluminescence spectra can be well explained by weakly coupled H-aggregates. [44] This is due to dense π-stacking of the polymer chains with short distances between the

interacting chromophores of $\approx 3.8\,\text{Å}$, giving rise to excitonic coupling across the polymer chains. Dipole coupling along the polymer backbone is probably disrupted by torsional disorder because of the interacting hexyl side chains, which suppresses J-aggregate behaviour. The strength of the coupling and hence the size of the exciton bandwith W was found to be dependent on the nanomorphology of the P3HT film. [44, 45] This important result could be successfully applied in the previous chapter to determine the average crystallinity of nanofibre films (see Sec. 3.3.3).

However, recent studies have shown significant deviations from this model. In particular, investigations on isolated NFs of P3HT showed altered absorption and PL characteristics compared to that of a P3HT film. [25, 93, 110–112] Furthermore, a clear difference in the photophysics of P3HT films is seen in dependence of the molecular weight, with high molecular weight P3HT showing a behaviour that cannot be fully described by the model of weakly coupled H-aggregates [109]. Instead, it appears to be the case that the optical response of P3HT aggregates requires a more general description where both *inter*chain and *intra*chain coupling is taken into account. [106, 108, 109]

The following sections give an overview of the different PL characteristics of H- and J-aggregates and how this model can be applied to P3HT, continuing the explanations in Section 2.3. Besides describing ideal aggregates, this also includes the effect of disorder and temperature. With regard to more recent findings, Section 4.1.3 gives an introduction to the concept of the HJ-aggregate model.

4.1.1. Photoluminescence in H- and J-Aggregates

According to Kasha's rule, vibrational relaxation to the lowest excited state takes place on a much shorter time scale than the lifetime of an exciton, photon emission will therefore have to take place from the lowest energy excited state. In ideal H-aggregates consisting of rigid molecules, the optical transition from the band bottom of the lowest excited state is optically forbidden, hence these aggregates do not show any fluorescence.

For the more relevant case of aggregates made of non-rigid molecules, it is just the 0-0 transition that is forbidden. Transitions to higher-lying vibronic levels are allowed to take place as illustrated in Figure 2.7.

The radiative decay rate for H-aggregates is decreased, due to the suppressed 0-0 transition as well as a decrease in side-band intensity with increasing bandwidth W. It is therefore the 0-1 transition that increasingly dominates the emission spectrum.

For J-aggregates, both the absorbing state ($k = 0$) and the emitting state are located at the band bottom, which leads to a negligible Stokes shift in this case. Furthermore, absorbing and emitting state red-shift with increasing W. The radiative decay rate of the 0-0 emission is enhanced by the coherence number N_{coh} which is the number of chromophores over which the wave function is spread. This enhancement by a factor which equals the number of coherently coupled chromophores leads to superradiance of J-aggregates at low temperature. In contrast to the 0-0 emission, the 0-1 side-band emission is not influenced by an increase in N_{coh} (in either H- or J-aggregates). The emission intensity ratio of the 0-0 to 0-1 emission can therefore be used as a direct measure of the exciton coherence length. In fact, the line intensity ratio $I_{PL}^{0-0}/I_{PL}^{0-1}$ increases linearly with N_{coh}, which is true for all aggregates with allowed 0-0 transition.

For P3HT, it has been found that the shape of the low temperature PL spectrum can in general be explained using a modified Franck-Condon model, [44]

$$I_{PL}(\omega) \propto (\hbar\omega)^3 n_f^3 e^{-\lambda^2} \times \left[\alpha\Gamma(\hbar\omega - E_0) + \sum_{m=1,2,..} \frac{\lambda^{2m}}{m!}\Gamma(\hbar\omega - (E_0 - m\hbar\omega_0)) \right], \tag{4.1}$$

which describes a vibronic progression of emission peaks with an energetic distance of $\hbar\omega_0 \approx 0.17\,\text{eV}$ and decoupled 0-0 emission peak with relative intensity α. n_f is the refractive index of the film (which, for P3HT is ≈ 2 and strictly speaking a function of ω), [99] Γ a Gaussian function that represents the inhomogeneously broadened line-shape of the vibronic replica in the progression, E_0 the energy of the origin of the progression, and λ is the Huang-Rhys parameter.

4.1.2. Static Disorder and Thermal Effects:

In H-aggregates, static disorder breaks the symmetry of the dipole coupling and therefore allows emission to the vibrationless ground state, which is strictly forbidden in perfect H-aggregates. Hence, increasing disorder increases the intensity of the 0-0 emission peak. Although sideband intensities increase as well this happens at a slower

rate, which means that $I_{PL}^{0-0}/I_{PL}^{0-1}$ increases with disorder. For the case of weakly coupled H-aggregates, Spano derived an equation that describes the dependence of the 0-0 and 0-1 emission peak ratio by

$$R_{em} = I_{PL}^{0-0}/I_{PL}^{0-1} \propto \frac{(1-\beta)\,\sigma^2}{(1+\beta)\,W^2}\ , \tag{4.2}$$

where σ is a disorder parameter, i.e. the width of the Gaussian distribution of site energies, and β a spatial correlation parameter which ranges from 0 (chain disorder is greatest) to 1 (corresponding to maximum N_{coh}). [40] It can be seen that the intensity ratio is largest for a given σ if disorder is at its maximum, i.e. if $\beta = 0$. It also includes the dependence on W, describing how a decrease in W increases the intensity ratio as discussed above.

In J-aggregates, the opposite behaviour is observed. Here, the 0-0 intensity decreases strongly (while sideband intensities decrease slightly) as N_{coh} is decreased, resulting in decreasing R_{em} with increasing disorder.

Increasing temperature leads to the thermal activation of vibronic states above the band bottom. In the case of H-aggregates, this gives rise to the population of the $k = 0$ state at the top of the band, leading to an increased intensity of the 0-0 emission. The opposite is true for J-aggregates. Here, the thermally excited states with $k \neq 0$ cannot emit to the vibrationless ground state, leading to reduced 0-0 line intensity. Importantly, the general trend of R_{em} with increasing temperature is the same for disordered aggregates and disorder free aggregates. In both cases it can be calculated that the PL ratio decreases with $1/\sqrt{T}$ as the temperature is increased. [43]

4.1.3. The HJ-Aggregate Model

In recent years, a more general model to describe the photophysics of polymer aggregates has been developed, called the HJ-aggregate model. [106] The main motivation for the development of this model was that the H-aggregate model, although successful in describing the PL behaviour of films prepared with low and medium molecular weight P3HT, especially if cast from low boiling point solvents, showed significant deviations from the measured spectra of films using P3HT with high molecular weight, or if measured on individual, self-assembled nanofibres.

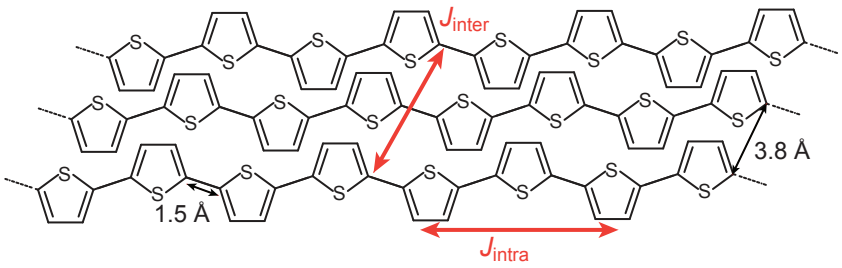

Figure 4.1.: Illustration of P3HT crystal structure (hexyl side chains are omitted for clarity), showing how dipole-dipole interactions can take place along one polymer chain (J-type), or across neighbouring polymer chains (H-type). The strength of the coupling in each direction is expressed by the coupling counstants J_{intra} and J_{inter}, respectively.

In this model, coupling along one polymer chain is considered in the form of the intrachain coupling constant J_{intra}, as well as coupling across the polymer chains in the stack, expressed by J_{inter}. The photophysical response will be determined by a competition of the coupling in these two dimensions. Dominant intrachain coupling will result in a behaviour that can be explained by the J-aggregate model, while dominant interchain coupling will show up in a H-aggregate-like characteristics.

Figure 4.1 illustrates the two types of coupling for the case of P3HT. Although the distance between thiophene rings located on different polymer chains is larger than between the rings along one chain (i.e. the π-stacking distance of 3.8 Å vs. a C-C bond length of $\approx$ 1.5 Å), coupling of neighbouring chromophores along one chain is usually suppressed by torsional disorder induced by the specific packing arrangement of the alkyl side chains.

Yamagata and *Spano* find that increasing interchain coupling leads to a splitting of the intrachain energy levels into two energy levels, depending on the orientation of the coupled intrachain dipoles (symmetric or antisymmetric). Referring to the case of the ideal dimer J-aggregate in Figure 2.6 (b), this means that the lowest energy state E_{J-P} will be split into a state E^{+}_{J-P} at higher energy, and E^{-}_{J-P} at lower energy. The energetic distance, ΔE depends on the strength if the interchain coupling. As is the case for H-aggregates, emission to the vibrationless ground state is only allowed for the symmetric state. This leads to the fact, that the 0-0 emission in J-aggregates

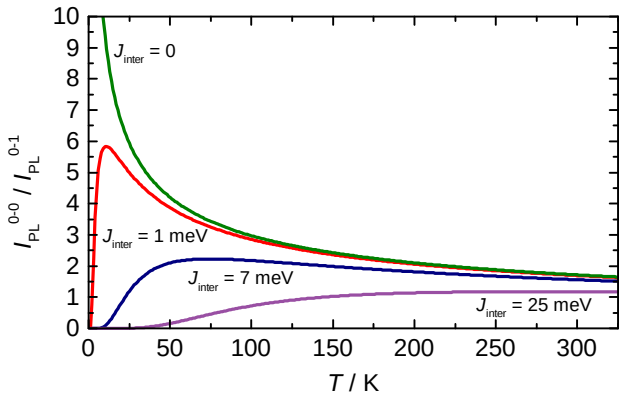

Figure 4.2.: Temperature dependence of the 0-0 to 0-1 intensity ratio as described by the HJ-aggregate model in reference [106]. To demonstrate the strong influence of the strength of intermolecular coupling, curves are plotted for different values of J_{inter} using Equ. 4.3 with $J_{intra} = 40\,\text{meV}$.

with non-vanishing interchain interactions needs to be thermally activated.

At low temperatures, the photophysical behaviour will look similar to what is predicted for an H-aggregate, i.e. a vanishing 0-0 intensity that slowly increases with T. As soon as the temperature is high enough so that $k_bT \approx \Delta E$, the symmetric state E^+_{J-P} gets populated and the emission changes to a J-like characteristic, where R_{em} decreases with increasing T. The analytical expression for the PL intensity ratio in dependence of J_{inter} and J_{intra} derived by *Yamagata* and *Spano* is

$$R_{em} = I_{PL}^{0-0}/I_{PL}^{0-1} = \frac{1}{\lambda_0^2}\frac{2e^{-2FJ_{inter}/k_bT}}{1+e^{-2FJ_{inter}/k_bT}}\sqrt{\frac{4\pi F\,|J_{intra}|}{k_bT}}\,, \tag{4.3}$$

where F is the Franck-Condon factor. [43, 106] To get an idea of what the behaviour looks like for P3HT, Equation 4.3 can be plotted using the P3HT-optimised single-chain parameters, $F = 0.34$, $\lambda_0^2 = 1.5$, $J_{intra} = 40\,\text{meV}$. [106] The curves are shown in Figure 4.2 for a range of values for J_{inter}. The case of $J_{inter} = 0$ describes a pure J-aggregate, where the PL spectrum at low temperature is dominated by the 0-0 transition, which decreases with temperature as $1/\sqrt{T}$. For non-zero interchain coupling, the PL ratio then increases first and reaches its maximum at $T > 0\,\text{K}$, before it decreases similar to J-aggregates. The temperature T_P at which R_{em} reaches its maximum calculated from the above expression is

$$T_P \approx 2.6FJ_{inter}/k_b\,. \tag{4.4}$$

For values of J_{inter} that are typical for P3HT films, the behaviour is similar to what is predicted from the pure H-aggregate model. For $J_{inter} = 25\,\text{meV}$ (corresponding to $W = 4\,|J_{inter}| = 100\,\text{meV}$, which is the value that was found for untreated films in Chapter 3, compare Tab. 3.1.), the PL ratio is expected to increase steadily with increasing temperature.

The following sections explore how measured PL spectra of P3HT NFs differ from that of P3HT thin-films and how the above model helps to explain the differences by relating the PL characteristics of the samples to changes in the strength of inter- and intrachain coupling, caused by the different processing techniques.

4.2. Experimental

4.2.1. Materials and Sample Preparation

For the presented measurement in this chapter, the same batch of P3HT (M_n = 54,000-75,000 g/mol) that was described in the previous chapter (compare Sec. 3.2) was used. All solvents were purchased from Sigma-Aldrich and used without further purification.

Three different samples are compared in this study, a P3HT thin-film sample, and two nanofibre samples, one prepared from *p*-xylene solution, and one from toluene solution.

Thin-film Sample

For the thin-film sample, a solution of 10 mg/ml P3HT in chloroform was prepared and heated to a temperature of 50 °C to make sure the material is well dissolved. It was then spin-cast at 2000 rpm on a circular fused silica substrate (diameter 15 mm) while still warm.

Nanofibre Samples

The xylene NF sample was prepared by dissolving 0.1 mg/ml P3HT in *p*-xylene and heating the solution by placing it on a hot plate at 100 °C until a bright orange colour could be observed. It was then taken off the hotplate and cooled down to room temperature relatively quickly (< 30 min).

The toluene NF sample was prepared by dissolving 0.1 mg/ml P3HT in toluene, and heating the solution to 100 °C in a water bath until a bright orange colour could be observed. The water bath was then gradually cooled down to room temperature over a period of ≈ 2 h.

Both solutions changed colour to dark purple during cool-down. They were left at room temperature for ≈ 1 day, before the nanofibre fraction was separated from non-aggregated material by two centrifugation steps. Fresh solvent was added after the supernatant, i.e. solvent with remaining non-sedimented material was removed to keep the overall concentration of solid content approximately constant.

Both samples were prepared by drop-casting the centrifuged solution on fused silica substrates.

4.2.2. Measurement Setup

The temperature-dependent photoluminescence spectra were recorded using a closed cycle optical cryostat (Optistat AC-V from *Oxford Instruments*) and a 532 nm collimated diode laser ($P = 4.5$ mW) as excitation light source. The experimental setup is illustrated in Figure 4.3 (a). The sample is placed in the vacuum chamber of the cryostat ($p \approx 10^{-5}$ mbar) with four entrance windows. The sample holder is connected to the cold head, which is cooled by a closed cycle system which is connected to an air cooled compressor system (*Cryomech PT403*). Thermal contact of the sample with the sample holder is secured by tightly pressing the sample against the sample holder using a metal frame and four screws.

The excitation enters the vacuum chamber through one of the optical windows and the laser spot of diameter of ≈ 3 mm covers part of the sample. The emitted light is detected using a combination of an imaging spectrograph (*Andor Shamrock SR163i*) and a low-noise CCD detector (*Andor Newton*^{EM}). To avoid self-absorption effects, the spectrometer is placed to detect light from front illumination. The angle of the excitation beam is adjusted so that the reflected beam does not enter the spectrometer.

The cryostat used is able to cool down to a measured temperature (of the sample holder) of ≈ 7 K. The cool-down procedure takes about 120 min. The temperature curve during cool-down is shown in Figure 4.3 (b). The sample holder can be heated

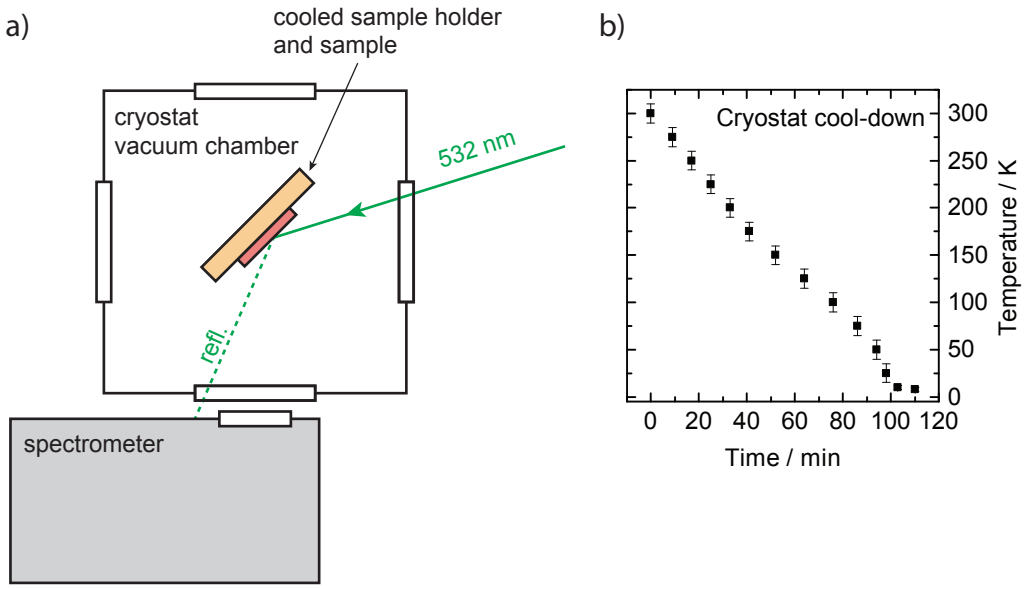

Figure 4.3.: (a) Illustration of the experimental setup for temperature-dependend PL measurements. (b) Sample temperature vs. time during cool-down from room temperature.

at the same time as it is cooled, which allows a fine adjustment and stabilisation of the temperature over a wide range.

The temperature-dependent spectra reported in this chapter were recorded during warm-up of the sample, after it had been cooled down to the lowest temperature possible. For temperature steps up to 100 K both the cooling system and the heater were operated. For measurements at higher temperature, the cooling system was switched off, and the temperature increased slowly by using the electrical heater and temperature control. However, a comparison between spectra recorded during cool-down of the cryostat and slow warm-up showed little deviation, indicating a good thermal contact between the cryostat and the sample (spectra can be found in the Appendix).

4.3. Results

4.3.1. Comparison of P3HT Thin-Film and NFs

To study the different behaviour of the temperature dependence of film and nanofibres in more detail, three different samples are compared in this study. For more details about the preparation of the samples, see Section 4.2.1.

The first sample is a film of P3HT, spin-cast from chloroform, which acts as a reference and is expected to show the behaviour that can be described by weakly coupled H-aggregates, as discussed above. In the following, this sample is referred to as *"thin-film"*.

Two different processing methods were chosen for the NF samples. One sample was prepared by cooling a warm solution of P3HT in *p*-xylene, while a second sample was prepared by using toluene as a solvent and a slow cooling method using a water bath. It was shown by *J. Roehling et al.* that using *p*-xylene as a solvent and a rapid formation process results in a different nanomorphology of the fibres with less perfect aggregates than if the NFs are grown by slowly cooling a solution in toluene. [93] A third formation process, the fabrication of NFs by addition of DTBP to a chlorobenzene solution that was described in Chapter 3, has also been investigated within this study. The preparation method of using an additive results in a rapid NF formation process, hence the morphology of these fibres is expected to be similar to the NFs grown in xylene solution. To support this assumption, the PL spectra of the DTBP sample can be found in the appendix of this thesis. It demonstrates that the temperature behaviour is indeed similar to the xylene sample presented in this chapter. To avoid unnecessary duplication of the results and for the sake of simplicity of the argumentation, the data for the DTBP samples will not be presented in the framework of the following section. Also, the use of methods using cooling in *p*-xylene and toluene allows better comparability of the results, since these methods have been employed by other groups as well.

It is important to note that all samples were prepared from the same material batch of P3HT, to eliminate the influence of variations in molecular weight and to solely focus on the different processing conditions.

As a first characterisation of the samples and to assess the different degree of intermolecular order, the absorption at room temperature is studied.

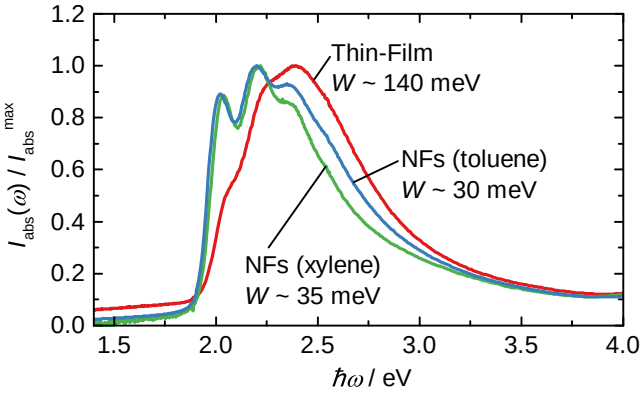

Figure 4.4.: Absorption spectra (measured at RT) of the P3HT thin-film and the two NF samples. The values for W are calculated from the ratio of the two lowest energy absorption peaks using Equation 3.4.

4.3.2. UV-vis Absorption

Figure 4.4 shows the absorption spectra of the three samples investigated in this study. It can be seen that the spectral lineshape of the film sample differs from that of the two NF samples. In particular, the 0-0 transition at $\sim 2.0\,\text{eV}$ is much stronger for the nanofibers than it is for the film. Note that according to Equation 3.4, the ratio between the peak at $\sim 2.0\,\text{eV}$, the absorption strength of the 0-0 transition I_{PL}^{0-0}, and the peak at $\sim 2.2\,\text{eV}$, I_{PL}^{0-1}, is related to the exciton bandwidth W, where an increasing absorption peak ratio indicates a decreasing exciton bandwidth. From the graphs in Figure 4.4, a value for W of 140 meV can be calculated for the film sample. This relatively large value indicates a high degree of disorder, which is also confirmed by the fact that the maximum of the absorption for this sample lies at a higher energy of $\sim 2.4\,\text{eV}$, a region where mainly uncoupled chromophores absorb. For the fiber samples, a much smaller value for W is derived from the absorption spectra, 35 meV and 30 meV for the fast and slow-cooled fibers, respectively. These values confirm the assumption that the slowly-grown toluene NFs show the highest degree of molecular order, while the thin-film is significantly less ordered than both fibre samples.

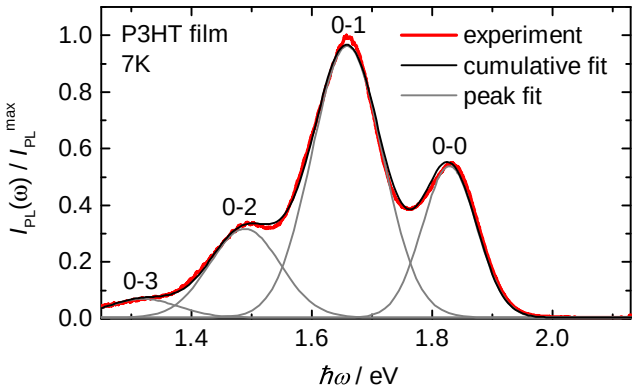

Figure 4.5.: Low temperature (7K) PL spectrum of a film of P3HT. The peak fits are Gaussian functions with an energy difference of $\hbar\omega_0 = 170\,\text{meV}$.

4.3.3. Low Temperature PL

To provide a reference for the following investigation into the PL characteristics of P3HT NFs, the PL spectrum of a film of P3HT, spin-cast from chloroform was measured. As mentioned in the introduction above, the photophysics of such films can be well described using the H-aggregate model.

Figure 4.5 shows a measured PL spectrum of a film of P3HT, together with Gaussian peak fits with a distance of $\hbar\omega_0 = 170\,\text{meV}$. The spectrum shows the expected lineshape for weakly coupled H-aggregates and can be well described by a series of Gaussian peaks as expressed in Equation 4.1.[1] The relative line intensity of the 0-0 transition can be determined to be $\alpha \approx 0.45$, which indicates a significant degree of disorder in the π-stack, in line with a relatively large $W \approx 140\,\text{meV}$ as determined from the UV-vis absorption above. Further contributions to a non-vanishing 0-0 intensity according to Equation 4.2 is a large distribution of site energies as well as little spacial correlation, which might both be related to a largely disordered film morphology. Due to the interdependence of the individual parameters, it is difficult to determine the main contributing factor.

A different behaviour is revealed when looking at the NF samples. Figure 4.6 shows the measured PL spectra for a sample of NFs grown from toluene solution.

[1] For the 0-0 transition, the constraint of equal linewidth for all peaks had to be relaxed in order to make the fit converge, which resulted in a narrower linewidth for the 0-0 transition than for the three peaks at lower energy.

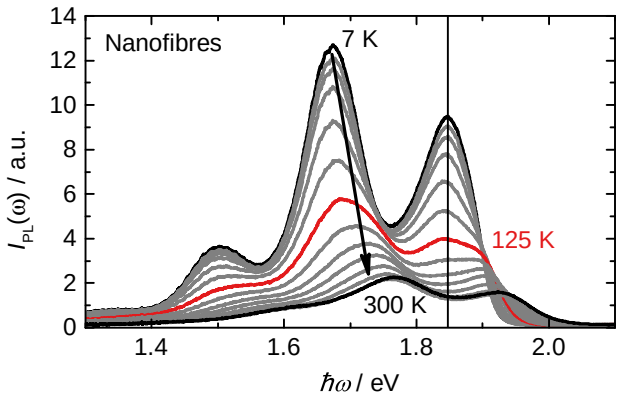

Figure 4.6.: Temperature dependent PL spectra of toluene NFs under constant excitation intensity. The vertical line marks the position of the low temperature 0-0 transition at $\hbar\omega \approx 1.84\,\mathrm{eV}$.

The spectra are measured at varying temperature between 7 K and 300 K. At low temperatures, the spectrum looks similar to the one shown for the film (for a direct comparison see further below, Fig. 4.9 (a)), but the shape of the spectrum changes significantly with increasing temperature. Highlighted in Figure 4.6 is the spectrum that was measured at a temperature of 125 K, which clearly shows a lineshape that cannot be described by a single vibronic progression. With increasing temperature, the intensity of the low temperature progression decreases, and a gradual shift to a second progression at higher energy takes place. Interestingly, the position of the low temperature 0-0 peak (at $\hbar\omega \approx 1.84\,\mathrm{eV}$) seems to remain at the same position, while the second progression peaks shift to higher energy.

The following section will directly compare the spectra of thin-film and NFs at different temperature.

4.3.4. PL Temperature Evolution for Thin-Film and NFs

Figure 4.7 shows the PL spectra measured for the three samples with increasing temperature, starting from $\sim 7\,\mathrm{K}$ up to 300 K.

Remarkably, there is a significant difference in the PL characteristics of the three samples, which highlights the importance of processing conditions on the optical properties of organic semiconductors. The spectra in Figure 4.7 (a) show an expected behaviour that was previously reported for P3HT films. [44] With increasing

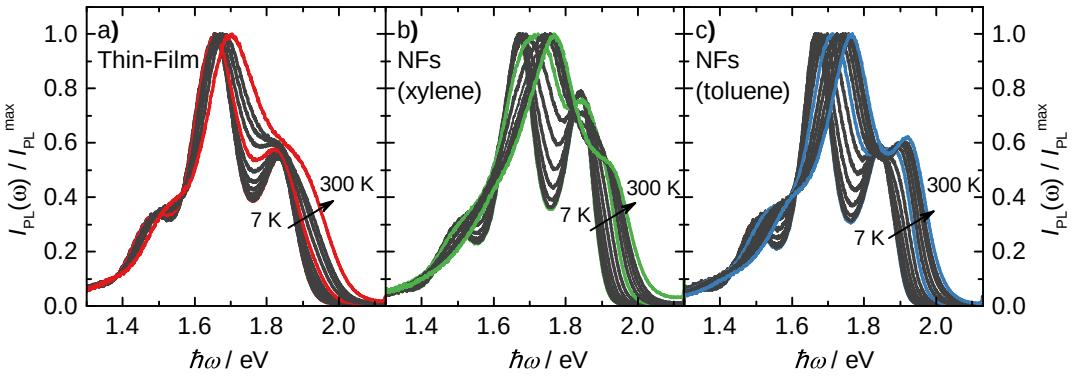

Figure 4.7.: Temperature evolution of the photoluminescence of the investigated samples. The spectra in colour are the spectra at 7 K, 175K and 300 K which are shown in direct comparison in Figure 4.9.

temperature, it shows inhomogeneous line-broadening due to increasing disorder, a slight blue-shift of the spectrum due to decreased conjugation length, and a small increase of the intensity ratio of 0-0 to 0-1 transition. These characteristics indicate a predominantly H-like interchain coupling.

A different behaviour is observed for the NF samples. Also in this case, the spectra shift to higher energy with increasing temperature, but in contrast to the film sample, the 0-0/0-1 does not increase continuously. Instead, the low temperature 0-0 transition loses intensity, while a higher energy peak develops with increasing temperature. This is more pronounced for the xylene NF sample, but the trend for the toluene NFs is the same, as might be clearer from the non-normalised spectra in Figure 4.6.

It is interesting to look closer at the extent of the blue-shift with increasing temperature, and at the evolution of the 0-0 line intensity, which is initially, i.e. at low temperature, at around 1.84 eV.

Figure 4.8 (a) shows the position of the intensity maximum, which for all samples is the energy of the the 0-1 transition, E^{0-1}, in dependence of temperature, illustrating the shift of the whole spectrum. It can be seen that both NF samples show a strong blue-shift of around 100 meV when the temperature is raised from 7 K to 300 K. The shift for the thin-film sample is, with around 45 meV, much smaller. Also, the shift does not take place continuously. Instead, for the NFs, starting from around 125 K, a fast shift takes place up to $\sim$ 200 K, which is somewhat slowed down after this. For

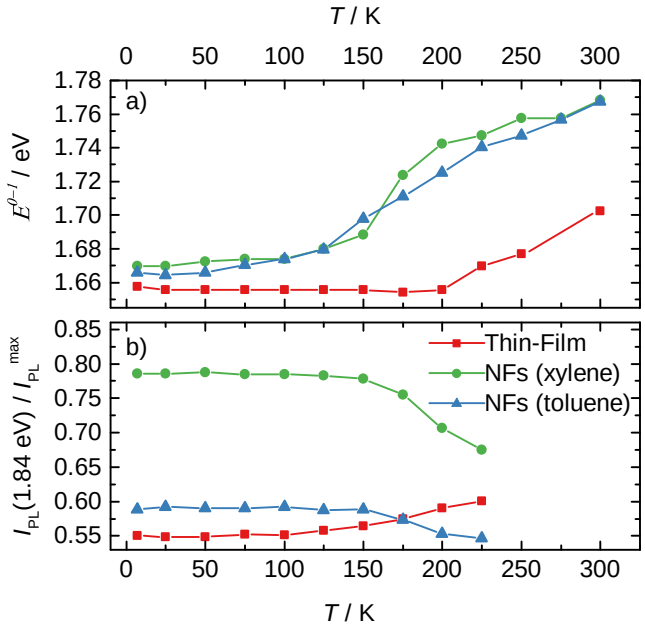

Figure 4.8.: (a) Energetic position E^{0-1} of the PL maximum of the samples under investigation and (b) the relative PL intensity at an energy of $\sim 1.84\,\mathrm{eV}$, the position of the 0-0 peak at 7 K.

the film, almost no shift takes place up to 200 K, after which a continuous increase of E^{0-1} takes place up to 300 K.

An even more dramatic difference between thin-film and NFs can be seen in the change of intensity of the transition at an energy of $\sim 1.84\,\mathrm{eV}$. This is the energy of the 0-0 peak at low temperature for all three samples. Figure 4.8 (b) shows the relative intensity for a temperature from $\sim 7\,\mathrm{K}$ to $\sim 225\,\mathrm{K}$. For higher temperature, this value starts to increase for all samples, which is due to line-broadening and blue-shift of the 0-1 transition, and is therefore not plotted in the graph.

The intensity of the 0-0 transition is highest for the xylene NF sample, but the evolution with increasing temperature is similar for both NF samples. In both cases, the 0-0 intensity stays roughly at the same value until T reaches about 150 K, from where it drops sharply. The trend is different for the film sample. Here, starting from around 100 K, the 0-0 intensity increases slightly.

Both graphs show how changes in the PL spectral shape, particularly for the fibre samples, seem to happen in a discontinuous way, with a sudden transition taking

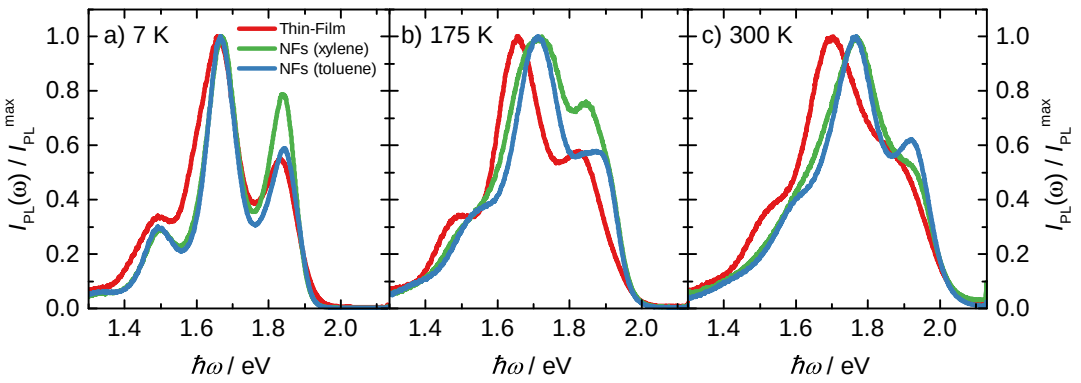

Figure 4.9.: Direct comparison of the PL spectra of the samples at different temperature.

place at a particular temperature. The transition seems to take place between a temperature of 125 K and 225 K. To have a closer look at the line shapes at this particular temperature, the spectra of all three samples at 175 K are shown in Figure 4.9, together with the spectra at lowest (7 K) and highest (300 K) temperature recorded in this series.

In terms of position of the peaks, the spectra at 7 K are almost identical. The linewidth of the film sample is slightly increased, indicating a higher degree of disorder. Also, the decreased 0-0 line intensity compared to the fibre samples can be explained by a larger W, according to Equation 4.2, which is also consistent with what was concluded from the absorption spectra in Figure 4.4. A larger W indicates a higher interchain coupling J_{inter}. Since I_{PL}^{0-0} is highest for the xylene NFs at low temperature this possibly indicates lowest J_{inter} for this sample. Decreased static disorder, which can be assumed to be case for both fibre samples, rather decreases the relative 0-0 intensity. This might contribute to the fact that the toluene NFs show a lower 0-0/0-1 intensity ratio.

More pronounced differences between the three samples can be seen when comparing the spectra at 175 K. The spectra of both NF samples have shifted significantly to higher energy. Also, it appears that these two spectra consist of more than one vibronic progression. The 0-0 peak of the toluene NF sample (blue line) feature a plateau-like shape, which seems to stem from a superposition of two emission peaks (see also Fig. 4.6). Also the xylene NF sample shows this superposition of two peaks,

which shows up as a shoulder at high energy. This shoulder perfectly matches the line shape of the toluene NFs. In contrast, the film sample shows an increased linewidth, but does not show a clear blue-shift of the spectrum.

At 300 K, the spectra of the fibre samples are significantly blue-shifted compared to those of the film sample. The toluene sample shows a higher $0-0/0-1$ ratio compared to the fast grown (xylene) sample. In both cases, the emission seems to stem from just one vibronic progression, hence the transition that was apparent in the 175 K spectra appears to be completed.

4.3.5. Integrated PL Intensity

In addition to the evolution of the intensity peak ratios, that are best compared using normalised spectra, valuable information can also be gained from the temperature dependence of the overall, i.e. spectrally integrated PL intensity. The non-normalised NF spectra for the toluene PL sample were already presented in Figure 4.6 above. Although the measurement setup used does not allow the determination of the PL efficiency Φ_{PL}, it is assumed that the angle dependence of the light emission does not change with temperature and hence the PL signal is proportional to Φ_{PL}. In general, Φ_{PL} describes the probability of a radiative deactivation, a process that takes place in competition to non-radiative deactivation (compare Eq. 2.9). It can therefore be written as

$$\Phi_{PL} = \frac{k_r}{k_r + \sum_i k_{nr}^i} \,, \tag{4.5}$$

where k_r is the radiative rate and $\sum_i k_{nr}^i$ is the sum of all non-radiative decay channels. A decrease in Φ_{PL} can be caused by either a decreased k_r or increased non-radiative rate. As discussed in Section 4.1.3, a temperature dependent change in the radiative rate mainly affects the 0-0 transition, with a sharp decrease of I_{PL}^{0-0} with increasing temperature if J-like intrachain coupling dominates, and in contrast an increase of I_{PL}^{0-0} for dominant interchain coupling. However, from Figure 4.6 and Figure 4.7 it can be seen that the overall intensity decreases significantly for the whole spectrum starting from a low temperature (< 100 K), while the intensity ratio R_{em} is not affected.

It is therefore more likely that an increase in non-radiative rate is responsible for the demise of the PL intensity. To look at this in more detail, the total PL intensity

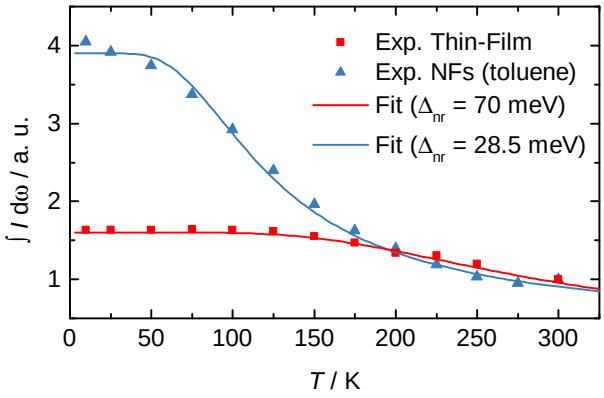

Figure 4.10.: Integrated PL intensity of a thin-film sample and a toluene NF sample vs. temperature. The continuous lines are best fits of the data using Equation 4.9.

of the NF spectra in Figure 4.6 was calculated by integrating the area under the curve from $\hbar\omega = 1.3\,\mathrm{eV}$ to $\hbar\omega = 2.1\,\mathrm{eV}$. This data is shown in Figure 4.10, together with the same data for the set of PL spectra for the thin-film sample that was discussed above (Fig. 4.7 (a)). The datasets were normalised to the intensity at 300 K to allow a better comparison.

At a first glance, the two curves seem to show a different behaviour. The film shows a long plateau with little change when the temperature is increased, and starting from $T \approx 150\,\mathrm{K}$ decreases slightly. The total intensity at lowest temperature is increased by a factor of about 1.6 compared to the intensity at 300 K.

For the NFs, Φ_{PL} starts to decreases at a much lower temperature than the film and the drop is much stronger, with a difference in intensity of a factor of about 4.

However, both curves can be explained by assuming a single, thermally activated non-radiative channel. With one non-radiative process, Equation 4.5 reduces to

$$\Phi_{PL} = \frac{k_r}{k_r + k_{nr}} \,. \tag{4.6}$$

A thermally activated process can be described in general by *Arrhenius'* equation, which has the form

$$k = Ae^{-\Delta/k_b T} \,, \tag{4.7}$$

where Δ is the activation energy and A a prefactor. [113] With this, Eqn. (4.6) can

be written as

$$\Phi_{PL} = \frac{k_r}{k_r + Ae^{-\Delta_{nr}/k_bT}} , \tag{4.8}$$

or, assuming that k_r is an unknown, but temperature-independent constant,

$$\Phi_{PL} \propto \frac{1}{1 + A'e^{-\Delta_{nr}/k_bT}} . \tag{4.9}$$

This expression was used to fit the data in Figure 4.10. As the curves show, both data sets can be described well with the same equation with a different value for Δ_{nr}. For the NF sample, the best fit gives $\Delta_{nr} = 28.5\,\text{meV}$, while for the film this value is much higher, $\Delta_{nr} = 70\,\text{meV}$.

This finding demonstrates how differences in the nanomorphology do not just have an impact on the radiative rate and the shape of the PL spectra, but also significantly impact the non-radiative rate. Even more so, compared to changes in the radiative rate, non-radiative processes dominate the photophysical response of P3HT systems.

However, the data shows that the non-radiative rate increases much more strongly in the nanofibre system. This is most likely due to increased order inside the nanofibres, which allow the exciton to diffuse over longer distances and efficiently find non-radiative decay centres. It is also important to note that the description of one non-radiative process is a simplification and probably other decay processes play a role as well.

4.4. Discussion

The presented data shows that there are significant differences in the temperature evolution of P3HT PL spectra, depending on whether the film was spun from chloroform or if it consists of nanofibres.

At low temperatures, the PL lineshape is similar for the film and the fibre samples. All samples show the same peak position, with differences just in R_{em} and in the width of the peaks.

For thin-films of P3HT, the emission behaviour has been shown to be dominated by H-like interchain interaction of the transition dipoles, as a result of dense π-stacking of the polymer backbones and high torsional disorder. R_{em} is a very sensitive probe for structural conformation in the aggregate and is strongly influenced by disorder and by the exciton bandwidth, as described by Equation 4.2.

At the lowest temperature, the NF samples show very similar characteristics to the film, with the transition peaks at the same position and main differences just in the relative intensity of the 0-0 transition. Although disorder is expected to be lower for the NF samples (which would lead to a decreased R_{em}), as can be concluded from the narrower linewidth, a smaller exciton bandwidth W for these samples was extracted from the absorption spectra above. This corresponds to a weaker interchain coupling J_{inter}, which might be the reason why the NF samples exhibit a higher R_{em} than the thin-film at low temperature.

With increasing temperature, the film continues to behave as predicted by the H-aggregate model, while for the NF samples a second progression at higher energy shows up starting at around 125 K. Since this progression is absent in the thin-film sample, it can be assumed that it is related to the highly ordered part in the core of the NFs. With increasing temperature, this progression becomes more dominating and shows a strong blue-shift. This blue-shift can be attributed to a decreased coherence length of the exciton, resulting from a shift away from interchain coupling, to a more intrachain dominated coupling.

In films of P3HT, strong interchain coupling results in the exciton wavefunction being spread along two dimensions, along the polymer backbone and across several polymer chains. However, exciton coherence along one chain is limited by torsional disorder. *C. Silva et al.* found that for low molecular weight P3HT, the exciton coherence length across neighbouring molecules is ~ 10 Å, which corresponds to about 2.5 polymer chains, and the coherence length along the chain ~ 13 Å, which equals around 3 thiophene units. [109] For films of high molecular weight P3HT, which features higher molecular order, the intermolecular spatial coherence is decreased to ~ 7.5 Å, while the coherence along the chain increases to ~ 18 Å.

Responsible for the anisotropic coherence along these two dimensions is a different morphology, from closely packed polymer chains with a high degree of static disorder along one polymer chain, and semicrystalline domains of high molecular weight polymer chains, which show a higher planarity along the polymer backbone. This effect is illustrated in Figure 4.11.

A similar cause is expected for the differences between the films and the NF samples investigated in this study. At low temperature, the PL characteristics are very similar for all samples. It is with increasing temperature, that the fibre samples allow

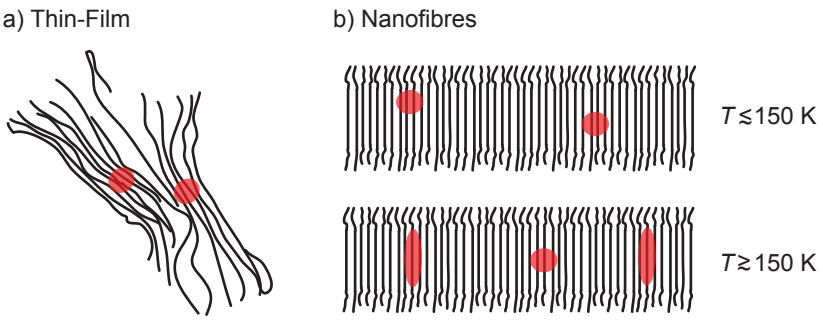

Figure 4.11.: Illustration of the differences in the two-dimensional spatial exciton coherence between P3HT films and nanofibres. The red areas mark the approximate size and shape of the coherence areas for excitons that are predominantly intermolecular (circular) or intramolecular (elongated along one chain) in character.

emission from a species that does not show up in the film sample. It is likely that the change in the PL spectrum is the result of morphological changes in the fibre sample.

Recently, *Martin et. al* reported indication of a structural phase transition in isolated nanofibres. [112] In the temperature dependent PL spectrum, they detect an abrupt change of the PL ratio R_{em} as well as a shift of the position of the 0-0 peak at $\sim 110 - 130\,\mathrm{K}$. The proposed explanation for this phenomenon is that upon increased pressure due to low temperature, the P3HT crystalline structure undergoes a rearrangement of the alkyl side chains which causes more torsional disorder and disrupts the intrachain character. The authors speculate that P3HT might change its packing to a *Type II* configuration, where hexyl side chains are interdigitated, in contrast to the thermally stable *Type I* configuration (compare Sec. 2.4).

The explanation of a temperature dependent re-packing of the P3HT lamella structure is well supported by the data presented in this work. Although the transition is less abrupt and seems to take place gradually between $\sim 125 - 225\,\mathrm{K}$, the temperature range is similar to the one reported by *Martin et al.*. The reason for the more spread out transition is that the NF samples in this work are a mixture of NFs of different size and shape, and although separated by centrifugation, still feature a significant fraction of material that is not incorporated in fibres, but present in the form of smaller aggregates. The exact nature of the transition, and whether a rearrangement to a *Type II* configuration takes place, remains unclear at this point. Due to the

great sensitivity of the transition dipole coupling to packing distance and disorder, it is also possible that much smaller changes in these parameters causes the different PL behaviour. It is however likely that side-chain interactions along the lamella stacking direction play the crucial role in this process. It is necessary to further investigate possible changes in the lamella stacking or in the π-stacking distances by temperature dependent X-ray studies to be able to determine actual repacking processes.

In contrast to the abrupt change in the PL characteristics reported by *Martin et al,*, the gradual transition measured in this work allows the clear observation of coexistence of both phases at $\sim$ 150 K. The observation of multiple vibronic progressions in isolated P3HT NFs has been reported before by *Baghgar et al.*, even when measured at room temperature. [111, 114, 115]. In this study, the authors describe the shape of the measured PL spectra with up to 3 vibronic progressions with different inter- and intrachain character. [111] Similar to previous studies on P3HT films, *Baghgar et al.* observe a strong influence of the molecular weight on whether the PL characteristics are dominated by interchain or by intrachain coupling. They attribute this observation to polymer chain folding within the lamella stack, which gives rise to higher chain planarity and hence increased intrachain coupling. The determination of the chain folding threshold for a given polymer is not trivial, and depends on the solvent system, solution preparation, coating conditions and substrate interactions. [116] However, in the presented case where a high molecular weight P3HT ($M_n \approx 54 - 75$ kg/mol) was used, and a slow fibre formation process employed (in the case of toluene), it is likely that chain folding plays an important role, leading to high intramolecular order for fibres formed from the high molecular weight fraction. The low molecular weight fraction is not expected to take part in the fibre formation process and is instead being removed by the centrifugation step.

The presence of two dominant vibronic progressions at around 150 K indicates that two types of emitting species are present alongside in the NFs, one with dominant interchain character (circular area in Fig. 4.11) and one with dominant intrachain character. This indicates that the fibre morphology is not "perfect" in the sense that all parts show the high planarity that is necessary for J-like behaviour. Instead, less ordered parts and grain boundaries are expected to be present which will show a behaviour that is more similar to the film sample. Especially at lower temperature, when non-radiative decay is suppressed and the excitons can diffuse over longer dis-

tances, emission from the energetically lower lying H-type aggregates will be more dominant.

5. Application of Polythiophene Nanofibres in Optoelectronic Devices

5.1. Organic Thin-Film Transistors

Due to its solution-processability and semicrystalline structure, P3HT is well-suited as semiconducting material in organic thin-film transistors (OTFTs) and hence, significant research efforts were focused on increasing the field-effect mobility of this material. To increase the crystallinity as well as to gain control over the alignment of the crystalline domains, different film-forming methods and surface treatment effects were investigated. With this knowledge, field-effect mobilities as high as 0.1-0.3 cm^2/Vs could be demonstrated. [15, 117–122]

Although this is still significantly lower than mobilities for other polymer systems such as DPP- or DNTT-based compounds which reach field-effect mobilities of $> 1\,\mathrm{cm}^2$/Vs, [123, 124] or pentacene OTFTs with mobilities of $\sim 3\,\mathrm{cm}^2$/Vs, [125, 126] P3HT is a good model system to demonstrate the influence of nanoscale morphology effects on charge transport properties.

The technique of using a nanofibre formation process in solution to control the crystallinity of a P3HT thin-film was presented in Chapter 3, and the influence on the photophysics of the film was investigated. In the following sections, the same technique of using DTBP as an additive will be employed to study the effect on the field-effect mobility of the nanofibre films are used as a semiconducting layer in OTFTs.

5.1.1. Experimental

OTFTs offer the possibility to gain valuable information about the charge transport in a polymer film. Most important, they allow the determination of a value for the

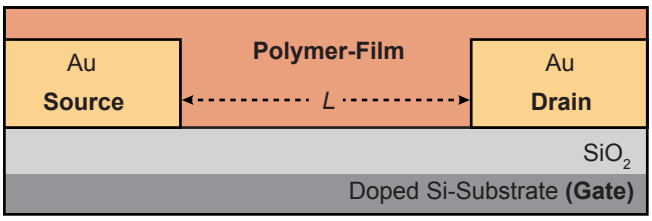

Figure 5.1.: Illustration of an OTFT with bottom-gate structure. L indicates the channel length.

field-effect mobility μ. The basic structure of an OTFT is shown in Figure 5.1. This consists of two ideally ohmic contacts as source and drain contact, separated by a distance L, defining the channel length. The polymer film in the channel forms the active layer. As gate contact, a doped silicon substrate is often used, separated from the organic layer by the gate dielectric, silicon-dioxide (SiO_2). Between the gate-dielectric and the polymer layer, a self-assembled monolayer such as octadecyltrichlorosilane (OTS) or hexamethyldisilazane (HMDS) is often incorporated. By decreasing the surface free energy, the self-organisation of the polymer film near the interface to the dielectric is modified, which can result in increased mobility. [127, 128]

Unlike silicon MOSFETs, organic TFTs usually do not operate in inversion mode, but in accumulation mode. Positively charged carriers are accumulated in the semiconductor near the dielectric interface when a negative V_{GS} is applied (p-channel transistor), or negative charges are accumulated when a positive V_{GS} is applied (n-channel transistor). As shown in Figure 5.1, in organic TFTs, source and drain are implemented by directly contacting the intrinsic semiconductor with a metal. Depending on the choice of the materials for the semiconductor and the contacts, the charge transfer of one carrier type is usually more efficient than that of the other, and this determines whether the device operates as a p-channel or as an n-channel TFT.

Figure 5.2 shows a typical output characteristic of an OTFT. Plotted is the current between source and drain contact, I_{DS}, in dependence of the source-drain voltage, V_{DS}, for varying source-gate voltage, V_{GS}.

A field-effect transistor operates as a voltage-controlled current source. By applying V_{GS} across the gate dielectric, a sheet of mobile charge carriers is induced in the

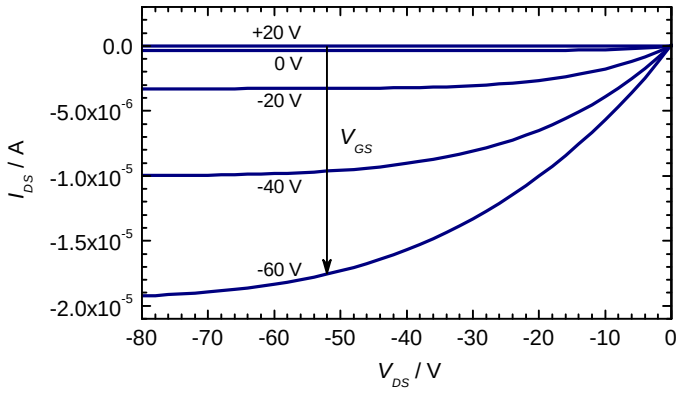

Figure 5.2.: Typical current-voltage characteristics of an organic field-effect transistor for various gate voltages.

semiconductor that allows the current I_{DS} to flow through the semiconductor when V_{DS} is applied.

Because the charge-carrier density in the semiconductor is a function of the gate-voltage, the drain-current can be modulated by adjusting V_{GS}. This modulation is quantitatively described by the most fundamental field-effect transistor parameter, the transconductance g_m,

$$g_m = \left.\frac{\partial I_{DS}}{\partial V_{GS}}\right|_{V_{DS}=\text{const.}} . \tag{5.1}$$

Despite the fact that the transport physics in organic TFTs is different from that in silicon MOSFETs, the current-voltage characteristics can to first order be described with the same formalism, resulting in

$$I_{DS}^{(lin)} = \frac{Z}{L}\mu C_i \left((V_{GS} - V_{th})\, V_{DS} - \frac{V_{DS}^2}{2} \right) \tag{5.2}$$

for $|V_{GS} - V_{th}| > |V_{DS}|$ (the *linear regime*), and

$$I_{DS}^{(sat)} = \frac{Z}{2L}\mu C_i \,(V_{GS} - V_{th})^2 \tag{5.3}$$

for $|V_{DS}| > |V_{GS} - V_{th}|$ (the *saturation regime*). [35, 129] Z is the channel width and C_i the insulator capacitance (per unit area).

For silicon MOSFETs, the threshold voltage V_{th} is defined as the minimum gate-source voltage required to induce strong inversion. Organic TFTs do not operate in inversion mode, but the threshold voltage concept is nonetheless useful for organic TFTs, since V_{th} is the minimum gate-source voltage required to obtain appreciable

drain current, and because the threshold voltage marks the transition between the different regions of operation. [35, 129]

Equation 5.3 allows the determination of μ as well as V_{th} from the transfer characteristics of OTFT-devices by linearly fitting the first derivative or, alternatively, the square root of $I_{DS}(V_{GS})$.

Sample Preparation

The TFT substrates used in this work were purchased from *Fraunhofer-Institut Photonische Mikrosysteme (IPMS)*, Dresden, Germany. The gate substrate is made of 150 nm thick n-doped silicon (doping at wafer surface: $n \approx 3 \cdot 10^{17}$ cm^{-3}), with 230±10 nm SiO_2 as dielectric and with interdigitated ITO (10 nm)/Au (30 nm) source and drain contacts (channel length, $L = 20\,\mu$m and channel width, $Z = 10$ mm). The substrates were treated with oxygen plasma to increase the Au workfunction. A hexamethyldisilazane (HMDS) layer was spin-coated on the samples, annealed at 100 °C for 1 h and spin-washed with isopropyl alcohol.

The P3HT solution and P3HT nanofibre solution was prepared using the same method and the same batch of material that was used for the experiments described in Chapter 3 (P3HT M_n = 54,000-75,000 g/mol, compare Sec. 3.2). DTBP, and all solvents were purchased from Sigma-Aldrich and used without further purification.

The films were deposited by spin-casting the solution at 1000 rpm inside a nitrogen-filled glove box.

Sample Characterisation

The transfer characteristics of the samples were measured using a Karl Suss PM5 probe station and an HP4145 parameter analyser, which was connected to low-noise guarded probes for the source- and drain-contacts and to the probe chuck for the gate connection. For these measurements, the drain-current (I_{DS}) was measured sweeping the gate voltage (V_{GS}) from 20 V to -60 V with a 1 V step and keeping the drain voltage (V_{DS}) constant at -80 V. Electrical characterisation of the TFTs was carried out inside a nitrogen-filled glove box.

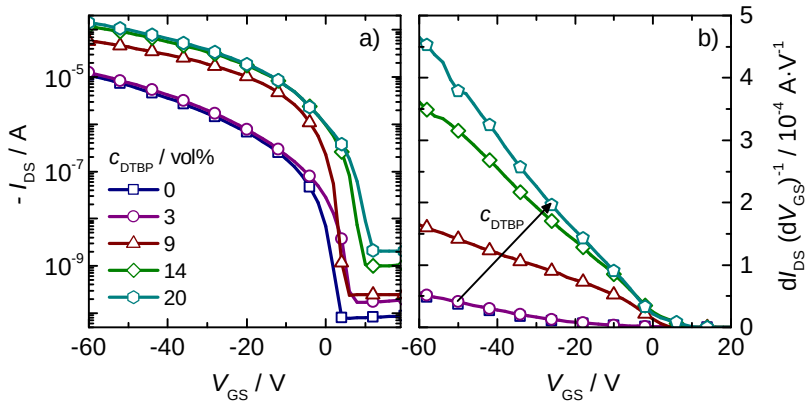

Figure 5.3.: (a) Transfer characteristics of thin-film transistors using P3HT films spin-cast from solutions with different amount of DTBP (measured in saturation regime, $V_{SD} = -80V$). (b) The first derivative of the transfer characteristics.

5.1.2. Results and Discussion

To investigate the influence of the addition of DTBP to a solution of P3HT on the charge transport properties, a set of thin-film transistors (TFTs) was prepared. The samples use films cast from solutions with different concentration of DTBP, c_{DTBP}, up to 20 vol%. Figure 5.3 (a) shows the transfer characteristics of the devices, measured in saturation regime (V_{DS} = - 80 V, comp. Fig. 5.2). It can be seen that the drain-source current I_{DS} for the devices with $c_{DTBP} = 0$ vol% and 3 vol% are very similar. The current starts to increase for higher DTBP concentration of ($c_{DTBP} \geq 9$ vol%). Also, all devices show a high on-off ratio of at least 10^5, although it can be seen that the off-current (I_{DS} at $V_{GS} = 20$ V) is increased for the 14 vol% and 20 vol% case.

The first derivative of Equation 5.3 reads

$$\frac{\partial I_{DS}^{(sat)}}{\partial V_{GS}} = \frac{Z}{L}\mu C_i \left(V_{GS} - V_{th}\right) \ , \tag{5.4}$$

which describes a linear dependence of I_{DS} on V_{GS}, with the prefactor defining the slope of the curve. Therefore, with the knowledge of the substrate-specific parameters Z, L, and C_i, a value for μ can be determined from a linear fit of the experimental values for $\partial I_{DS}/\partial V_{GS}$. Figure 5.3 (b) shows the curves for the samples under investigation. All devices show a good linearity which allows a reliable extraction of the

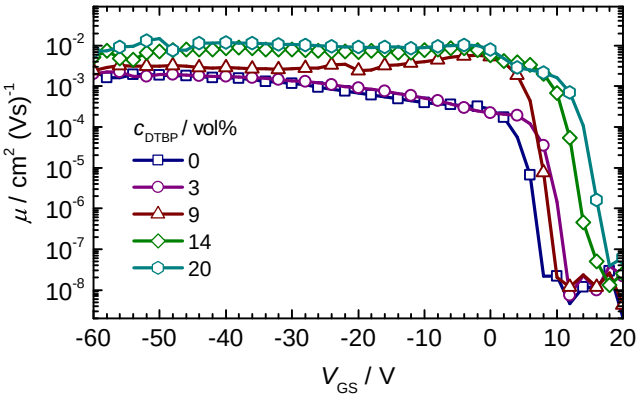

Figure 5.4.: Gate-voltage dependence of μ for different DTBP concentrations, calculated from the second derivative of the transfer characteristics as shown in Figure 5.3.

field-effect mobility. The individual values for μ for the different devices are discussed further below.

The second derivative of Equation 5.3 is the product of the constant ratio of the geometry parameters (Z/L) and the mobility μ. Using the second derivative of the experimental data therefore allows us to calculate the field-dependent mobility, shown in Figure 5.4. Following the curves from positive to negative V_{GS}, it can be seen that for a high DTBP concentration of 14 vol% and 20 vol% the mobility increases sharply at around +18 V and leads into a flat plateau, ranging from 0 V to -60 V. For pristine P3HT and a low c_{DTBP} of 3 vol%, the onset occurs at around +10 V, and the following plateau is tilted. The 9 vol% case shows a somehow intermediate behaviour, with an onset at $\sim$ 10 V and a mainly flat plateau.

A mobility that is independent of the gate voltage has been correlated to high structural order, as seen when comparing films spun from solvents with different boiling points. [47] An increasing mobility with increasing gate voltage indicates a wide distribution of localised states below the mobility edge of trap states, which get filled with increasing carrier concentration. *J. Clark et al.* could show that a higher crystallinity results in a narrower trap distribution, hence the weaker dependence on the gate voltage. [45]

As described in Chapter 3, a good measure for the structural order within the film is the peak ratio $I_{abs}^{0-0}/I_{abs}^{0-1} = R_{abs}$, extracted from the absorption spectra of the thin-

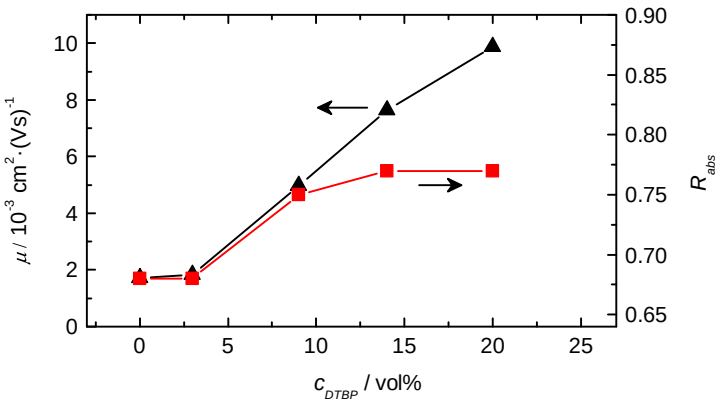

Figure 5.5.: Field-effect mobility μ, obtained from a linear fit of the curves in Figure 5.3, together with the absorption peak ratio R_{abs} for the same c_{DTBP} as listed in Table 3.1.

films. To explore the correlation between molecular order and field-effect mobility, the values for μ, calculated from a linear fit of the data shown in Figure 5.3 (b), are compared to values for R_{abs} that were determined in Section 3.3.3 (comp. Tab. 3.1). The data is shown in Figure 5.5.

It can be seen that the values for $c_{DTBP} = 0$ vol% and $c_{DTBP} = 3$ vol% are almost identical, 2.2×10^{-3} cm^2/Vs and 1.9×10^{-3} cm^2/Vs, respectively. For higher c_{DTBP}, μ starts to increase and reaches a value of 10×10^{-3} cm^2/Vs for $c_{DTBP} = 20$ vol%, a five-fold increase compared to the case of pure P3HT.

This increase in mobility can be attributed to the altered film morphology associated with the fibre formation discussed in Section 3.3.3. It is known that a significant amount of polymer chains in an edge-on orientation can lead to high field-effect mobility. [46] As shown by XRD data in Chapter 3, the polymer chains are highly ordered in π-stacks along the fibre axis, which, when laid out flat on the surface, puts these polymer chains in an edge-on orientation.

The correlation between crystalline quality and mobility can be seen when looking at the trend of R_{abs} in Figure 5.5. R_{abs} increases significantly from 0 vol% up to 9 vol%, but a further increase of the DTBP concentration changes this value only marginally. This suggests that the average of crystallinity of the film cannot be increased further for concentrations greater than 9 vol%. It is surprising, however, that the mobility keeps increasing beyond the 9 vol% concentration of DTBP.

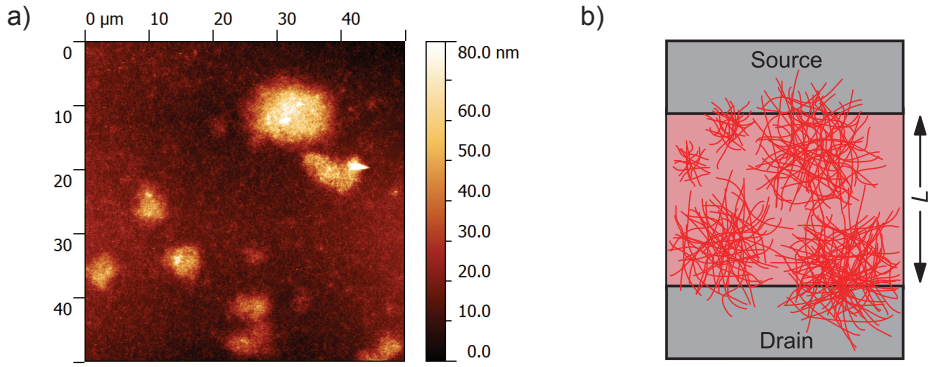

Figure 5.6.: (a) AFM image of DTBP fibres spin-cast on a SiO_2 surface, showing the formation of large fibre bundles. (b) Compared with the channel length $L = 20\,\mu$m of the transistor samples used, these fibre bundles are expected to significantly contribute to the charge transport.

In fact, besides the increased order on a molecular level, a second effect is expected to play an important role that has a significant impact on the measured field-effect mobility. As already mentioned in Section 3.3.2, nanofibres, if not in a dilute solution, tend to form bigger, micrometre sized fibre bundles. Figure 5.6 shows an AFM image of a $50 \times 50 \mu m^2$ area of fibres deposited on a SiO_2 surface. Fibre bundles of different size, with diameter of $> 10\,\mu$m are apparent. Considering a typical fiber length of about $2\,\mu m$, as shown in the AFM images in Chapter 3, and a channel length L of $20\,\mu$m, it is clear that the charge transport cannot occur along just a single fibre, but will have to pass fibre junctions. These junctions can be of different type, either overlaps, contacts, or bifurcations, and it has been shown that the measured mobility obtained by field-effect transistor measurements is determined by a complex interplay between the size of the individual networks and the amount and type of junctions. [130, 131] A way to estimate the maximum size of the networks in this study is by looking at the surface topography measurements shown in Chapter 3 (Fig. 3.5). From this data, it is found that the bundles can be as large as $\sim 25\,\mu$m, i.e. a similar size as the length L of the transistor channel. Therefore, the interconnectivity of the fibres in form of fibre networks plays an important role for the performance of the thin-film transistor, which is illustrated in a cartoon in Figure 5.6. Considering the increasing surface roughness with increasing c_{DTBP} and the saturation behaviour of

the crystallinity, it can be concluded that the increase in mobility at concentrations $c_{DTBP} > 9\,\text{vol}\%$ is most likely due to the formation of larger fibre networks. These networks are shown to be beneficial for the charge transport over relatively large distances of several micrometers, consistent with an extensive study of charge transport in P3HT fibre networks by *Newbloom et al.* [130]

5.1.3. Conclusion

The experiments show how the method of adding DTBP to a solution of P3HT in chlorobenzene can be used to control the OTFT transfer characteristics. An increasing concentration of DTBP increases the mobility of the P3HT film, starting from $c_{DTBP} = 3\,\%$ up to $20\,\%$ roughly linearly. This increase can be partially explained by an increased structural order, which enhances charge transport across polymer chains by dense π-stacking of the polymer backbones over long distances. However, the mobility can be increased further even though the order on a molecular length scale stays constant. This increase can is due to the formation fibre networks, which improve charge transport between the fibres. *Newbloom et al.* have found that in transistors that use P3HT fibre networks as active material, the performance depends on network size, density of the bundles, and the type and shape of the nanofibres (which depends on the formation method and solvent used). [130] In the presented case of DTBP fibres, the main influencing factor is found to be the size and density of the fibre networks, which increases with c_{DTBP} as can be inferred from the surface roughness measurements presented in Chaper 3.

Although the maximum mobility measured for $c_{DTBP} = 20\,\%$ of $\mu = 1 \times 10^{-2}$ cm^2/Vs is still significantly lower than the highest reported values for P3HT based transistors ($\mu \sim 1 \times 10^{-1}$ cm^2/Vs reported in [122]), with the developed method a more than five-fold increase in the mobility compared to the untreated P3HT films can be achieved. Most importantly, the transistor performance is controlled by the solution preparation, and does not depend on particular film-casting methods or post-deposition treatments. It is expected that by further optimisation of the fibre solution like solid content and DTBP concentration a further increase in mobility can be achieved.

5.2. Organic Solar Cells

Although in principle an infinite number of polymers and small molecules can employed in organic solar cells, the by far most commonly used and most intensively investigated system is a heterojunction of P3HT and a soluble fullerene compound, usually phenyl-C61-butyric-acid-methyl (PCBM). This is mainly due to the good solubility of both materials, which leads to ease of fabrication, good stability, and the fact that both materials are widely available. [5, 17, 132] Figure 5.7 shows the chemical structure and energy levels of both materials. [1] It can be seen that the energy

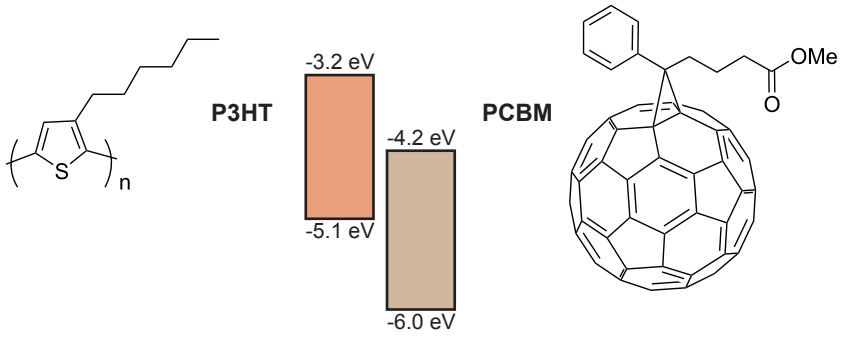

Figure 5.7.: Chemical structures of P3HT and PCBM and the position of HOMO and LUMO of both materials, showing the suitability to form a bulk heterojunction. [133]

offsets of HOMO and LUMO levels are well suited to form a heterojunction for efficient exciton separation as discussed in Chapter 2. According to Equation 2.22, a V_{OC} of 0.6 V should be expected, which is indeed similar to the values which are typically achieved experimentally. Although in the most general view, V_{OC} is determined by the location of the energy levels of donor and acceptor, it has been found that also the nanomorphology of the active layer has a major impact on V_{OC}. [134] Besides the V_{OC}, also other performance parameters are largely affected by morphological changes. This is mainly the case because the morphology of the active layer defines how efficiently excitons are dissociated into electrons and holes, and how well charge carriers get transported and extracted by the electrodes. Many factors are known to

[1] HOMO and LUMO values reported in literature vary to some extent, depending on the technique used and experimental details. Typical values are chosen here, taken from Ref. [133].

have a great impact on the nanomorphology of a P3HT:PCBM heterojunction, such as the casting solvent, the donor-acceptor ratio, the molecular weight, the solution concentration and deposition method. [135–139] Another method to influence the morphology of the active layer is a thermal annealing, which has been shown to be the most effective way to achieve an optimal morphology for the P3HT:PCBM system, resulting in efficiencies of 4.5 % - 6 %. [140, 141] Although a single, primary cause for the increase in efficiency upon thermal treatment has not been conclusively identified, several factors have been shown to play a significant role, such as a change of the domain size of donor and acceptor phase, increased crystallinity of P3HT and PCBM, leading to increased charge carrier mobility, and migration of one or both materials to the electrodes which leads to improved charge extraction. [49, 50, 118, 142–144]

One approach to address the complex issue of morphology control in P3HT:PCBM heterojunctions is the use of P3HT nanofibres. This method allows to more efficiently control the crystallinity of the P3HT phase, as well as partly controlling the intermixing behaviour of the two materials. P3HT nanofibres were successfully employed in solar cells as one way to control the morphology of the active layer when blended in solution with PCBM. [24, 89, 91, 92, 145, 146] Although in the reported cases, little or no increase in efficiency compared to devices with thermal treatment could be achieved, these studies could show that it is possible to obtain an optimal nanomorhphology without an annealing step.

In the following sections, a different approach to incorporate P3HT nanofibres in organic solar cells is presented. The idea is to use the property of the films to become insoluble with sufficient concentration of DTBP to deposit donor and acceptor material successively, and thereby gain better control over the morphology of the active layer. This approach also has the advantage that the donor layer, once it is insolubilsed, can be patterned, and it allows more flexibility in the materials and solvents that can be used as an electron acceptor. Insolubilisation is furthermore of importance if more than two active materials are used in a solar cell stack, e.g. in tandem cells or potentially in ternary systems, [147–149] or to investigate interface effects by placing a third material between donor and acceptor layer. [150]

5.2.1. Experimental

Sample Preparation

P3HT nanofibre solution was prepared using the same method and the same batch of material that was used for the experiments described in Chapter 3 (P3HT M_n = 54,000-75,000 g/mol, compare Sec. 3.2). The used glass substrates have a size of $1 \times 1\,\mathrm{cm}^2$ and were coated with patterned indium tin oxide of 150 nm thickness. They were cleaned in an ultrasonic bath using acetone and isopropyl alcohol and subsequently treated by oxygen plasma for 10 min. PEDOT:PSS (Sigma Aldrich, conductive grade, PEDOT content 0.5 wt. %, PSS content 0.8 %) was applied by spin-coating in ambient conditions. The active materials were spin-coated inside a nitrogen-filled glove box. Contact deposition was performed in a high vacuum evaporation chamber ($p \approx 10^{-6}$ mbar), using a shadow mask to obtain three pixels per substrate each with an active area (overlap with ITO bottom contact) of $14\,\mathrm{mm}^2$.

Sample Characterisation

Current - Voltage Characteristics The response of photovoltaic devices under presence and absence of illumination was measured using a source-measure-unit (SMU, *Keithley 2400*), connected to a computer for data collection and analysis. The illumination was obtained with a class AAA solar simulator (*ABET Technologies*, model *Sun 3000 11016A*). The sample itself was kept in a cylinder which can be loaded in the glove box and which is evacuated to rough vacuum ($p \approx 10$ mbar) during measurement to avoid oxidation of the sample.

External quantum efficiency

The EQE was determined by measuring the short-circuit current, I_{SC}, under illumination of light of a varying wavelength λ and then calculated using

$$EQE(\lambda) = \frac{1240 \cdot I_{SC}}{\lambda \cdot P_{in}} \ , \tag{5.5}$$

where $P_{in}(\lambda)$ is the incident power density (in $\mathrm{W/m}^2$).

The setup to determine the EQE uses a xenon arc lamp as light source, shining light through a monochromator and a beam splitter onto the sample. The beam splitter directs part of the light to a photodiode to record the light intensity P_{in}.

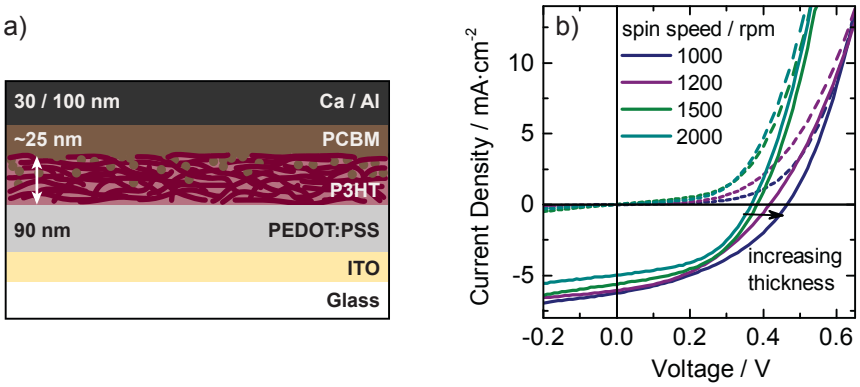

Figure 5.8.: (a) Device architecture of a solar cell that uses a film of P3HT NFs as absorber layer and a subsequently deposited film of PCBM as electron acceptor. The thickness of the P3HT NF layer is varied by different spin speed for film deposition. (b) The effect of different P3HT NF layer thickness on the $J - V$ characteristics of the device, measured in dark conditions (dashed lines) and under 1 sun illumination (straight lines).

The sample is mounted inside a metal cylinder which is evacuated to rough vacuum during measurement. The short-circuit current is measured using a *Keithley 6517A* source-metre.

5.2.2. Results and Discussion

The basic architecture of the device that is investigated in this section is shown in Figure 5.8 (a). It consists of a transparent bottom electrode, made of ITO and a spin-coated film of PEDOT:PSS. The active layer is formed of successively deposited films of P3HT nanofibres and PCBM. The layer thickness of both layers can be varied by changing the speed of the spin-coater. As reflective top electrode, thermally evaporated calcium and aluminium is used.

The film of NFs is prepared using a solution of P3HT with added DTBP in a concentration of $c_{DTBP} = 14\,\text{vol}\%$. This concentration was chosen based on the investigations of surface roughness and film retention of the NF films that were presented in Chapter 3 (see Fig. 3.5). $c_{DTBP} = 14\,\text{vol}\%$ provides already a high degree of film retention ($r = 0.64$) while keeping the film still relatively smooth. For higher concentrations of DTBP, the surface roughness increases strongly which can be a problem

for thin-film devices, since it increases the risk of short-circuits in the device.

The most critical parameter for the fabrication of solar cells with a structure as shown in Figure 5.8 (a) is the thickness of the P3HT NF layer. Figure 5.8 (b) shows the $J-V$ characteristics (measured under 1 sun illumination and under dark conditions) of a range of samples where the P3HT NF film was spin-cast at different spin-coater speed, resulting in thinner films with increasing speed. After film deposition, the P3HT NF layer was spin-rinsed with chlorobenzene to verify the insolubilisation and to remove the amorphous fraction at the surface. An accurate value for the thickness of these films can, due to the significant surface roughness (thickness variation of $\sim \pm 10\,\mathrm{nm}$), not be determined. However, for lowest spin speed (1000 rpm), a thickness of about $50 \pm 10\,\mathrm{nm}$ was measured, while for highest speed (2000 rpm), the thickness is around $20 \pm 10\,\mathrm{nm}$. The subsequent film of PCBM was spin-cast at a speed of 2000 rpm for all devices, resulting in a thickness of about $25 \pm 10\,\mathrm{nm}$. The spin speed for the PCBM layer was found to have a weaker impact on the device performance and is therefore not further investigated in this work. After deposition of the top electrode, all devices were annealed on a hot plate at 150 °C for 10 min. This step is necessary to get a reproducible performance from the devices. The effect of annealing will be described in more detail below.

As can be seen in Figure 5.8 (b), with increasing film thickness, the devices gain in both J_{SC} and V_{OC}. Because a thicker layer is able to absorb more light and hence can contribute to the generation of more charge carriers, the increase in J_{SC} with increasing thickness can be understood intuitively. The large change in V_{OC} is, however, more surprising. It is most likely due to direct pathways of the PCBM phase that connect the electrodes and leads to increased charge recombination at the interface, which decreases V_{OC}. [98] Increasing the thickness of the P3HT NF layer prevents this recombination, hence leading to an increase in V_{OC}. Evidence for direct pathways between electrodes can also be found from the increased leakage current of the dark curves (J in reverse bias), which increases with decreasing layer thickness and indicates a poor blocking behaviour. However, increasing the layer thickness also increases the series resistance of the device which leads to a decreased FF as can be seen in the shown data. Besides the encountered loss in FF, going to higher film thickness is also difficult because the spin speed cannot be decreased further without risking that the substrate will be covered non-uniformly. This is due to the increased

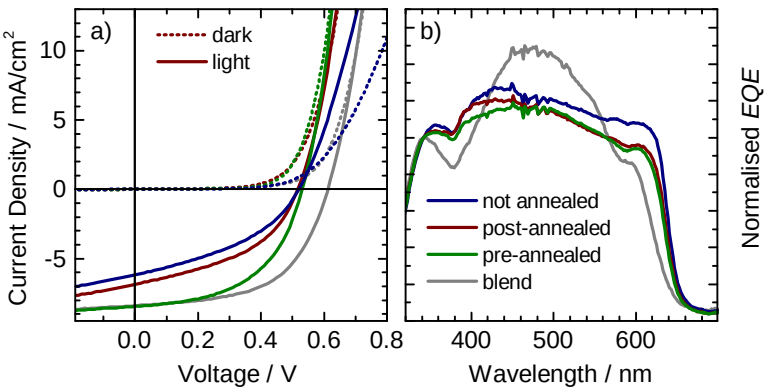

Figure 5.9.: $J-V$ characteristics of P3HT NF solar cells comprising a film of P3HT nanofibres (≈ 50 nm) and a layer of PCBM (≈ 25 nm), measured in dark conditions (dashed line) and under 1 sun illumination (straight line). The devices were either *not* annealed, or annealed at 150°C either after cathode deposition (*post*-annealed), or directly after spin-casting of the PCBM layer, before the cathode was deposited (*pre*-annealed). For comparison, a curve of a solar cell using a 1:0.8 blend of P3HT:PCBM as active layer is shown. (b) External quantum efficiencies (EQE) of the devices shown in (a). The spectra were normalised to allow a better comparison of the shape of the spectra and to highlight the "flatness" of the curves measured for the NF devices.

viscosity of the P3HT + DTBP solution compared to a pure P3HT solution, which requires higher spin speeds to distribute the solution evenly.

For these reasons, a deposition at 1000 rpm was chosen for the P3HT NF deposition in the following experiment, which looks at different annealing treatment of the solar cell samples. Figure 5.9(a) shows the $J-V$ characteristics of three NF devices (structure as shown in Figure 5.8(a) with P3HT NF thickness ~ 50 nm), measured in dark conditions and under illumination. As a reference, the $J-V$ curve of a device with an active layer spin-cast from a blend solution of P3HT:PCBM (1:0.8) is shown as well (gray line). The samples were thermally treated in different ways, either annealed at 150 °C after deposition of the calcium / aluminium cathode (*post-annealed*), annealed after spin-casting the PCBM layer and before depositing the top contact (*pre-annealed*), or without any annealing step. In dark conditions, the pre-

Device	V_{OC} [V]	J_{SC} [mA/cm^2]	FF [%]	η [%]
not annealed	0.52	6.2	40	1.3
pre-annealed	0.53	8.4	52	2.3
post-annealed	0.52	6.8	44	1.6
blend	0.61	8.4	56	2.9

Table 5.1.: Parameters of the solar cells, extracted from the I-V curves shown in Figure 5.9(a).

annealed and the post-annealed devices show similar characteristics. Compared to the non-annealed device, it can be seen how annealing at 150 °C changes the slope of the J-V curve significantly. The current density in forward bias is significantly increased for both annealed devices, which can be attributed to an improved conduction path for charge extraction, and in particular for electrons owing to rearrangement of PCBM molecules near the interface to the P3HT phase and to the top-contact, as previously suggested. [22, 151] The redistribution of PCBM molecules upon annealing also results in a smoothed surface which allows a better contact to the anode and therefore a decreased contact resistance. The smoothing is expected to be more efficient for the pre-annealed device, resulting in a slightly increased current under dark conditions compared to the post-annealed one, although other effects such as specific interactions with the metal electrodes could also play a role.

The efficiency parameters for the individual cells are summarised in Table 5.1. The improved electron transport also results in an increased fill factor for the post-annealed device compared to the non-annealed device from 40 % to 44 %, and an increased power conversion efficiency η from 1.3 % to 1.6 %. However, the short-circuit current (J_{SC}) increases just slightly from 6.2 mA(cm)$^{-2}$ to 6.8 mA(cm)$^{-2}$, indicating that the charge-carrier generation rate is virtually unchanged. In the pre-annealed case, the performance is significantly improved, resulting in a fill factor of 52 %, a J_{SC} of 8.4 mA(cm)$^{-2}$, and $\eta = 2.3$ %. The higher J_{SC} indicates a higher charge generation, caused by an increased P3HT / PCBM interface area, since a significant variation due to a difference in the charge extraction paths should also result in more prominent differences in the dark $J - V$ characteristics than observed.

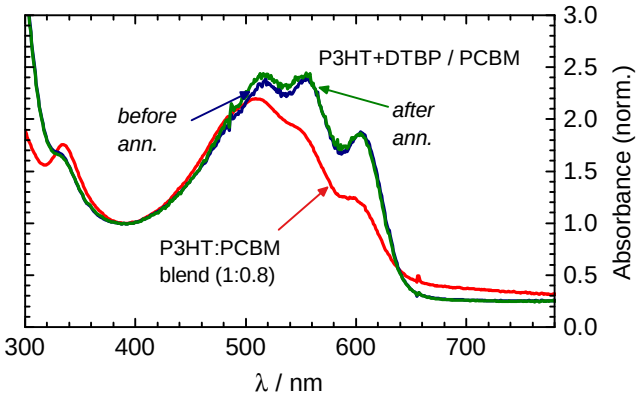

Figure 5.10.: Absorption spectra (normalised at local minimum at $\sim$ 395 nm) of P3HT NF / PCBM films on PEDOT:PSS, similar to the films used as active layer in the device shown in Fig. 5.8 (a), before and after annealing at 150 °C. The spectra are compared to a film of a P3HT:PCBM blend (ratio 1 : 0.8).

This scenario is consistent with diffusion of PCBM into the P3HT phase, as also reported by *Chen et al.* by using neutron scattering techniques. [151] Interestingly, the diffusion behaviour is strongly influenced by the presence of the top contact, which presumably hinders the movement of the PCBM molecules upon annealing. It is also likely that intermixing already takes place during the deposition of PCBM due to swelling of P3HT in chlorobenzene and a partial removal of amorphous fraction. [152]

Figure 5.10 shows the UV-vis absorption spectrum of the successively deposited P3HT NF / PCBM films compared to a spectrum of a film of a P3HT:PCBM (1:0.8) blend. The increased absorption in the 500 nm - 640 nm region due to the crystallinity of the P3HT is preserved after the PCBM deposition, and also after annealing of the bilayer, the absorption spectrum does not change significantly. This suggests that even in the presence of an expected diffusion of PCBM into the P3HT layer, the intermixing mainly takes place in the amorphous P3HT domains, and leaves the crystalline domains effectively unchanged. [15] The intermixing of P3HT and PCBM plays an important role in the performance of the device, since it increases the donor-acceptor interface area and can help to form an interpenetrating network beneficial for charge extraction.

Further insight about the morphology can be extracted from the external quantum efficiency (EQE) of the devices. Shown in Figure 5.9(b) are the spectra for the four devices discussed above (non-annealed, pre-annealed, post-annealed, and blend device). The spectral shapes of the P3HT NF devices are almost identical, while they strongly differ from the blend device. The NF device spectra feature a plateau between $\sim$ 400 nm and $\sim$ 600 nm, while the spectrum of the blend device has a pronounced maximum at $\sim$ 470 nm. This behaviour can be explained by a filter effect due to the relatively large thickness of the P3HT layer. Incoming light near the absorption maximum of P3HT gets absorbed more strongly before it can reach the P3HT / PCBM interface than light at around the low and high wavelength end of the absorption spectrum. [2] In a blend layer, where the exciton-splitting donor-acceptor interface is distributed through the whole depth of the layer, this filter effect does not show up. It is therefore possible to take the shape of the EQE spectrum as an indicator for how much the morphology matches a real bilayer structure, i.e. how sharp the interface between donor and acceptor is. [153]

Figure 5.10 shows that there is virtually no difference in the shape of the pre-annealed and the post-annealed device. This indicates that the interdiffusion of the PCBM and P3HT layer happens near the interface, and the PCBM molecules cannot penetrate deeply into the P3HT layer, preserving the multilayer-structure to a large extend. This is in agreement with earlier findings that suggest that the diffusion of the PCBM molecules primarily takes place in the amorphous phase of the P3HT layer, resulting in a morphology similar to film cast from a blend solution already after just seconds of annealing at 150 °C. [151] However, the high crystallinity of the P3HT in the present case prevents this strong interdiffusion.

5.2.3. Conclusions

The experiments successfully demonstrate an alternative method for the fabrication of organic solar cells by successive deposition of the donor and acceptor material. This method provides additional control over the morphology of the active layer, and opens up the possibility to apply additional patterning techniques. It was found that

[2] Assuming a P3HT layer thickness of 40 nm and an absorption coefficient of 0.005 nm^{-1} at 470 nm and 0.001 nm^{-1} at 600 nm, gives a 45% higher intensity of 600 nm photons compared to 470 nm photons after light has travelled through this layer.

the thickness of the P3HT NF film strongly impacts the performance of the devices, which is mainly due to a change in V_{OC}. All NF devices that were fabricated show a significantly lower V_{OC} compared to similar P3HT:PCBM blend devices, with a maximum of 0.53 V, which is ~ 100 mV lower than for a typical P3HT:PCBM cell. It is likely that this decrease in V_{OC} is due to direct pathways between the electrodes, caused by the high surface roughness of the P3HT NF film and diffusion of PCBM to the bottom electrode. To achieve highest efficiency, the cells have to be thermally annealed before contact deposition, however, the V_{OC} does not change with thermal annealing.

In contrast to this finding, *Chen et al.* report a sharp increase in V_{OC} with thermal annealing of P3HT / PCBM bilayer solar cells, from initially 0.36 V, to 0.50 V already after just 5 s of annealing at 150 °C. [151] They attribute this increase to the fast intermixing of the PCBM and amorphous P3HT phase. The unchanged V_{OC} for the presented case of P3HT NF solar cells therefore indicates that intermixing of the phases with thermal annealing takes place to a lesser extent than what was reported for the bilayer cells. The same conclusion can be reached from the shape of the EQE spectra, which does not change significantly. The increased performance is therefore attributed mainly to an improved contact at the interface to the electrodes. It is most likely the contact to the top electrode that has the biggest impact, as can be inferred from the different behaviour of the pre-annealing and the post-annealing treatment. Post-annealing seems to hinder the PCBM molecules from movement and therefore prevents the formation of an improved electrical contact. Annealing before the metal deposition allows the redistribution of PCBM molecules at the surface and the contact to the subsequently deposited calcium and aluminium is improved.

Due to the decreased V_{OC}, the efficiency of the fabricated P3HT NF cells ($PCE = 2.3\,\%$) is still lower than for the blend devices (PCE for the same P3HT batch and prepared in the same lab at UCL is $\sim 3\,\%$). Interestingly, the J_{SC} is the same for both devices, which is surprising considering the fact that a large fraction of the P3HT polymer chains is oriented in an edge-on orientation when incorporated in nanofibres. Charge transport to the electrodes will therefore have to take place mainly across the lamella stacks, which is less efficient than along the π-stacking direction due to the greater intermolecular distance. [46]

The similar J_{SC} of NF solar cells and blend devices suggests that it is mainly

an interface effect between the active layer and the electrodes that is responsible for the difference in performance. Improvement of the film quality of the NF layer by optimising the DTBP concentration and coating conditions to obtain a reduced surface roughness is expected to further increase the performance of the devices.

6. Summary and Conclusions

Fabrication and Properties of Polythiophene Nanofibres The work presented in Chapter 3 shows that DTBP can be used as an additive to a solution of P3HT in chlorobenzene to increase the overall crystallinity of P3HT films. The change in crystallinity can be detected by a change in the shape of the absorption spectrum as well as with the help of X-ray diffraction measurements. Both measurements indicate the formation of P3HT lamella stacks with a stack spacing of $\sim 1.6\,\mathrm{nm}$ known as Type I packing structure. Besides the change in crystallinity, the addition of DTBP also allows control of the film retention. It could be shown that the underlying process of the altered film properties is a formation of micrometer-sized nanofibres (NFs). The shape and dimensions of the NFs were investigated by AFM, and the nanofibres are found to be around 50 nm wide and several micrometers in length. The height of the NFs varies, from $< 2\,\mathrm{nm}$ to $\sim 8\,\mathrm{nm}$, and the measured values are discrete, correlating with a different number of lamella stacks. To be able to measure the dimension of individual fibres, the solution has to be diluted before deposition. However, if a higher concentrated solution is used, like the 10 mg/ml solution used for the film deposition, the fibres tend to form larger bundles in the range of several micrometers, which are most likely the main reason why the films become insoluble with increasing DTBP concentration. The larger size of these bundles made it possible to detect the PL using a SNOM, however, it remains challenging to image individual NFs due to their small size and soft nature, which bears the risk of getting easily displaced or damaged by the scanning probe. Preliminary experiments to align the NFs in a high magnetic field were performed and an alignment effect detected at a field strength of $\sim 2\,\mathrm{T}$ and a partial saturation at $\sim 4\,\mathrm{T}$. Attempts to deposit aligned fibres on a substrate were not successful, due to solvent drying effects counteracting weak alignment forces induced by the magnetic field.

Suggestions for Additional Characterisation Methods One of the remaining challenges connected to the presented work is the preparation of films with highly aligned NFs. The alignment would allow the polarisation-dependent investigation of optical absorption and photoluminescence. This has the advantage that the highly ordered part can be isolated from the less ordered part of non aggregated polymer chains which surround the fibres or protrude from the fibre core.

Within this work, a range of experiments were performed that were focused on the alignment of the NFs, in addition to the measurements in a high magnetic field that were described in Chapter 3. This included attempts to achieve an alignment by mechanically rubbing of NF films, drop-casting the solution on a horizontally tilted substrate, as well as attempts to achieve a directional growth of the NFs by spatial confinement, using a PDMS grating.

However, so far none of the mentioned techniques could be successfully applied. The main difficulty lies in the fragile nature of the fibres, which limits the mechanical force that can be applied to the NFs. The small dimensions also make it susceptible to small forces that counteract any alignment, like convection flows of solvent during drying as well as the tendency of the fibres to aggregate to networks, which are disordered and counteract alignment of the individual fibres.

Another possibility to obtain polarisation-resolved information from the fibres is with the help of imaging techniques with high spatial resolution. One possibility was explored in this work by using a SNOM to image the fibres and to detect the PL. As mentioned above, this task remains challenging due to the relatively large dimensions of the scanning probe compared to the NF dimensions and the use of shear forces to follow the topography of the surface. Furthermore, the small dimensions of the fibres combined with the low PL quantum efficiency of P3HT results in a very low intensity of the PL signal and hence requires an extremely sensitive photon detector system.

Other optical imaging techniques like a confocal microscopy were also explored within this work. The advantage of this technique compared to SNOM is that it operates contact-less. However, the resolution is diffraction limited, with spot-sizes of at least $\sim 0.2\,\mu$m, which is large compared to the NF width and height in the range of nanometres. It is therefore not suited to determine the shape of the fibres. However, confocal microscopy has been employed by some groups to detect the PL of P3HT NFs. [111, 112]. Although the authors argue that the measured PL originates

from individual NFs, the actual shape of these fibres is not reported, and it remains unclear whether the detected features are individual self-assembled NFs like the ones investigated in this work, or if the PL was measured from larger aggregates in the form of fibre networks.

Temperature-dependent Photoluminescence of Polythiophene Nanofibres The PL of P3HT films and P3HT NFs was measured at varying temperature, ranging from room temperature to $\sim 7\,\mathrm{K}$. It was found that the PL behaviour differs significantly between the samples, most strongly at an intermediate temperature of $\sim 175\,\mathrm{K}$. At this temperature, the NF spectra show evidence of a transition between two vibronic progressions, with an increasing intensity of the higher energy progression with increasing temperature. The low temperature spectrum of the NF samples shows great similarity with the P3HT thin-film spectrum, that can be explained by polymer aggregates in which the interchain coupling dominates over intrachain coupling (H-type coupling). However, the character of the second progression is more difficult to determine, since several effects are contributing simultaneously to the shape of the spectrum. This is in general the PL temperature dependence of the particular type of aggregate, as determined from the location of energy levels and strength of transition dipole moments, and as a second factor possible changes in morphology of the aggregate, which can alter the relative strengths of inter- and intrachain coupling dramatically.

It is most likely the latter effect that dominates the PL behaviour for the measurements presented in this work. The second progression, which only shows up in the spectra of the NFs, is expected to originate from a larger contribution of intrachain coupling than it is the case for the P3HT film. An increased strength of J_{intra} results in a larger relative contribution of I_{PL}^{0-0}. This is opposite to the trend that is predicted from the energetics of pure J-aggregates, which predicts a sharp decrease in I_{PL}^{0-0} with increasing temperature. The exact reason for the rather abrupt change of J_{inter} and J_{intra} at around $\sim 175\,\mathrm{K}$ cannot be determined with the employed measurement method. It is likely that the reason for the altered dipole coupling behaviour is a change in torsional disorder of the polymer backbones in the π-stack, caused by alkyl side chain interactions. Decreasing temperature increases the pressure on these chains which induces higher torsional disorder, which interrupts the coupling along

the polymer backbone. Increasing temperature releases this pressure and allows the backbone to planarise, which is more apparent in the NF films because of the higher structural order as proven by X-ray diffraction. Interestingly, no indication for an abrupt phase transition is visible from the evolution of the overall PL intensity of the NF films and the behaviour can in contrast be explained by a single thermally activated non-radiative decay mechanism. The drop in PL efficiency with increasing temperature is much stronger for the NF samples, meaning that non-radiative decay processes are more efficient in the NFs than they are in P3HT films. Also this can be explained by the high structural order in the NFs which allows the excitons to diffuse over wider ranges and therefore find non-radiative decay centres more efficiently.

Suggestions for Complementary Experiments to the PL Measurements To complement the PL measurements and to help to validate the suspected structural phase transition at a temperature of around 125-225 K, temperature-dependent X-ray diffraction experiments could be employed. As shown in Section 3.3.3, X-ray diffraction measurements are well suited to probe the lamella spacing of P3HT aggregates. Following the argumentation in the previous paragraph, a shift towards a smaller interlamella distance with decreasing temperature would be expected. The fact that the specifics of the NF samples can be probed on a relatively thick layer of NFs should positively impact the signal to noise ratio of the measurement.

As discussed above, to gain more information about the photophysics, polarisation dependent measurements either on individual fibres or on films of aligned fibres could be performed.

Another aspect of the PL characteristics of the NFs that has not been investigated within this work are time-resolved PL measurements. It was found that the PL of P3HT typically consists of a fast (≤ 1 ns) component, and a slow component, which seems to follow a power law behaviour rather than an exponential decay. [154–157] First experiments on P3HT NFs show a change in the relative contribution of the fast and slow component, with a reduced fast component for the fibres. [110, 112, 158] This can be explained assuming that the fast component mainly results from exciton dissociation into polaron pairs at the borders of crystalline domains, a process which will be less likely in highly ordered systems like P3HT NFs. The process in the long time domain has been found to be related to the characteristic electron-hole

separation and to the distance dependence of charge tunnelling, and first experimental evidence that these parameters change with the size of crystalline domains exists. [157, 158]

Application of Polythiophene Nanofibres in Optoelectronic Devices Both OTFTs and solar cells could be fabricated making use of the specific properties of P3HT NF films that were described in Chapter 3. The increased crystallinity of the films made from a solution with $c_{DTBP} \geq 9\,\text{vol}\%$ results in an increased field-effect mobility of these films compared to P3HT films without DTBP treatment. In addition to the higher order on a molecular level, also the formation of micrometre-sized fibre networks leads to an improved charge transport and contributes to a higher mobility.

It could be shown that the high film retention of NF films with $c_{DTBP} = 14\,\text{vol}\%$ can be used for the fabrication of P3HT:PCBM solar cells by successive deposition of donor and acceptor layer from the same solvent. Due to the high amount of the crystalline P3HT fraction and the different fabrication technique, these solar cells are expected to show a significantly different nanomorphology compared to standard P3HT:PCBM blend devices. Nevertheless, after annealing, these devices show a performance comparable to P3HT:PCBM blend solar cells, lacking just in V_{OC} and still reaching a power conversion efficiency of up to 2.3 %. It is expected that further optimisation of the film thickness and roughness by finding the right DTBP concentration and spin-coating parameters, an even higher PCE can be achieved.

Suggestions for Further Work on Applications It would be interesting to look at OTFT characteristics if the NFs in the transistor channel are aligned. An array of oriented NFs is expected to significantly improve charge transport and to result in high mobility due to the charge transport being highly dependent on the orientation of the P3HT crystalline domains. [46, 65, 119, 159] As mentioned above, the alignment of P3HT NFs has been attempted in the framework of this thesis, but did not give satisfactory results so far.

A high degree of orientation of the P3HT crystalline domains is also interesting for photovoltaic applications, as has been shown by *Zhu et al.* who demonstrated P3HT solar cells that also act as a polariser. [160]

The presented technique for the fabrication of solar cells by successive deposition

of the acceptor material on top of a film of NFs could be improved to increase the efficiency of the devices. To investigate the correlation between the morphology of the NF layer and solar cell performance, techniques like transmission electron spectroscopy, small angle neutron scattering or X-ray scattering are well suited to obtain more information about the arrangement of donor and acceptor phase in the active layer. [151, 152]

Bibliography

[1] Raghu Das and Peter Harrop. Printed, Organic & Flexible Electronics: Forecasts, Players & Opportunities 2013-2023. Technical report, IDTechEx, 2013.

[2] Sebastian Reineke, Frank Lindner, Gregor Schwartz, Nico Seidler, Karsten Walzer, Björn Lüssem, and Karl Leo. White organic light-emitting diodes with fluorescent tube efficiency. *Nature*, 459(7244):234–238, 2009.

[3] Antonio Facchetti. Organic Semiconductors - Made to order. *Nature Materials*, 12(July):598, 2013.

[4] Roar Søndergaard, Markus Hösel, Dechan Angmo, Thue T. Larsen-Olsen, and Frederik C. Krebs. Roll-to-roll fabrication of polymer solar cells. *Materials Today*, 15(1-2):36–49, January 2012.

[5] Mikkel Jørgensen, Jon E. Carlé, Roar R. Søndergaard, Marie Lauritzen, Nikolaj A. Dagnæs-Hansen, Sedi L. Byskov, Thomas R. Andersen, Thue T. Larsen-Olsen, Arvid P. L. Böttiger, Birgitta Andreasen, Lei Fu, Lijian Zuo, Yao Liu, Eva Bundgaard, Xiaowei Zhan, Hongzheng Chen, and Frederik C. Krebs. The state of organic solar cells - A meta analysis. *Solar Energy Materials and Solar Cells*, 119:84–93, December 2013.

[6] F. Padinger, R. S. Rittberger, and N. S. Sariciftci. Effects of Postproduction Treatment on Plastic Solar Cells. *Advanced Functional Materials*, 13(1):85–88, January 2003.

[7] Xiaoniu Yang, Joachim Loos, Sjoerd C. Veenstra, Wiljan J. H. Verhees, Martijn M. Wienk, Jan M. Kroon, Matthias A. J. Michels, and René A. J. Janssen. Nanoscale morphology of high-performance polymer solar cells. *Nano Letters*, 5(4):579–83, April 2005.

[8] W. Ma, C. Yang, X. Gong, K. Lee, and A. J. Heeger. Thermally Stable, Efficient Polymer Solar Cells with Nanoscale Control of the Interpenetrating Network Morphology. *Advanced Functional Materials*, 15(10):1617–1622, October 2005.

[9] Hsiang-Yu Chen, Jianhui Hou, Shaoqing Zhang, Yongye Liang, Guanwen Yang, Yang Yang, Luping Yu, Yue Wu, and Gang Li. Polymer solar cells with enhanced open-circuit voltage and efficiency. *Nature Photonics*, 3:649–653, 2009.

[10] Markus C. Scharber, Markus Koppe, Jia Gao, Fabrizio Cordella, Maria A. Loi, Patrick Denk, Mauro Morana, Hans-Joachim Egelhaaf, Karen Forberich, Gilles Dennler, Russ Gaudiana, Dave Waller, Zhengguo Zhu, Xiaobo Shi, and Christoph J. Brabec. Influence of the bridging atom on the performance of a low-bandgap bulk heterojunction solar cell. *Advanced Materials*, 22(3):367–70, January 2010.

[11] Yanming Sun, Gregory C. Welch, Wei Lin Leong, Christopher J. Takacs, Guillermo C. Bazan, and Alan J. Heeger. Solution-processed small-molecule solar cells with 6.7% efficiency. *Nature Materials*, 11(1):44–8, January 2012.

[12] M. C. Scharber and N. S. Sariciftci. Efficiency of bulk-heterojunction organic solar cells. *Progress in Polymer Science*, 38(12):1929–1940, December 2013.

[13] Martin A. Green, Keith Emery, Yoshihiro Hishikawa, Wilhelm Warta, and Ewan D. Dunlop. Solar cell efficiency tables (version 44). *Progress in Photovoltaics: Research and Applications*, 22(7):701–710, 2014.

[14] Nieves Espinosa, Markus Hösel, Mikkel Jørgensen, and Frederik C. Krebs. Large scale deployment of polymer solar cells on land, on sea and in the air. *Energy & Environmental Science*, 7(3):855, 2014.

[15] H. C. Yang, T. J. Shin, L. Yang, K. Cho, C. Y. Ryu, and Zhenan Bao. Effect of mesoscale crystalline structure on the field-effect mobility of regioregular poly(3-hexyl thiophene) in thin-film transistors. *Advanced Functional Materials*, 15(4):671, April 2005.

[16] Minh Trung Dang, Lionel Hirsch, and Guillaume Wantz. P3HT:PCBM, Best Seller in Polymer Photovoltaic Research. *Advanced Materials*, 23(31):3597–3602, August 2011.

[17] Xiaohan Yang and Ashraf Uddin. Effect of thermal annealing on P3HT:PCBM bulk-heterojunction organic solar cells: A critical review. *Renewable and Sustainable Energy Reviews*, 30:324–336, February 2014.

[18] Martin Brinkmann. Structure and Morphology Control in Thin Films of Regioregular Poly(3-hexylthiophene). *Journal of Polymer Science Part B - Polymer Physics*, 49(17):1218, September 2011.

[19] Michael A. Brady, Gregory M. Su, and Michael L. Chabinyc. Recent progress in the morphology of bulk heterojunction photovoltaics. *Soft Matter*, 7(23):11065, 2011.

[20] Kyo Jin Ihn, Jeff Moulton, and Paul Smith. Whiskers of poly(3-alkylthiophene)s. *Journal of Polymer Science Part B: Polymer Physics*, 31(6):735–742, May 1993.

[21] I. R. Gearba, C. Y. Nam, R. Pindak, and C. T. Black. Thermal crosslinking of organic semiconducting polythiophene improves transverse hole conductivity. *Applied Physics Letters*, 95(17):173307, October 2009.

[22] Ankit Kumar, Gang Li, Ziruo Hong, and Yang Yang. High efficiency polymer solar cells with vertically modulated nanoscale morphology. *Nanotechnology*, 20(16):165202, April 2009.

[23] Jeffrey A. Merlo and C. Daniel Frisbie. Field Effect Transport and Trapping in Regioregular Polythiophene Nanofibers. *The Journal of Physical Chemistry B*, 108(50):19169–19179, December 2004.

[24] Solenn Berson, Remi De Bettignies, Severine Bailly, and Stephane Guillerez. Poly (3-hexylthiophene) fibers for photovoltaic applications. *Advanced Functional Materials*, 17(8):1377, May 2007.

[25] Wibren D. Oosterbaan, Veerle Vrindts, Solenn Berson, Stéphane Guillerez, Olivier Douhéret, Bart Ruttens, Jan D'Haen, Peter Adriaensens, Jean Manca, Laurence Lutsen, and Dirk Vanderzande. Efficient formation, isolation and characterization of poly(3-alkylthiophene) nanofibres: probing order as a function of side-chain length. *Journal of Materials Chemistry*, 19(30):5424, 2009.

[26] Michael Hoffmann and Karl Leo. *Organic Semiconductors - University Lecture*. Technische Universität Dresden, 2006.

[27] Franco Cacialli. *Plastic and Molecular Electronics - University Lecture*. University College London, 2010.

[28] M. Pope and C. Swenberg. *Electronic Processes in Organic Crystals and Polymers*. Oxford University Press, 1999.

[29] Christoph Brabec, Vladimir Dyakonov, Juergen Parisi, and Niyazi Sariciftci. *Organic Photovoltaics*. Springer-Verlag, 2003.

[30] Christoph Brabec, Vladimir Dyakonov, and Ullrich Scherf. *Organic Photovoltaics*. Wiley-VCH Verlag Gmbh & Co. KGaA, 2008.

[31] Thorsten U. Kampen. *Low Molecular Weight Organic Semiconductors*. John Wiley & Sons, 2011.

[32] Mark Geoghegan and Georges Hadziioannou. *Polymer Electronics*. Oxford University Press, 2013.

[33] Robert S. Knox. Förster's resonance excitation transfer theory: not just a formula. *Journal of Biomedical Optics*, 17(1):011003, January 2012.

[34] D. L. Dexter. A Theory of Sensitized Luminescence in Solids. *The Journal of Chemical Physics*, 21(5):836, 1953.

[35] G. Horowitz. Organic field-effect transistors. *Advanced Materials*, 10(5):365, 1998.

[36] Flora M. Li, Arokia Nathan, Yiliang Wu, and Beng S. Ong. *Organic Thin Film Transistor (OTFT) Overview, in Organic Thin Film Transistor Integration: A Hybrid Approach*. Wiley-VCH Verlag GmbH & Co. KGaA, 2011.

[37] M. Kasha. Energy Transfer Mechanisms and the Molecular Exciton Model for Molecular Aggregates. *Radiation Research*, 20(1):55–70, 1963.

[38] Michael R. Philpott. Theory of the Coupling of Electronic and Vibrational Excitations in Molecular Crystals and Helical Polymers. *The Journal of Chemical Physics*, 55(5):2039, 1971.

[39] H. Yamagata, J. Norton, E. Hontz, Y. Olivier, D. Beljonne, J. L. Brédas, R. J. Silbey, and F. C. Spano. The nature of singlet excitons in oligoacene molecular crystals. *The Journal of Chemical Physics*, 134(20):204703, May 2011.

[40] F. C. Spano. Modeling disorder in polymer aggregates: The optical spectroscopy of regioregular poly(3-hexylthiophene) thin films. *Journal of Chemical Physics*, 122(23):234701, June 2005.

[41] Frank C. Spano, Jenny Clark, Carlos Silva, and Richard H. Friend. Determining exciton coherence from the photoluminescence spectral line shape in poly(3-hexylthiophene) thin films. *The Journal of Chemical Physics*, 130(7):074904, February 2009.

[42] Frank C. Spano. The Spectral Signatures of Frenkel Polarons in H- and J-Aggregates. *Accounts of Chemical Research*, 43(3):429–439, 2010.

[43] Frank C. Spano and Hajime Yamagata. Vibronic Coupling in J-Aggregates and Beyond: A Direct Means of Determining the Exciton Coherence Length from the Photoluminescence Spectrum. *Journal of Physical Chemistry B*, 115(18):5133, May 2011.

[44] Jenny Clark, Carlos Silva, Richard Friend, and Frank Spano. Role of Intermolecular Coupling in the Photophysics of Disordered Organic Semiconductors: Aggregate Emission in Regioregular Polythiophene. *Physical Review Letters*, 98(20):206406, May 2007.

[45] Jenny Clark, Jui-Fen Chang, Frank C. Spano, Richard H. Friend, and Carlos Silva. Determining exciton bandwidth and film microstructure in polythiophene films using linear absorption spectroscopy. *Applied Physics Letters*, 94(16):163306, 2009.

[46] H. Sirringhaus, P. J. Brown, R. H. Friend, M. M. Nielsen, K. Bechgaard, and A. J. H. Spiering. Two-dimensional charge transport in conjugated polymers. *Nature*, 401:685–688, 1999.

[47] Jui-Fen Chang, Baoquan Sun, Dag W. Breiby, Martin M. Nielsen, Theis I. Sölling, Mark Giles, Iain McCulloch, and Henning Sirringhaus. Enhanced

Mobility of Poly(3-hexylthiophene) Transistors by Spin-Coating from High-Boiling-Point Solvents. *Chemistry of Materials*, 16(23):4772–4776, November 2004.

[48] Marisol Reyes-Reyes, Kyungkon Kim, and David L. Carroll. High-efficiency photovoltaic devices based on annealed poly(3-hexylthiophene) and 1-(3-methoxycarbonyl)-propyl-1- phenyl-(6,6)C[sub 61] blends. *Applied Physics Letters*, 87(8):083506, 2005.

[49] V. D. Mihailetchi, H. X. Xie, B. de Boer, L. J. A. Koster, and P. W. M. Blom. Charge transport and photocurrent generation in poly (3-hexylthiophene): methanofullerene bulk-heterojunction solar cells. *Advanced Functional Materials*, 16(5):699–708, March 2006.

[50] Y. Kim, S. Cook, S. M. Tuladhar, S. A. Choulis, J. Nelson, J. R. Durrant, D. D. C. Bradley, M. Giles, I. McCulloch, C. S. Ha, and M. Ree. A strong regioregularity effect in self-organizing conjugated polymer films and high-efficiency polythiophene: fullerene solar cells. *Nature Materials*, 5(3):197, March 2006.

[51] Mariano Campoy-Quiles, Toby Ferenczi, Tiziano Agostinelli, Pablo G. Etchegoin, Youngkyoo Kim, Thomas D. Anthopoulos, Paul N. Stavrinou, Donal D. C. Bradley, and Jenny Nelson. Morphology evolution via self-organization and lateral and vertical diffusion in polymer:fullerene solar cell blends. *Nature Materials*, 7(2):158–64, February 2008.

[52] T. J. Prosa, M. J. Winokur, J. Moulton, P. Smith, and A. J. Heeger. X-ray Structural Studies of Poly(3-alkylthiophenes) - An Example of An Inverse Comb. *Macromolecules*, 25(17):4364, August 1992.

[53] Jostein Mårdalen, Emil J. Samuelsen, Odd R. Gautun, and Per H. Carlsen. X-ray scattering from oriented poly(3-alkylthiophenes). *Synthetic Metals*, 48:363–380, 1992.

[54] T. J. Prosa, M. J. Winokur, and R. D. McCullough. Evidence of a Novel Side Chain Structure in Regioregular Poly(3-alkylthiophenes). *Macromolecules*, 29:3654–3656, 1996.

[55] Christopher A. Hunter and Jeremy K. M. Sanders. The nature of pi-pi interactions. *Journal of the American Chemical Society*, 112(14):5525–5534, 1990.

[56] Eun Cheol Lee, Dongwook Kim, Petr Jurecka, P. Tarakeshwar, Pavel Hobza, and Kwang S. Kim. Understanding of assembly phenomena by aromatic-aromatic interactions: Benzene dimer and the substituted systems. *Journal of Physical Chemistry A*, 111(18):3446, May 2007.

[57] Chelsea R. Martinez and Brent L. Iverson. Rethinking the term "pi-stacking". *Chemical Science*, 3(7):2191, 2012.

[58] A. Zen, M. Saphiannikova, D. Neher, J. Grenzer, S. Grigorian, U. Pietsch, U. Asawapirom, S. Janietz, U. Scherf, I. Lieberwirth, and G. Wegner. Effect of molecular weight on the structure and crystallinity of poly(3-hexylthiophene). *Macromolecules*, 39(6):2162, March 2006.

[59] Guanghao Lu, Ligui Li, and Xiaoniu Yang. Achieving perpendicular alignment of rigid polythiophene backbones to the substrate by using solvent-vapor treatment. *Advanced Materials*, 19(21):3594, November 2007.

[60] S. Joshi, S. Grigorian, and U. Pietsch. X-ray structural and crystallinity studies of low and high molecular weight poly(3-hexylthiophene). *Physica Status Solidi (a)*, 205(3):488–496, March 2008.

[61] Navaphun Kayunkid, Sureeporn Uttiya, and Martin Brinkmann. Structural Model of Regioregular Poly(3-hexylthiophene) Obtained by Electron Diffraction Analysis. *Macromolecules*, 43(11):4961, June 2010.

[62] K. Tashiro, M. Kobayashi, T. Kawai, and K. Yoshino. Crystal structural change in poly(3-alkyl thiophene)s induced by iodine doping as studied by an organized combination of X-ray diffraction, infrared/Raman spectroscopy and computer simulation techniques. *Polymer*, 38(12):2867, June 1997.

[63] A. Zen, J. Pflaum, S. Hirschmann, W. Zhuang, F. Jaiser, U. Asawapirom, J. P. Rabe, U. Scherf, and D. Neher. Effect of molecular weight and annealing of poly (3-hexylthiophene)s on the performance of organic field-effect transistors. *Advanced Functional Materials*, 14(8):757, August 2004.

[64] D. M. DeLongchamp, B. M. Vogel, Y. Jung, M. C. Gurau, C. A. Richter, O. A. Kirillov, J. Obrzut, D. A. Fischer, S. Sambasivan, L. J. Richter, and E. K. Lin. Variations in semiconducting polymer microstructure and hole mobility with spin-coating speed. *Chemistry of Materials*, 17(23):5610, November 2005.

[65] R. Joseph Kline, Michael D. McGehee, and Michael F. Toney. Highly oriented crystals at the buried interface in polythiophene thin-film transistors. *Nature Materials*, 5(3):222–228, February 2006.

[66] Jean-Marie Verilhac, Gilles LeBlevennec, David Djurado, François Rieutord, Mustapha Chouiki, Jean-Pierre Travers, and Adam Pron. Effect of macromolecular parameters and processing conditions on supramolecular organisation, morphology and electrical transport properties in thin layers of regioregular poly(3-hexylthiophene). *Synthetic Metals*, 156(11-13):815–823, June 2006.

[67] Patrick Pingel, Achmad Zen, Ruben D. Abellon, Ferdinand C. Grozema, Laurens D. A. Siebbeles, and Dieter Neher. Temperature-Resolved Local and Macroscopic Charge Carrier Transport in Thin P3HT Layers. *Advanced Functional Materials*, 20(14):2286, July 2010.

[68] S. Nagamatsu, W. Takashima, K. Kaneto, Y. Yoshida, N. Tanigaki, and K. Yase. Backbone arrangement in "friction-transferred" regioregular poly(3-alkylthiophene)s. *Macromolecules*, 36(14):5252, July 2003.

[69] Jean-Luc Bredas, Joseph E. Norton, Jérôme Cornil, and Veaceslav Coropceanu. Molecular Understanding of Organic Solar Cells: The Challenges. *Accounts of Chemical Research*, 42(11):1691–1699, 2009.

[70] Tracey M. Clarke and James R. Durrant. Charge photogeneration in organic solar cells. *Chemical Reviews*, 110(11):6736–67, November 2010.

[71] D. Beljonne, Z. Shuai, G. Pourtois, and J. L. Bredas. Spin - Orbit Coupling and Intersystem Crossing in Conjugated Polymers: A Configuration Interaction Description. *Journal of Physical Chemistry A*, 105(15):3899–3907, 2001.

[72] Carsten Deibel, Thomas Strobel, and Vladimir Dyakonov. Role of the charge transfer state in organic donor-acceptor solar cells. *Advanced Materials*, 22(37):4097–111, October 2010.

[73] Stoichko D. Dimitrov, Artem A. Bakulin, Christian B. Nielsen, Bob C. Schroeder, Junping Du, Hugo Bronstein, Iain McCulloch, Richard H. Friend, and James R. Durrant. On the energetic dependence of charge separation in low-band-gap polymer/fullerene blends. *Journal of the American Chemical Society*, 134(44):18189–92, November 2012.

[74] Artem A. Bakulin, Akshay Rao, Vlad G. Pavelyev, Paul H. M. van Loosdrecht, Maxim S. Pshenichnikov, Dorota Niedzialek, Jérôme Cornil, David Beljonne, and Richard H. Friend. The Role of Driving Energy and Delocalized States for Charge Separation in Organic Semiconductors. *Science*, 335:1340–1344, 2012.

[75] G. Grancini, M. Maiuri, D. Fazzi, A. Petrozza, H.-J. Egelhaaf, D. Brida, G. Cerullo, and G. Lanzani. Hot exciton dissociation in polymer solar cells. *Nature Materials*, 12(1):29–33, January 2013.

[76] Koen Vandewal, Steve Albrecht, Eric T. Hoke, Kenneth R. Graham, Johannes Widmer, Jessica D. Douglas, Marcel Schubert, William R. Mateker, Jason T. Bloking, George F. Burkhard, Alan Sellinger, Jean M. J. Fréchet, Aram Amassian, Moritz K. Riede, Michael D. McGehee, Dieter Neher, and Alberto Salleo. Efficient charge generation by relaxed charge-transfer states at organic interfaces. *Nature Materials*, 13(1):63–8, January 2014.

[77] A. Pivrikas, N. S. Sariciftci, G. Juška, and R. Österbacka. A review of charge transport and recombination in polymer/fullerene organic solar cells. *Progress in Photovoltaics: Research and Applications*, 15(8):677–696, 2007.

[78] Serap Günes, Helmut Neugebauer, and Niyazi Serdar Sariciftci. Conjugated polymer-based organic solar cells. *Chemical Reviews*, 107(4):1324–38, April 2007.

[79] Gilles Dennler, Markus C. Scharber, and Christoph J. Brabec. Polymer-Fullerene Bulk-Heterojunction Solar Cells. *Advanced Materials*, 21(13):1323–1338, April 2009.

[80] Gang Li, Rui Zhu, and Yang Yang. Polymer solar cells. *Nature Photonics*, 6(3):153, March 2012.

[81] M. C. Scharber, D. Mühlbacher, M. Koppe, P. Denk, C. Waldauf, A. J. Heeger, and C. J. Brabec. Design Rules for Donors in Bulk-Heterojunction Solar Cells - Towards 10 % Energy-Conversion Efficiency. *Advanced Materials*, 18(6):789–794, March 2006.

[82] L. J. A. Koster, V. D. Mihailetchi, and P. W. M. Blom. Bimolecular recombination in polymer/fullerene bulk heterojunction solar cells. *Applied Physics Letters*, 88(5):52104, January 2006.

[83] Ralf Mauer, Ian A. Howard, and Frederic Laquai. Effect of Nongeminate Recombination on Fill Factor in Polythiophene/Methanofullerene Organic Solar Cells. *The Journal of Physical Chemistry Letters*, 1(24):3500–3505, December 2010.

[84] Rico Meerheim, Christian Körner, and Karl Leo. Highly efficient organic multijunction solar cells with a thiophene based donor material. *Applied Physics Letters*, 105(6):063306, August 2014.

[85] Jens A. Hauch, Pavel Schilinsky, Stelios A. Choulis, Richard Childers, Markus Biele, and Christoph J. Brabec. Flexible organic P3HT:PCBM bulk-heterojunction modules with more than 1 year outdoor lifetime. *Solar Energy Materials and Solar Cells*, 92(7):727–731, July 2008.

[86] Matthieu Manceau, Dechan Angmo, Mikkel Jørgensen, and Frederik C. Krebs. ITO-free flexible polymer solar cells: From small model devices to roll-to-roll processed large modules. *Organic Electronics*, 12(4):566–574, April 2011.

[87] Olle Inganäs and W. R. Salaneck. Thermochromic and Solvatochromic Effects in Poly(3-hexylthiophene). *Synthetic Metals*, 22:395–406, 1988.

[88] N. Kiriy, E. Jahne, H. J. Adler, M. Schneider, A. Kiriy, G. Gorodyska, S. Minko, D. Jehnichen, P. Simon, A. A. Fokin, and M. Stamm. One-dimensional aggregation of regioregular polyalkylthiophenes. *Nano Letters*, 3(6):707, June 2003.

[89] Ligui Li, Guanghao Lu, and Xiaoniu Yang. Improving performance of polymer photovoltaic devices using an annealing-free approach via construction of ordered aggregates in solution. *Journal of Materials Chemistry*, 18(17):1984, 2008.

[90] Yeong Don Park, Hwa Sung Lee, Yeon Joo Choi, Donghoon Kwak, Jeong Ho Cho, Sichoon Lee, and Kilwon Cho. Solubility-Induced Ordered Polythiophene Precursors for High-Performance Organic Thin-Film Transistors. *Advanced Functional Materials*, 19(8):1200–1206, April 2009.

[91] Bong-Gi Kim, Myung-Su Kim, and Jinsang Kim. Ultrasonic-Assisted Nanodimensional for Organic Photovoltaic Cells. *ACS Nano*, 4(4):2160–2166, 2010.

[92] A. J. Moulé and K. Meerholz. Controlling Morphology in Polymer-Fullerene Mixtures. *Advanced Materials*, 20(2):240–245, January 2008.

[93] John D. Roehling, Ilke Arslan, and Adam J. Moulé. Controlling microstructure in poly(3-hexylthiophene) nanofibers. *Journal of Materials Chemistry*, 22(6):2498, 2012.

[94] A. G. Andreopoulos and E. M. Kampouris. Mechanical Properties of Crosslinked Polyethyelene. *Journal of Applied Polymer Science*, 31:1061–1068, 1986.

[95] T. K. Kang and C. S. Ha. Effect of processing variables on the crosslinking of HDPE by peroxide. *Polymer Testing*, 19(7):773, 2000.

[96] G. Binnig, C. F. Quate, and C. Gerber. Atomic Force Microscope. *Physical Review Letters*, 56(9):930, 1986.

[97] E. Meyer. Atomic force microscopy. *Progress in Surface Science*, 41(1):3–49, September 1992.

[98] Derek M. Stevens, Yang Qin, Marc A. Hillmyer, and C. Daniel Frisbie. Enhancement of the Morphology and Open Circuit Voltage in Bilayer Polymer/Fullerene Solar Cells. *The Journal of Physical Chemistry C*, 113(26):11408–11415, July 2009.

[99] P. J. Brown, D. S. Thomas, A. Kohler, J. S. Wilson, J. S. Kim, C. M. Ramsdale, H. Sirringhaus, and R. H. Friend. Effect of interchain interactions on the absorption and emission of poly(3-hexylthiophene). *Physical Review B*, 67(6):64203, 2003.

[100] I. O. Shklyarevskiy, P. Jonkheijm, P. C .M. Christianen, A. P. H. J. Schenning, A. Del Guerzo, J. P. Desvergne, E. W. Meijer, and J. C. Maan. Magnetic alignment of self-assembled anthracene organogel fibers. *Langmuir*, 21(6):2108, March 2005.

[101] Igor O. Shklyarevskiy, Pascal Jonkheijm, Natalie Stutzmann, Dorothee Wasserberg, Harry J. Wondergem, Peter C. M. Christianen, Albertus P. H. J. Schenning, Dago M. de Leeuw, Zeljko Tomović, Jishan Wu, Klaus Müllen, and Jan C. Maan. High anisotropy of the field-effect transistor mobility in magnetically aligned discotic liquid-crystalline semiconductors. *Journal of the American Chemical Society*, 127(46):16233–7, November 2005.

[102] P. C. M. Christianen, I. O. Shklyarevskiy, M. I. Boamfa, and J. C. Maan. Alignment of molecular materials in high magnetic fields. *Physica B*, 346:255, April 2004.

[103] Hiroaki Yonemura, Koichi Yuno, Yuuichi Yamamoto, Sunao Yamada, Yoshihisa Fujiwara, and Yoshifumi Tanimoto. Orientation of nanowires consisting of poly(3-hexylthiophene) using strong magnetic field. *Synthetic Metals*, 159(9-10):955–960, May 2009.

[104] D. Richards and F. Cacialli. Near-field microscopy and lithography of light-emitting polymers. *Philosophical Transactions of the Royal Society A-mathematical Physical and Engineering Sciences*, 362(1817):771, April 2004.

[105] Frank C. Spano, Jenny Clark, Carlos Silva, and Richard H. Friend. Determining exciton coherence from the photoluminescence spectral line shape in poly (3-hexylthiophene) thin films. *The Journal of Chemical Physics*, 130:074904, 2009.

[106] H. Yamagata and F. C. Spano. Interplay between intrachain and interchain interactions in semiconducting polymer assemblies: The HJ-aggregate model. *Journal of Chemical Physics*, 136(18):184901, May 2012.

[107] Hajime Yamagata, Chris M. Pochas, and Frank C. Spano. Designing J- and H-aggregates through wave function overlap engineering: Applications to poly(3-hexylthiophene). *The Journal of Physical Chemistry B*, 116(49):14494–503, December 2012.

[108] Frank C. Spano and Carlos Silva. H- and J-Aggregate Behavior in Polymeric Semiconductors. *Annual Review of Physical Chemistry*, 65:477–500, January 2014.

[109] Francis Paquin, Hajime Yamagata, Nicholas J. Hestand, Maciej Sakowicz, Nicolas Bérubé, Michel Côté, Luke X. Reynolds, Saif A. Haque, Natalie Stingelin, Frank C. Spano, and Carlos Silva. Two-dimensional spatial coherence of excitons in semicrystalline polymeric semiconductors: Effect of molecular weight. *Physical Review B*, 88(15):155202, October 2013.

[110] Edwards T. Niles, John D. Roehling, Hajime Yamagata, Adam J. Wise, Frank C. Spano, Adam J. Moule, and John K. Grey. J-Aggregate Behavior in Poly-3-hexylthiophene Nanofibers. *The Journal of Physical Chemistry Letters*, 3:259–263, 2012.

[111] Mina Baghgar, Joelle Labastide, Felicia Bokel, Irene Dujovne, Aidan Mckenna, Austin M. Barnes, Emily Pentzer, Todd Emrick, Ryan Hayward, and Michael D. Barnes. Probing Inter- and Intrachain Exciton Coupling in Isolated Poly(3-hexylthiophene) Nanofibers: Effect of Solvation and Regioregularity. *Journal of Physical Chemistry Letters*, 3:1674, 2012.

[112] Thomas P. Martin, Adam J. Wise, Erik Busby, Jian Gao, John D. Roehling, Michael J. Ford, Delmar S. Larsen, Adam J. Moule, and John K. Grey. Packing Dependent Electronic Coupling in Single Poly(3- hexylthiophene) H- and J Aggregate Nanofibers. *Journal of Physical Chemistry B*, 117:44784487, 2013.

[113] Mitsuo Yamaga, Yuki Masui, Shu Sakuta, Nobuhiro Kodama, and Keiko Kaminaga. Radiative and nonradiative decay processes responsible for long-lasting phosphorescence of Eu2+-doped barium silicates. *Physical Review B*, 71(20):205102, May 2005.

[114] Michael D. Barnes and Mina Baghar. Optical probes of chain packing structure and exciton dynamics in polythiophene films, composites, and nanostructures. *Journal of Polymer Science Part B-Polymer Physics*, 50(15):1121, August 2012.

[115] Mina Baghgar, Joelle A. Labastide, Felicia Bokel, Ryan C. Hayward, and Michael D. Barnes. Effect of Polymer Chain Folding on the Transition from H-

to J-Aggregate Behavior in P3HT Nanofibers. *The Journal of Physical Chemistry C*, 118:2229–2235, 2014.

[116] Jung Ah Lim, Feng Liu, Sunzida Ferdous, Murugappan Muthukumar, and Alejandro L. Briseno. Polymer semiconductor crystals. *Materials Today*, 13(5):14–24, May 2010.

[117] Guangming Wang, James Swensen, Daniel Moses, and Alan J. Heeger. Increased mobility from regioregular poly(3-hexylthiophene) field-effect transistors. *Journal of Applied Physics*, 93(10):6137, 2003.

[118] Youngkyoo Kim, Stelios A. Choulis, Jenny Nelson, Donal D. C. Bradley, Steffan Cook, and James R. Durrant. Device annealing effect in organic solar cells with blends of regioregular poly(3-hexylthiophene) and soluble fullerene. *Applied Physics Letters*, 86(6):063502, 2005.

[119] D. H. Kim, Y. D. Park, Y. Jang, H. Yang, Y. H. Kim, J. I. Han, D. G. Moon, S. Park, T. Chang, C. Chang, M. Joo, C. Y. Ryu, and K. Cho. Enhancement of Field-Effect Mobility Due to Surface-Mediated Molecular Ordering in Regioregular Polythiophene Thin Film Transistors. *Advanced Functional Materials*, 15(1):77–82, January 2005.

[120] Shinuk Cho, Kwanghee Lee, Jonathan Yuen, Guangming Wang, Daniel Moses, Alan J. Heeger, Mathieu Surin, and Roberto Lazzaroni. Thermal annealing-induced enhancement of the field-effect mobility of regioregular poly(3-hexylthiophene) films. *Journal of Applied Physics*, 100(11):114503, 2006.

[121] L. A. Majewski, J. W. Kingsley, C. Balocco, and A. M. Song. Influence of processing conditions on the stability of poly(3-hexylthiophene)-based field-effect transistors. *Applied Physics Letters*, 88(22):222108, 2006.

[122] Yu Fu, Ching Lin, and Feng-Yu Tsai. High field-effect mobility from poly(3-hexylthiophene) thin-film transistors by solventvapor-induced reflow. *Organic Electronics*, 10(5):883–888, August 2009.

[123] Iori Doi, Myeong Jin Kang, and Kazuo Takimiya. High mobility organic thin-film transistors on plastic substrate. *Current Applied Physics*, 12:e2–e5, September 2012.

[124] Yuning Li, Samarendra P. Singh, and Prashant Sonar. A high mobility P-type DPP-thieno[3,2-b]thiophene copolymer for organic thin-film transistors. *Advanced Materials*, 22(43):4862–6, November 2010.

[125] Hagen Klauk, Marcus Halik, Ute Zschieschang, Gunter Schmid, Wolfgang Radlik, and Werner Weber. High-mobility polymer gate dielectric pentacene thin film transistors. *Journal of Applied Physics*, 92(9):5259, 2002.

[126] Tommie Wilson Kelley, Larry D. Boardman, Timothy D. Dunbar, Dawn V. Muyres, Mark J. Pellerite, and Terry P. Smith. High-Performance OTFTs Using Surface-Modified Alumina Dielectrics. *The Journal of Physical Chemistry B*, 107(24):5877–5881, June 2003.

[127] S. C. Lim, S. H. Kim, J. H. Lee, M. K. Kim, D. J. Kim, and T. Zyung. Surface-treatment effects on organic thin-film transistors. *Synthetic Metals*, 148(1):75, January 2005.

[128] S. Grecu, M. Roggenbuck, A. Opitz, and W. Brütting. Differences of interface and bulk transport properties in polymer field-effect devices. *Organic Electronics*, 7(5):276–286, October 2006.

[129] Hagen Klauk. Organic thin-film transistors. *Chemical Society Reviews*, 39(7):2643, 2010.

[130] Gregory M. Newbloom, Felix S. Kim, Samson A. Jenekhe, and Danilo C. Pozzo. Mesoscale Morphology and Charge Transport in Colloidal Networks of Poly(3-hexylthiophene). *Macromolecules*, 44(10):3801, May 2011.

[131] Gregory M. Newbloom, Katie M. Weigandt, and Danilo C. Pozzo. Electrical, Mechanical, and Structural Characterization of Self-Assembly in Poly(3-hexylthiophene) Organogel Networks. *Macromolecules*, 45(8):3452, April 2012.

[132] Minh Trung Dang, Lionel Hirsch, Guillaume Wantz, and James D. Wuest. Controlling the Morphology and Performance of Bulk Heterojunctions in Solar Cells . Lessons Learned from the Benchmark Poly(3-hexylthiophene):[6,6]-PhenylC61-butyric Acid Methyl Ester System. *Chemical Reviews*, 113:37343765, 2013.

[133] Barry C. Thompson and Jean M. J. Fréchet. Polymer-fullerene composite solar cells. *Angewandte Chemie*, 47(1):58–77, January 2008.

[134] Dan Credgington, Rick Hamilton, Pedro Atienzar, Jenny Nelson, and James R. Durrant. Non-Geminate Recombination as the Primary Determinant of Open-Circuit Voltage in Polythiophene:Fullerene Blend Solar Cells: an Analysis of the Influence of Device Processing Conditions. *Advanced Functional Materials*, 21(14):2744, July 2011.

[135] Jung-Yao Chen, Chi-Ching Kuo, Chia-Sheng Lai, Wen-Chang Chen, and Hsin-Lung Chen. Manipulation on the Morphology and Electrical Properties of Aligned Electrospun Nanofibers of Poly(3-hexylthiophene) for Field-Effect Transistor Applications. *Macromolecules*, 44(8):2883, April 2011.

[136] Y. Kim, A. Ballantyne, J. Nelson, and D. Bradley. Effects of thickness and thermal annealing of the PEDOT:PSS layer on the performance of polymer solar cells. *Organic Electronics*, 10(1):205–209, February 2009.

[137] Lichang Zeng, Ching W. Tang, and Shaw H. Chen. Effects of active layer thickness and thermal annealing on polythiophene: Fullerene bulk heterojunction photovoltaic devices. *Applied Physics Letters*, 97(5):053305, 2010.

[138] Pavel Schilinsky, Udom Asawapirom, Ullrich Scherf, Markus Biele, and Christoph J. Brabec. Influence of the Molecular Weight of Poly(3-hexylthiophene) on the Performance of Bulk Heterojunction Solar Cells. *Chemistry of Materials*, 17(8):2175–2180, April 2005.

[139] Lilian Chang, Hans W. A. Lademann, Jörg-Bernd Bonekamp, Klaus Meerholz, and Adam J. Moulé. Effect of Trace Solvent on the Morphology of P3HT:PCBM Bulk Heterojunction Solar Cells. *Advanced Functional Materials*, 21(10):1779–1787, May 2011.

[140] Kyungkon Kim, Jiwen Liu, Manoj A. G. Namboothiry, and David L. Carroll. Roles of donor and acceptor nanodomains in 6% efficient thermally annealed polymer photovoltaics. *Applied Physics Letters*, 90(16):163511, 2007.

[141] Mi Sun Ryu, Hyuk Jin Cha, and Jin Jang. Effects of thermal annealing of polymer:fullerene photovoltaic solar cells for high efficiency. *Current Applied Physics*, 10(2):S206–S209, March 2010.

[142] D. Chirvase, J. Parisi, J. C. Hummelen, and V. Dyakonov. Influence of nanomorphology on the photovoltaic action of polymerfullerene composites. *Nanotechnology*, 15(9):1317–1323, September 2004.

[143] G. Li, V. Shrotriya, J. S. Huang, Y. Yao, T. Moriarty, K. Emery, and Y. Yang. High-efficiency solution processable polymer photovoltaic cells by self-organization of polymer blends. *Nature Materials*, 4(11):864, November 2005.

[144] T. Erb, U. Zhokhavets, G. Gobsch, S. Raleva, B. Stühn, P. Schilinsky, C. Waldauf, and C. J. Brabec. Correlation Between Structural and Optical Properties of Composite Polymer/Fullerene Films for Organic Solar Cells. *Advanced Functional Materials*, 15(7):1193–1196, July 2005.

[145] Jong Soo Kim, Ji Hwang Lee, Jong Hwan Park, Chiyeoung Shim, Myungsun Sim, and Kilwon Cho. High-Efficiency Organic Solar Cells Based on Preformed Poly(3-hexylthiophene) Nanowires. *Advanced Functional Materials*, 21(3):480, February 2011.

[146] Andrew H. Rice, Rajiv Giridharagopal, Sam X. Zheng, Fumio S. Ohuchi, David S. Ginger, and Christine K. Luscombe. Controlling Vertical Morphology within the Active Layer of Organic Photovoltaics Using Poly- (3-hexylthiophene) Nanowires and Phenyl-C61-butyric Acid Methyl Ester. *ACS Nano*, 5(4):3132–3140, 2011.

[147] J. D. Kotlarski and P. W. M. Blom. Ultimate performance of polymer:fullerene bulk heterojunction tandem solar cells. *Applied Physics Letters*, 98(5):053301, 2011.

[148] Tayebeh Ameri, Ning Li, and Christoph J. Brabec. Highly Efficient Organic Tandem Solar Cells: A Follow Up Review. *Energy & Environmental Science*, 6(8):2390, 2013.

[149] Tayebeh Ameri, Parisa Khoram, Jie Min, and Christoph J. Brabec. Organic Ternary Solar Cells: A Review. *Advanced Materials*, 25(31):4245–66, August 2013.

[150] Akira Tada, Yanfang Geng, Qingshuo Wei, Kazuhito Hashimoto, and Keisuke Tajima. Tailoring organic heterojunction interfaces in bilayer polymer photovoltaic devices. *Nature Materials*, 10(6):450, June 2011.

[151] Dian Chen, Feng Liu, Cheng Wang, Atsuhiro Nakahara, and Thomas P. Russell. Bulk Heterojunction Photovoltaic Active Layers via Bilayer Interdiffusion. *Nano Letters*, 11:2071–2078, 2011.

[152] Dian Chen, Atsuhiro Nakahara, Dongguang Wei, Dennis Nordlund, and Thomas P. Russell. P3HT/PCBM Bulk Heterojunction Organic Photovoltaics: Correlating Efficiency and Morphology. *Nano Letters*, 11(2):561, February 2011.

[153] Veronique S. Gevaerts, L. Jan Anton Koster, Martijn M. Wienk, and Rene A. J. Janssen. Discriminating between Bilayer and Bulk Heterojunction Polymer: Fullerene Solar Cells Using the External Quantum Efficiency. *ACS Applied Materials & Interfaces*, 3(9):3252, September 2011.

[154] G. S. Kanner, X. Wei, B. C. Hess, L. R. Chen, and Z. V. Vardeny. Physical review. *Physical Review Letters*, 69(3):538–541, 1992.

[155] Xiao Mei Jiang, Ronald Österbacka, Oleg Korovyanko, Chong P. An, Baruch Horovitz, René A. J. Janssen, and Z. Valy Vardeny. Spectroscopic Studies of Photoexcitations in Regioregular and Regiorandom Polythiophene Films. *Advanced Functional Materials*, 12(9):587–597, 2002.

[156] P. Parkinson, C. Müller, N. Stingelin, M. B. Johnston, and L. M. Herz. Role of Ultrafast Torsional Relaxation in the Emission from Polythiophene Aggregates. *Journal of Physical Chemistry Letters*, 1(19):2788, 2010.

[157] Francis Paquin, Gianluca Latini, Maciej Sakowicz, Paul-Ludovic Karsenti, Linjun Wang, David Beljonne, Natalie Stingelin, and Carlos Silva. Charge Separation in Semicrystalline Polymeric Semiconductors by Photoexcitation: Is the Mechanism Intrinsic or Extrinsic? *Physical Review Letters*, 106(19):197401, May 2011.

[158] Joelle A. Labastide, Mina Baghgar, Irene Dujovne, B. Harihara Venkatraman, David C. Ramsdell, Dhandapani Venkataraman, and Michael D. Barnes. Time- and Polarization-Resolved Photoluminescence of Individual Semicrystalline Polythiophene (P3HT) Nanoparticles. *The Journal of Physical Chemistry Letters*, 2:2089–2093, 2011.

[159] Shuhong Liu, Wechung Maria Wang, Alejandro L. Briseno, Stefan C. B. Mannsfeld, and Zhenan Bao. Controlled Deposition of Crystalline Organic Semiconductors for Field-Effect-Transistor Applications. *Advanced Materials*, 21(12):1217–1232, March 2009.

[160] Rui Zhu, Ankit Kumar, and Yang Yang. Polarizing Organic Photovoltaics. *Advanced Materials*, 23(36):4193, September 2011.

A. Appendix

Temperature-dependent Photoluminescence of Polythiophene Nanofibres

Supporting data to Section 4.2: Deviation of the recorded PL spectra depending on whether the spectrum was measured during cool-down of the cryostat or while warming up using an electrical heating element to stabilise the temperature. Based on the measured spectra, the error introduced by non-stabilised temperature is estimated to be $< 10\,\mathrm{K}$.

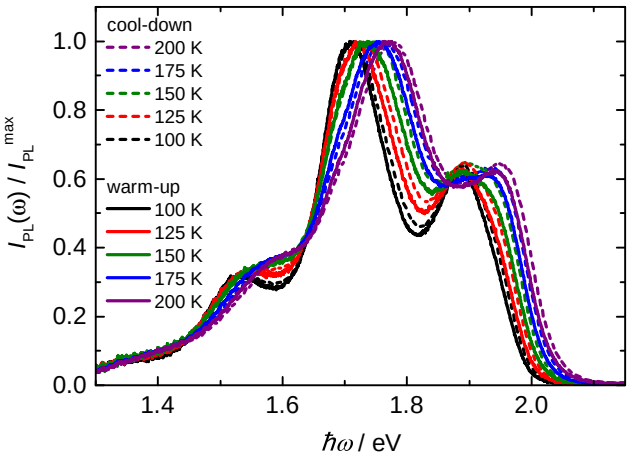

Supporting data to Section 4.3: Temperature-dependent PL spectra of NFs prepared by the method using DTBP, which show an almost identical behaviour to the spectra of the xylene NFs presented in Fig. 4.7(b).